

---


Electronic Theses and Dissertations, 2004-2019

---

2016

## High Temperature Mechanics of Aerospace Ceramic Composites via Synchrotron Radiation

Albert Manero II  
*University of Central Florida*

 Part of the [Mechanical Engineering Commons](#)  
Find similar works at: <https://stars.library.ucf.edu/etd>  
University of Central Florida Libraries <http://library.ucf.edu>

This Doctoral Dissertation (Open Access) is brought to you for free and open access by STARS. It has been accepted for inclusion in Electronic Theses and Dissertations, 2004-2019 by an authorized administrator of STARS. For more information, please contact [STARS@ucf.edu](mailto:STARS@ucf.edu).

---

### STARS Citation

Manero, Albert II, "High Temperature Mechanics of Aerospace Ceramic Composites via Synchrotron Radiation" (2016). *Electronic Theses and Dissertations, 2004-2019*. 5633.  
<https://stars.library.ucf.edu/etd/5633>

HIGH TEMPERATURE MECHANICS OF AEROSPACE  
CERAMIC COMPOSITES CHARACTERIZED VIA  
SYNCHROTRON RADIATION

by

ALBERT C. MANERO II

B.S. University of Central Florida, 2012

M.S. University of Central Florida, 2014

A dissertation submitted in partial fulfillment of the requirements  
for the degree of Doctor of Philosophy  
in the Department of Mechanical and Aerospace Engineering  
in the College of Engineering and Computer Science  
at the University of Central Florida  
Orlando, Florida

Fall Term  
2016

Major Professor:  
Seetha Raghavan

© 2016 by Albert C. Manero II

## ABSTRACT

This research investigates the mechanics of complex aerospace material systems designed for extreme environments. Ceramics and ceramic matrix composites (CMCs) provide highly sought-after capabilities including the potential to withstand extreme temperatures and heat fluxes, severe oxidation and mechanical stresses. Two important material systems form the basis of the scope for this effort: *i*) thermal barrier coatings (TBCs) on Ni-superalloys that have enabled dramatic increases in turbine inlet temperatures exceeding 1100 °C; and *ii*) ceramic matrix composites that have shown capability and promise for hypersonic applications beyond 1300 °C. Understanding the mechanical and material properties of these materials as they evolve with temperature and load requires in-situ measurements under realistic representative environments, and from these measurements life expectancy and failure mechanisms can be more completely elucidated.

In this work, TBCs representative of typical jet engine turbine blade coatings, comprised of a Yttria-stabilized zirconia top coat and NiCoCrAlY bond coat deposited on an IN 100 superalloy substrate were studied. Particular interest was given to the thermally grown oxide (TGO) that develops between the top layer and the bond coat that has a major influence on TBC durability. The oxide scale's development is linked to the typical failure mechanisms observed in application for aircraft engines, and the influence of internal cooling has been shown to vary the behavior and evolution over its lifetime.

Tubular specimens coated via electron beam physical vapor deposition (EB-PVD) were investigated with hard synchrotron X-rays at Argonne National Laboratory's Advanced Photon Source, while subjected to realistic mechanical and thermal loading representative of the engine environment.

A multi-variable investigation was conducted to determine the influence and magnitude of internal flow cooling, external applied force loading, and thermal exposure in cyclical application. The superposition of all these variables together creates variation spatially across in service turbine blades. Lattice strains for the axial and radial directions were resolved for the YSZ top coat layer and the internal thermally grown oxide scale. The findings revealed that during sufficiently high axial loading the strain condition for both the thermally grown oxide and top coat layers may be reversed in direction, and demonstrated how the internal flow and applied mechanical loading produce opposing effects while showing the magnitude of each variable. This reversal of the strain direction is known to contribute to the failure mechanics in the system. This discovery shows that with increased internal cooling to critical zones that experience higher mechanical loads, it is possible to tune the response of the system and prevent the reversal from compressive to tensile strains (in the axial direction). The impact of the results has the potential to be used in design for enhanced durability of the multi-layer coatings.

Ceramic matrix composites are identified to comprise the next generation of turbine blades and high temperature parts. All oxide ceramic matrix composites were investigated for the influence of micro-structure variations and processing on the mechanics of

the system. Isolation techniques of the all alumina composite by means of synchrotron diffraction and tomography presented a novel non-destructive method for evaluating the constituent's properties and evolution. The study successfully revealed how variations in grain size and elastic modulus result in a complex strain states. Further tomographical analysis identified system mechanics influenced by porosity and processing effects. CMCs with an yttria based environmental barrier coating were investigated for comparison to uncoated parts to further capture the in service condition, and revealed considerations for how to improve the durability of the inter-laminar strength of environmental barrier coatings interface.

Together the research conducted has contributed to the high temperature aerospace materials' community, and the experimental work taken strides to provide validation and support future numerical simulation for developing better lifetime modeling. Resulting high temperature mechanics' information has the potential to enhance the design of aerospace components for substantial increases in durability. The outcomes from this work can be leveraged to continue advancing material characterization for aerospace material systems under complex and extreme environments.

*“Every formula which expresses a law of nature is a hymn of praise to God.”*

*- Maria Mitchell*

*“A human being should be able to change a diaper, plan an invasion, butcher a hog,  
conn a ship, design a building, write a sonnet, balance accounts, build a wall, set a  
bone, comfort the dying, take orders, give orders, cooperate, act alone, solve equations,  
analyze a new problem, pitch manure, program a computer, cook a tasty meal, fight  
efficiently, die gallantly. Specialization is for insects.”*

*- Robert A. Heinlein*

## ACKNOWLEDGMENTS

My overwhelming thankfulness to my lovely wife Katie for standing beside me through this journey which has taken us all over the world. To my research advisor and Dissertation Chair, Dr. Seetha Raghavan, for the support and guidance on the project and the investment in my professional development. To my committee members Dr. Jay Kapat, Dr. Jeffrey Kauffman, and Dr. Axel Schülzgen for their guidance and continued support.

To my colleagues at the University of Central Florida who assisted in the project: Dr. Kevin Knipe, Dr. Gregory Freihofer, and Stephen Sofronsky. To Dr. Marion Bartsch for her support of the project and advisement, and the DLR scientists who have supported the collaboration and mentored me through the process: Dr. Stefan Hackemann, Janine Wischek, Katia Artzt, Carla Meid, and Mario Eggeler.

This material is based upon work supported by the Fulbright Academic Grant (Grant No. 34142765), National Science Foundation grants (Grant Nos. OISE 1157619, CMMI 1130837, OISE 1460045, DMR 1337758, and CMMI 1125696) and the German Aerospace Center (DLR). This project was supported by Space Florida and the National Aeronautics and Space Administration through the University of Central Florida's NASA Florida Space Grant Consortium. Special acknowledgments to the College of Engineering and Computer Science and our Dean Georgiopoulos. Use of the Advanced Photon Source, an Office of Science User Facility operated for the U.S. Department of Energy (DOE) Office of Science by Argonne National Laboratory, was supported by the U.S. DOE under Contract No. DE-AC02-06CH11357.



# TABLE OF CONTENTS

LIST OF FIGURES . . . . .	xii
LIST OF TABLES . . . . .	xxii
CHAPTER 1 INTRODUCTION . . . . .	1
1.1 Motivation . . . . .	1
1.1.1 Thermal Barrier Coatings . . . . .	2
1.1.2 Ceramic Matrix Composites . . . . .	5
1.2 Synchrotron Techniques . . . . .	9
1.3 Research Objectives . . . . .	11
1.4 Overview of Research . . . . .	12
CHAPTER 2 EXPERIMENTAL TECHNIQUES . . . . .	14
2.1 Synchrotron Radiation . . . . .	14
2.1.1 X-ray Diffraction Techniques . . . . .	15
2.1.2 Collection Methods . . . . .	15
2.1.3 Fitting Methods and Analysis Procedures . . . . .	17

CHAPTER 3	MATERIALS AND EXPERIMENTAL SETUP . . . . .	19
3.1	Thermal Barrier Coating System . . . . .	19
3.1.1	Sample Design . . . . .	19
3.1.2	Material Properties . . . . .	22
3.1.3	Loading Conditions and Measurement Methods . . . . .	23
3.2	Ceramic Matrix Composites . . . . .	34
3.2.1	Sample Design . . . . .	35
3.2.2	Material Properties . . . . .	42
3.2.3	Loading Conditions and Measurement Methods . . . . .	43
CHAPTER 4	INVESTIGATION OF THERMAL BARRIER COATINGS . . . . .	52
4.1	Objectives . . . . .	52
4.2	Advances in Complex Diffraction Ring Fitting . . . . .	53
4.2.1	Resolving Oxide Scale Diffraction Rings under Interference . . . . .	53
4.2.2	YSZ Texturing . . . . .	56
4.3	Strain Evolution . . . . .	59
4.3.1	TGO Investigation . . . . .	60

4.3.2	YSZ Investigation . . . . .	64
4.4	Investigating Strain State Deviation Between Cycles . . . . .	69
4.4.1	Investigating the YSZ $e_{11}$ vs $e_{22}$ Ratio . . . . .	70
4.4.2	Observing Grain Rotation . . . . .	71
4.4.3	Creep Investigations . . . . .	76
4.5	Discussion of Trends and Design for Durability . . . . .	82
4.6	Conclusions . . . . .	86
CHAPTER 5 MECHANICS OF CERAMIC MATRIX COMPOSITES . . . . .		88
5.1	Objectives . . . . .	88
5.2	Non-destructive Isolation of Fibers and Matrix . . . . .	89
5.2.1	Tomographic Isolation . . . . .	94
5.2.2	Investigating Azimuthal Texturing . . . . .	102
5.2.3	All Alumina Composites . . . . .	105
5.2.4	Alumina Mullite Composites . . . . .	108
5.3	Mechanical Response . . . . .	112
5.3.1	Vertical Fiber Orientation . . . . .	112
5.3.2	Perpendicular Fiber Orientation . . . . .	125

5.4	Composite Mechanics . . . . .	130
5.4.1	Imaging Analysis . . . . .	130
5.4.2	Environmental Barrier Coated Composites . . . . .	134
5.5	Conclusions . . . . .	138
CHAPTER 6 CONCLUSIONS AND OUTLOOK . . . . .		141
6.1	Conclusions . . . . .	141
6.2	Future Developments . . . . .	146
LIST OF REFERENCES . . . . .		148

## LIST OF FIGURES

2.1	Schematic of X-ray diffraction analysis from mechanical loading influence on Debye ring to deviation strain profile in transformed ring. . . . .	18
3.1	Annotated drawing of specimen design [91]. . . . .	20
3.2	As manufactured specimen with an as processed coating [91]. . . . .	21
3.3	Schematic of the thermal gradient and mechanical loading for in-situ X-ray diffraction measurements [91]. . . . .	24
3.4	Specimen scanning methods in line with the X-ray source [116]. . . . .	26
3.5	Specimen inside radiation heater with visible type S uninsulated thermocouple applied in hoop method for measurement and controller feedback [78].	28
3.6	Mutli-variable loading experimental matrix for thermal mechanical testing.	30
3.7	Loading methodology: a) Application of variable loading influences. b) Cycle loading schematics for individual cycles and flow rate study at high temperature [90]. . . . .	32
3.8	Loading conditions to measure viscoelastic response via synchrotron lattice spacing. . . . .	34

3.9	Design of WHIPOX <sup>TM</sup> specimens for thermal and mechanical testing (diffraction) and quantitative imaging (tomography): a) preparation of tomography specimens with ultrasonic drilling and mounted tomography specimen, b) pure $\alpha$ -alumina matrix material, c) unidirectional composite with $\alpha$ -alumina fibers and Mullite matrix, and d) full $\alpha$ -alumina fiber reinforced composite. . . . .	37
3.10	Specimens designed for tomography measurements: a) pure matrix specimen, b) EBC coated Whipox substrate, c) Alumina fiber bundles infiltrated with Mullite matrix, d) perpendicular uni-directional all alumina composite after aging, e) perpendicular uni-directional all alumina composite, and f) vertical uni-directional all alumina composite. . . . .	40
3.11	Specimens designed for diffraction measurements: a) perpendicular fiber alignment of all alumina composite, b) vertical fiber alignment of all alumina composite, c) Alumina fiber with Mullite matrix composite, d) pure matrix specimen, e) all alumina composite with yttria environmental barrier coating deposited. . . . .	41
3.12	Design of thermal and mechanical loading for Whipox: a) schematic of loading and measurement, and b) image of test setup including Whipox shielding for superalloy grips [89]. . . . .	46
3.13	Ultra-high temperature heating chamber with measurement devices interfaced at synchrotron beamline and mechanical loading test frame. . . . .	48

3.14	Experimental methodology: a) variations of neat WHIPOX <sup>TM</sup> specimens loading orientation, b) Thermal and mechanical loading profile for neat WHIPOX <sup>TM</sup> specimens of varying fiber orientations. . . . .	50
4.1	Fitting challenges for transformed Debye rings. Small bond coat precipitate beginning to skew the fitting of the thermally grown alumina oxide. . . . .	54
4.2	Solutions to fitting alumina peaks with obfuscation: (a) Examination of transformed Debye rings with precipitates obscuring oxide layer ring. Secondary peaks marked in blue interfere with faint oxide scale peak marked in green. (b) Fitting challenges for strain response with bond coat overlap over alumina peak. . . . .	56
4.3	Variation in texturing for YSZ: a) multi-constituent diffraction patterns from interior TGO interface, b) textured YSZ diffraction pattern from tangential surface scan with (111) plane not visible, and c) quantification of YSZ (111) texturing pattern from sub-surface scan where plane becomes visible. . . . .	58
4.4	TGO $e_{22}$ strain response over thermal cycle for constant mechanical load with varying flow rate (a, b, c); and re-plotted for constant flow rate with varying mechanical loading (d, e, f). . . . .	61
4.5	(a, b) Extrema testing strain evolution of low, medium, and high mechanical load and internal flow rate. . . . .	62

4.6	Isolating internal flow rate influence: a) Experimental design of flow rate study at 1000°C high temperature hold and increasing internal coolant flow. Variation of (b) TGO $e_{22}$ strains and (c) $e_{11}$ strain. . . . .	63
4.7	YSZ $e_{22}$ strain response over thermal cycle for constant mechanical load with varying flow rate (a, b, c); and re-plotted for constant flow rate with varying mechanical loading (d, e, f). . . . .	65
4.8	YSZ $e_{11}$ (out of plane) strain response over thermal cycle for constant mechanical load with varying flow rate (a, b, c); and re-plotted for constant flow rate with varying mechanical loading (d, e, f). . . . .	67
4.9	YSZ $e_{22}$ (in plane) strain response over internal cooling flow rate increase during high temperature hold. . . . .	68
4.10	(a, b) Extrema testing strain evolution of low, medium, and high mechanical load and internal flow rate. . . . .	69
4.11	$e_{22}/e_{11}$ strain ratio response over thermal ramping cycle for YSZ layer for constant mechanical load (128 MPa) with varying flow rate showcasing the change in residual strains as well as loading ratio. . . . .	71
4.12	YSZ (111) plane azimuthal texturing and variation fitting, highlighting the four independent preferred orientations. . . . .	73



4.13	YSZ (111) plane azimuthal texturing and variation through cycle: a) transformed Debye ring with azimuthal texturing fitted peaks called out, b) through cycle intensity peak deviation for each azimuthal intensity peak.	74
4.14	Creep response and fitting for YSZ (111): a) $e_{22}$ strain response and Power Fit (top) with corresponding strain rate, and b) $e_{11}$ strain response and Power Fit (top) with corresponding strain rate. . . . .	78
4.15	Strain relaxation rate under induced creep loading for YSZ (111): ratio of $e_{22}/e_{11}$ strain response numerical fitting. . . . .	79
4.16	Grain rotation response for YSZ (111) under creep loading: a) transformed Debye ring with azimuthal texturing fitted peaks called out, and b) preferred texturing peaks evolution under creep loading and time. . . . .	80
4.17	Influence of loading conditions: a) Schematic of turbine loading and implementation of internal cooling b) visual schematic to emphasize how the influence of loading variables enables the tuning of the resulting superposition that alters strain evolution. . . . .	85
5.1	Synchrotron X-ray diffraction assessment for all alumina WHIPOX <sup>TM</sup> composites: a) 2D Debye rings for composite, b) peak identification of ring set, and c) representation of crystallographic planes for $\alpha$ -alumina crystals [89]. . . . .	91

5.2	High temperature mechanics under constant loading producing strain response for six crystallographic planes. Lattice plane strains were plotted for $e_{11}$ and $e_{22}$ , and compared directly to their calculated (hkl) dependent elastic modulus. . . . .	93
5.3	Isolated fiber and matrix segmentation showcasing zones of interest. Image produced in Avizo Fire <sup>TM</sup> . . . . .	95
5.4	Vertical slice of all oxide composite showing processing defects. Image produced in ImageJ <sup>TM</sup> . . . . .	96
5.5	Isolation of fiber matrix interface: a) alumina matrix isolated from fiber and b) isolated alumina fibers with visible axial roughness. Image produced in ParaView <sup>TM</sup> . . . . .	97
5.6	Isolation of sub-volume with fiber (red), matrix (green), and porosity voids (blue) for all alumina composite. Image produced in ParaView <sup>TM</sup> . . . . .	99
5.7	Radiography assessment: Tracking fiber motion and specimen rotation via radiography for conditions of 1200 °C and 40 MPa compressive loading at the <i>a</i> : mid-hold at $t_i = 11$ minutes and <i>b</i> : at the conclusion of the hold $t_f = 16$ minutes [89]. . . . .	101
5.8	Azimuthal texturing investigation: a) Peak intensity plots for alumina (110) and (113) planes around the azimuth resulting from Nextel <sup>TM</sup> 610 (alumina) fibers in a Mullite slurry matrix, and b) azimuthal texturing for (110) and (113) pure alumina matrix specimens. . . . .	103

5.9	Azimuthal texturing investigation: a) comparison of diffraction ring intensity and peak broadening for pure matrix and aged pure matrix specimens, b) azimuthal texturing for (024) lattice plane for the pure alumina matrix specimen, and c) azimuthal texturing for lattice plane (024) for the heat treated aged pure alumina matrix specimens. . . . .	106
5.10	Tomographic inspection and comparison of cross sectional slices for a) pure alumina matrix specimens and b) heat treated aged pure alumina matrix specimens. Image processed in ParaView <sup>TM</sup> . . . . .	107
5.11	Diffraction ring lineout plots with peak and constituent identification for composites with alumina fibers with Mullite matrix. . . . .	109
5.12	Transformed Debye rings for composite specimen with alumina fibers with Mullite matrix. . . . .	110
5.13	Zone of interest highlighted on the transformed Debye rings for (120) Mullite diffraction plane for composite specimen with alumina fibers with Mullite matrix. . . . .	111
5.14	Diffraction azimuthally averaged lineout plot for all alumina composite with vertical fiber orientation with variations in applied nominal loading at ambient temperature: a) overview of main diffraction planes and b) highlighted subsection for the (113) alumina plane at approximately 2.07 Å.	114

5.15	Investigation of aged all alumina composite with vertical fiber orientation: a) depth scans starting from tangential edge to sample center nominal applied loading, b) transformed Debye imaging for edge scan for nominal loading and c) transformed Debye imaging for center scan for nominal loading; d) depth scans starting from tangential edge to sample center for mid-level loading (667 N), e) transformed Debye imaging for edge scan for mid-level loading (667 N), and transformed Debye imaging for center scan for mid-level loading (667 N). . . . .	117
5.16	Comparison of Debye transform imaging for variations in applied loading on uni-axial (unaged) aligned alumina fibers in an alumina matrix from a) nominal, b) 958 N, to 1304 N while held at ambient temperature presenting the evolution of composite strain manifested in ring splitting. . . . .	119
5.17	Identification of alumina (024) satellite peak formation and division with increased applied loading from nominal at ambient temperature: a) diffrac- tion lineout peaks and b) transformed Debye ring imaging. Fiber (c) and matrix (a, b) peak subdivision is identified, along with zirconia contami- nation (i). . . . .	120
5.18	Comparison of transformed Debye ring imaging for applied nominal load- ing (87 N) and (1304 N) featuring peak shifting and division. . . . .	122

5.19	Comparison of alumina (113) plane full width half maximum (a, b, c) and diffraction strain (d, e, f) with variations in applied mechanical loading for quasi uni-directional perpendicular to loading to loading alumina fibers with Mullite matrix as processed in ambient. . . . .	126
5.20	Comparison of alumina (110) plane full width half maximum (a, b, c) and diffraction strain (d, e, f) with variations in applied mechanical loading for quasi uni-directional perpendicular to loading to loading alumina fibers with Mullite matrix as processed in ambient. . . . .	128
5.21	Comparison of alumina (110) and (113) planes diffraction strains with variations in applied mechanical loading for quasi uni-directional perpendicular to loading to loading alumina fibers with Mullite matrix as processed in ambient. . . . .	129
5.22	Tomographic imaging visual analysis for comparing a) alumina fiber bundle with alumina matrix and b) alumina fiber bundle with Mullite matrix. Image development conducted in Paraview <sup>TM</sup> . . . . .	131
5.23	Tomographic imaging visual analysis for identifying a) alumina fiber debonding from alumina matrix, b) isolated alumina fibers from Mullite matrix, and c) visualization of alumina fibers and Mullite matrix processing defects. Images constructed by our collaboration in Avizo <sup>TM</sup> [11]. . . . .	133

5.24	Tomographic cross sectional analysis for WHIPOX <sup>TM</sup> substrates with $\pm 45^\circ$ orientation to investigate the non-uniform coating interface. Image development conducted in Paraview <sup>TM</sup> . . . . .	135
5.25	Tomographic analysis for WHIPOX <sup>TM</sup> substrates with $\pm 45^\circ$ orientation to investigate porosity variations between the EBC, CMC substrate, and the coating interface. Image development conducted in Paraview <sup>TM</sup> . . . .	136
5.26	Defined interface porosity on a 3D visualization with uniform fine pore size, captured on WHIPOX <sup>TM</sup> substrates with $\pm 45^\circ$ orientation with EBC coating. Image development conducted in Paraview <sup>TM</sup> . . . . .	138
5.27	Modeling and simulation: realistic geometries and properties extracted from synchrotron studies now in use by DLR scientists [11]. . . . .	140

## LIST OF TABLES

3.1	High Temperature and Room Temperature Material Properties for Thermal Barrier Coating System on IN100 Substrate [62]. . . . .	22
3.2	Specimen naming nomenclature for WHIPOX <sup>TM</sup> samples. . . . .	38
3.3	Specimen listing for tomography and diffraction experiments. . . . .	39
3.4	Material properties variation for all alumina composite, alumina matrix with Mullite fibers, and Mullite matrix and alumina fibers [111]. . . . .	42
3.5	Material properties of pure Nextel 610 alumina fibers [132]. . . . .	43

# CHAPTER 1 INTRODUCTION

## 1.1 Motivation

Aerospace materials demand high performance in the most extreme environments. Designing for strength and flexibility, while minimizing density and subsequently weight, is of high priority to the field [5]. The importance of weight reduction translates to large savings for aircraft and power generation. High temperature alloys have been employed to extend performance and manufacturing methods have been constantly improving to increase their effectiveness. Aircraft engines and power generation turbines utilize large blades in the high temperature gas flow to generate thrust and power. Increasing the combustion temperatures has continued to raise the efficiencies of the engines [16]. With this increase in temperatures, the superalloy high temperature properties have been pushed to the limit [113]. Further, as emission standards continue to be elevated emphasis has been placed to increase the inlet temperatures in lieu of further combustion chamber increases to avoid additional NO<sub>x</sub> emissions and increase efficiency [34, 94, 86]. Here a single percent increase in the system efficiency can save \$200,000 in fuel cost per year for a gas powered turbine [101]. These challenges have necessitated the development of overlay coatings to protect the expensive superalloy blades from both extreme temperatures and environmental damage. Next generation materials have been in development, including ceramic matrix composites, that promise to extend performance and reduce weight and potentially transform the industry.



### 1.1.1 Thermal Barrier Coatings

In an effort to maintain and increase the longevity of the superalloy blades, internal cooling flows have introduced thermal gradients, and architected thermal barrier coatings (TBC) have been applied to reduce the influence of the extremely hot gas environment [39]. Traditionally, TBCs for aircraft engine blades comprise a superalloy load bearing substrate with an yttria-stabilized zirconia (YSZ) coating deposited via electron-beam physical vapor deposition (EB-PVD). This micro-structure differs from that of what is used for power generation turbines, where atmospheric plasma spray is preferred to deposit much larger coating thicknesses. EB-PVD deposition is used for generating layers with a columnar structure, resulting in the necessary strain tolerance during thermal and mechanical cyclic loading in service. The adherence of the ceramic top coat is commonly ensured by the use of a metallic bond coat, such as NiCoCrAlY. As the YSZ topcoat micro-structure is permeable to oxygen, an oxide scale forms between the bond coat and zirconia topcoat and prevents more dramatic oxidation of the superalloys substrate [46]. For this microstructure, mud cracks have been observed to form at the columnar gap space of the YSZ [88] and has been a point of simulation and continued study [65] for how high temperature exposure and sintering influence the layer mechanics.

The formation of the protective scale initiates during the deposition process with less than 1 micron thickness, but during its lifetime it grows in response to high temperature exposure. The growth rate is non-linear in nature and can influence the resulting mechan-

ical behavior of the coating system in response to complex loading conditions. It has been observed that the oxide scale has a critical role in the failure mechanisms of the coating system, and this has been of great interest for study in literature [26, 46, 44, 48, 57, 70] to understand and predict the lifetime of the coating system. Synchrotron investigations have shown how phase changes occur during initial growth [127], while studies regarding creep have shown how the mechanics of the oxide scale can change with cycling [126].

Much research has been conducted on flat coupon specimens to evaluate the effect of thermal loading [36, 48, 103]. While such tests have been very effective for ranking different coating systems with respect to performance, they have also pointed to the need to conduct lifetime assessment under complex service conditions.

Thermo-mechanical fatigue (TMF) tests have advanced the understanding of the system failure mechanics of both atmospheric plasma spray and electron beam physical vapor deposition methods by experimental [124, 17, 135, 104] and numerical simulation [124, 118], and have revealed multiple damage mechanisms are active depending on the levels of applied mechanical loading on the system [124]. Remé et al [104] conducted TMF loading on tubular cylindrical specimens and identified that short duration TMF testing decreased lifetime to spallation. Further it has been seen that cyclic conditions can produce increased compressive strain in the coating at the minimum cycle temperature, whereby reducing the longevity compared to non-cyclic testing [135].

The inclusion of induced thermal gradients, such as air cooling on the leeward surface of a coupon contrasted with torch heating [74, 41, 85] and offsetting radiation and grip

cooling to produce multi-directional gradients [95], has advanced the characterization and deciphering of TBC behavior under thermal mechanical loading. This has revealed that the effects of the thermal gradient result in significant effects on the stress profile and such the constituent's failure mechanisms. Further work with tubular specimens has enabled the investigation of realistic curvature and internal cooling flow paths [12, 13] on damage and failure behavior of TBC systems. These tests have shown the extent that the system's response due to thermal gradients across the thickness conditions may result in a change in crack orientation. To understand holistically the influence of the applied loading and how it relates to the high temperature mechanics, real time in-situ measurements are seen to be a necessity.

Building upon the prior art of our collaborators [12, 13] for application of complex loading, novel in-situ thermal mechanical X-ray diffraction strain measurement have been developed [116, 78, 90] to reveal the role of loading variations on the different layers of a TBC coating system under representative service loading. In the prior art the strain evaluations for the TGO, which are governing the TBC failure in most cases, have been limited [78] due to the difficulty of assessing the minimal intensities coming from the thin layer's diffracted volume.

To advance the understanding of both the role and effect of the loading conditions, and to isolate their influence, in-situ measurements are required. Transient and time dependent behaviors for multi-layer composites can be observed with the application of high energy X-ray diffraction from a synchrotron source in in-situ testing [116, 78, 90].

The high available energies and flux result in short collection times and high spatial resolution for the simultaneous non-destructive analysis of multiple constituents and layers. This has been leveraged in this work to elucidate the conditions' influence on the failure mechanisms that plague TBCs. Considering thermal barrier coatings with mild isothermal aging, in-situ diffraction measurements of both the thermally grown oxide scale and YSZ top coat have been evaluated for their mechanics across representative service conditions.

### **1.1.2 Ceramic Matrix Composites**

Ceramic matrix composites have shown exceptional promise for application in extremely high temperature environments, including combustion liners and thermal protection systems [100]. With higher temperature stability than metallic superalloys and even thermal barrier coatings, ceramic matrix composites could potentially solve a number of challenges that plague thermal barrier coatings. With increased stiffness and extremely high strengths even at high temperatures coupled with chemical stability, the potential has attracted great research aims and industry development. However, with great strength also came brittleness and challenges for manufacturing. Similar to traditional ceramics, thermal shock remains a large issue; similarly load partitioning and manufacturing defects also pose challenges for application [30]. Further investigations revealed that creep effects could undermine the composites' effectiveness as well [56, 25, 100, 122].

Though the challenges remain great, the promises of dramatic weight reduction and higher application temperatures of 1500°C have proven worth the continued investment. Unlike traditional ceramics, ceramic matrix composites reduce the fears of catastrophic brittle failure [10]. However while oxidation resistance at high temperature is improved from some traditional materials due to protective oxide scales, the performance still leaves some desired improvements. Further, re-crystallization at high temperatures can decrease performance unless mitigated by doping materials or additional constituents in the composites [98, 63].

Ceramic fiber based composites are designed for high temperature applications, where oxidation is of concern. They can be classified in two categories: *i*) weak interface composites (WIC) and *ii*) weak matrix composites (WMC) [80]. When designing for durability and damage tolerance, a balance between the matrix fiber debonding against matrix cracking is desired, and composites can be classified from WIC to WMC. Substantial efforts to understand the mechanics of such composites, and to simulate and predict loading response, have been conducted and revealed challenges as the properties change during and over the course of thermal aging [28, 81, 80, 29, 123]. Comparing a composite ratio of elastic modulus ratios of the axial and 45° with the matrix density, a trend reveals that samples with higher porosity matrix have ratios well over 1 whereas samples with denser matrix properties have elastic modulus ratios closer to unity [80].

One material of interest that has gained traction is that of silicon carbide composites [82, 100, 71, 9, 137]. While silicone carbide based parts are of high interest for turbine

blades, shortcomings have suggested an alternative composite for combustion liners and parts after the turbine. This alternative is a unique class of ceramic matrix composites of all oxide composites. These materials hold excellent high temperature strength and stability [108, 84]. One particular composite called Wound Highly Porous Oxide (WHIPOX<sup>TM</sup>) has been developed and investigated for application in extreme environments [69, 50, 111]. All alumina ceramic fibers are drawn and shaped using a computer controlled winding facility, where a slurry of all alumina or Mullite is used to impregnate the fibers. The final product is cut from the winding mandrel and pre-processed in a drying furnace [51, 109]. WHIPOX<sup>TM</sup> can further be characterized as a low level WIC composite, with axial vs 45° elastic modulus ratio near 2 [80].

WHIPOX<sup>TM</sup> provides exciting mechanics for application including quasi-ductile behavior [111, 110, 106] which promises to unlock the potential of improved high temperature mechanics without the fear of catastrophic brittle failure. There are limitations to this, where above 1300°C the material begins to transition back to the brittle bulk material as sintering takes place [52]. Its high porosity percentage, upwards of 40%, enables resistance to damage propagation [139]. Due to its additional properties of being radio transmission transparent, WHIPOX<sup>TM</sup> has found application on rocket parts for high temperature protection panels for radio transmitters [121, 45].

High temperature testing has elucidated some of the mechanics for WHIPOX<sup>TM</sup> composites including creep mechanisms [6, 56, 115]. Numerical simulation has continued to predict mechanical response however bulk material processing defects have proven chal-

lenging to model [106, 109]. Mechanical testing has revealed that porosity variation has significant influences on elastic modulus and strength [15].

Fully understanding the material's mechanics is still of research interest. One study has explored the nature of high temperature deformation mechanics, examining the role of matrix compaction against fiber realignment and anisotropic creep behavior [89, 6]. Simulation has examined the creep response from pure isochoric matrix, which leads to larger fiber rotation, versus compressible matrix properties. These findings demonstrated the variation in fiber realignment could be significant depending on the true material properties.

In order to more completely simulate the behavior of the composite, it is necessary to define the mechanics of the fiber and matrix independently. However this is challenging to decipher as the all alumina constituents mechanics vary from the pure matrix or independent fibers. In this study, effort has been made to utilize high energy synchrotron X-rays to elucidate the independent matrix and fiber mechanical properties. Investigations for the influence of micro-structure and the role of processing on the mechanics of the system are to be develop, as understanding the each constituent's local properties and composite properties. Isolation of the all alumina composite by means of synchrotron diffraction and tomography will enable a more complete understanding of the system mechanics including how damage propagates and is resisted.

## 1.2 Synchrotron Techniques

The X-ray consists of photons of electromagnetic radiation with a wavelength spanning 0.01-100 Angstroms, in the range between ultra-violet and gamma ray radiation [60]. Because of the small wavelengths, X-Rays are uniquely capable of probing the crystalline structure where inter-atomic spacing is on the order of 1 Angstrom. Peter Debye's work with Paul Scherrer and Albert Hull helped to develop the first X-ray optics and cameras, enabling the scientific community to harness the X-ray for non-destructive analysis [21, 22, 23]. Using the diffraction of the light through the crystal, an understanding of the crystalline properties was made possible.

Synchrotron sources use long linear accelerators (LINAC) and booster rings to accelerate a stream of electrons to 99.9999% of the speed of light. Bending the electron path with powerful magnetic fields, the photons are emitted from the electrons when an insertion undulator device or bending magnet is applied [40, 55, 60]. The resulting X-Rays can then be tuned and filtered to provide a stream of monochromatic light of uniform wavelength with extreme precision [133]. The Sector 1 beamline at the Advanced Photon Source of Argonne National Laboratory utilizes an undulator insertion device to produce extremely bright X-rays between 50 keV and 150 keV with flux at  $7 \cdot 10^{10}$  photons per second at 80 keV [54]. When applied with a 1D or 2D detector, the very bright X-Rays can be used in reflection or transmission mode and penetrate larger depths of diffraction volume, even for dense elemental materials [18, 35, 40, 60].



The advent of two dimensional detectors has allowed for much faster measurement times. When coupled with a high energy synchrotron source, the capabilities for non-destructive testing were greatly improved. 2D area detectors collect slices of the resulting diffraction cone, and are viewed in the form of Debye rings, whose radius is inversely proportional with lattice spacing [60, 59].

The orientation and quantity of crystal grains produce starkly different results, where powder material with amorphously aligned crystals produce the most resolute complete ring sets. Single crystals produce spots according to their crystal structure, leaving a mostly incomplete ring. Materials can be classified based on their grain orientations via examining texturing in the ring set. Some materials exhibit a spotty or roped like texturing, characterized by continuous where the degree of amorphousness is high for the polycrystalline set, but the ring has high intensity spots instead of a fully continuous ring [60, 64, 77, 24].

One product of X-ray diffraction was the ability to measure real time micro strains by comparing the inter-atomic spacing of the crystals. In a powder state, randomly aligned unstressed crystals will diffract in perfectly circular rings. When introducing thermal driven strain or mechanical strain, the ring set is subsequently stretched or distorted. Measuring the deviation at the principle axis can provide information on the primary strains, while the degree of distortion reflects the shear in the system. Fitting the entire ring to an ellipse provides a fundamental equation of strain from which the primary strain components can be distilled [38, 60, 58, 128].

Throughout this study synchrotron diffraction will be utilized to determine in-situ strain evolution, phase changes, and ultimately the material mechanics. Further computed tomography (3D) and radiography (2D) to investigate micro-structure, processing defects, and observe failure mechanisms [8, 129, 73]. Coupled with realistic loading, this process will enable the identification of deformation mechanics representative of in service behavior.

### 1.3 Research Objectives

The scope of this study has been divided into two sections, but both are united by the common goal of elucidating high temperature mechanics. Experiments were designed to investigate multi-layer aerospace material systems including *i*) thermally barrier coatings on superalloy substrates and *ii*) all oxide ceramic matrix composites. The research scope is presented here, outlining the major goals of the study.

1. Investigation of thermal barrier coating system strain response using in-situ measurements
  - Multi-variable analysis of loading conditions
  - Identify high temperature mechanics for oxide scale and zirconia topcoat
  - Advancing design parameters for increasing durability and lifetime
2. Understanding ceramic matrix composites' mechanics and micro-structure

- Isolate matrix and fiber via synchrotron imaging
- Identify influence of mechanical loading and partitioning

## 1.4 Overview of Research

The manuscript is segmented into the following sections. *Chapter 1* provides an overview of the motivation and state of the art for high temperature aerospace materials as well as synchrotron techniques, as well as the research scope for both segments of the investigation. *Chapter 2* outlines the unique experimental techniques specific for synchrotron x-ray studies. Specific attention is paid to detailing the collection methods and analysis strategies. In *Chapter 3* the details of the specimen design and experimental setup are detailed.

*Chapter 4* discusses the primary objective for the study on thermal barrier coatings, and the results of the multi-variable assessment of loading conditions are presented for the ceramic top coat and thermally grown oxide scale. Secondary findings including high temperature mechanics, creep investigations, and considerations for plasticity are detailed.

In *Chapter 5* the investigation on ceramic matrix composites is presented and results featuring comparison of anisotropy, texturing and plastic strain consideration, and fiber matrix shear strain investigations are reported.

*Chapter 6* presents how the significance and impact of the research outcomes from this work. The current research outcomes have developed a path for future research efforts to achieve outcomes. This proceeds the extensive list of references from the state of the art.

## **CHAPTER 2 EXPERIMENTAL TECHNIQUES**

The use of X-ray spectroscopy and crystallography have been powerfully influential to advance the field of material science, aerospace structures, and even in-situ behavior. The tool has advanced the study of DNA and genetics, high temperature material properties, and non-destructive testing. With the advent of synchrotron sources, the ability to investigate dense and increased volume fractions allowed for novel experiments and the ability to improve simulation with real time material and crystallographic information. This has led to advances in power generation, aircraft engine efficiency, and the field of biomedical engineering.

### **2.1 Synchrotron Radiation**

The development of two dimensional detectors and synchrotron sources has allowed for short measurement times and sufficient throughput to collect diffraction signals through a wide range of materials, from ceramics to superalloys. These advanced detectors collect slices of the resulting diffraction cone, and are viewed in the form of Debye rings, whose radius is inversely proportional with lattice spacing. For this study the synchrotron at the Advanced Photon Source at Argonne National Laboratory was utilized with a X-ray energy of above 65 keV.

### 2.1.1 X-ray Diffraction Techniques

The five major components in a 2 dimensional X-ray diffraction (XRD) system include an area detector, an X-ray generator, X-ray optics (monochromator and collimator), goniometer and sample stage, and sample alignment and monitoring (laser/video) system [60]. Through diffraction, researchers have the ability to measure real time micro strains by comparing the inter-atomic spacing of the crystals. In a powder state, randomly aligned unstressed crystals will diffract in perfectly circular rings. When introducing thermal driven strain or mechanical strain, the ring set is subsequently stretched or distorted. Measuring the deviation at the principle axis can provide information on the primary strains, while the degree of distortion reflects the shear in the system. The governing principle behind the phenomena of the scattering of photons is Bragg's Law, and is presented in Equation 2.1. Photons are deflected by charged electron clouds, and select photons pass through a keyhole in the crystallographic lattice plane spacing [33].

$$2 * d * \sin(\theta) = n/\lambda \quad (2.1)$$

### 2.1.2 Collection Methods

X-ray diffraction patterns were obtained using the high-energy X-ray diffraction technique offered at the 1-ID Beamline at the Advanced Photon Source (APS) at Argonne

National Laboratory (ANL). This high-energy XRD technique employed monochromatic transmission geometry fitted with a GE 41RT with 2048 x 2048 pixels area detector to measure volume fraction of phases present and crystallographic texture qualities in each phase of the polycrystalline material. The detector rotation relative to the Debye cones was  $25.852^\circ$ ; and had a resolution of  $104 \Delta E/E$ . The beamline was slitted to  $30 \times 300 \mu\text{m}$  and was operated at 65 keV with CuK ( $0.7125 \text{ \AA}$ ) radiation. High flux was optimized for the throughput power to penetrate the materials in study. In order to obtain precise and accurate information from the scans, calibration of the detector position and orientation with respect to the incident beam was performed using ceria powder. A sample to detector distance yielded crystallographic range of d-spacings of 1.3 to  $3.5 \text{ \AA}$ .

Radiographic and tomographic imaging was conducted with a Retiga 4000DC charge-coupled device with 2048 x 2048 pixels. A step size of  $0.2^\circ$  was used to capture  $360^\circ$ , resulting in 1800 images captured for reconstruction of the 3D volume with a voxel size of 1.3 microns.

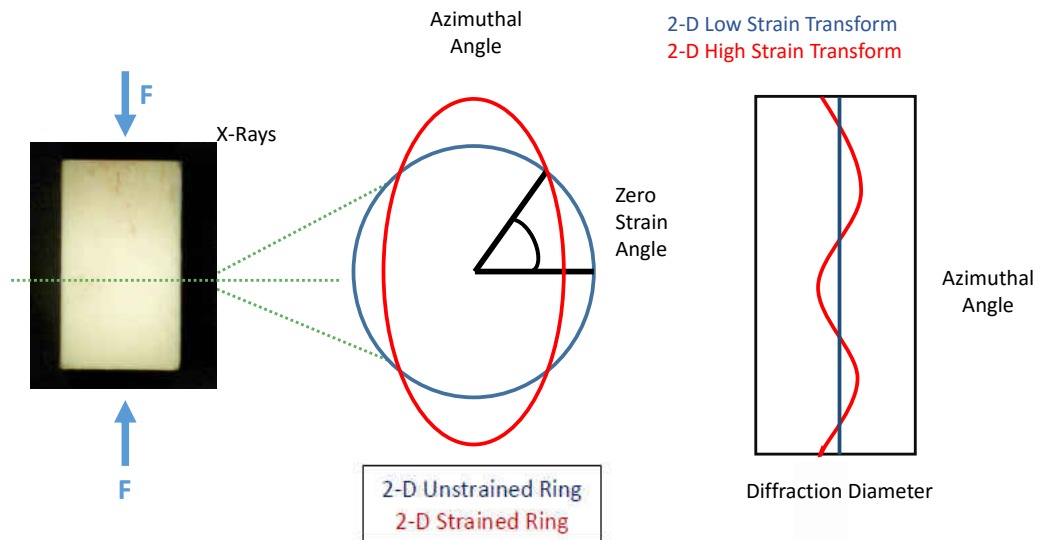
Instrumentation sensitivity towards analysis error has been determined experimentally by Jakobsen [66] on the equipment at the Advanced Photon Source 1-ID beamline. The 2D area detector pixel size is  $80.5 \times 80.5$  microns, with a point spread of  $100 \times 100$  microns [66]. Azimuthal binning utilized in the studies herein was resolved at a minimum of  $2^\circ$ , with strain analysis being conducted over  $15^\circ$  intervals on average.

### 2.1.3 Fitting Methods and Analysis Procedures

As the diffracted photons are collected by the 2D detector, the resulting Debye ring pattern is converted into a pixel map array. High-performance computing (HPC) batch correction was used to convert area detector data and MATLAB<sup>TM</sup> was used for subsequent processing. Each lattice plane has a specific inter-atomic spacing that varies with temperature and mechanical loading. In a randomly oriented poly-crystal, a sufficiently high number of grains are assumed to be present. Due to their near random orientation, complete circular Debye rings are produced. Single crystals produce spots depending on the crystal structure, leaving a mostly incomplete ring. Materials studied in this project have varying grain particle statistics, texturing or preferred orientation of grains, and grain size [134, 60]. These factors produce different types of diffraction response and can shed light on the material being scanned.

The pixel map of the Debye rings can be transformed azimuthally and discretized into bins to conduct further analysis. The binning parameter can be set to account for the appropriate amount of the ring to be averaged, and the resulting pixels are measured for the radius from the center of the diffraction cone. This process allows for radius deviation azimuthally to be quantified, and after examining the entirety of the ring a strain profile can be fit to the data. Variations in texturing around the azimuth can be collected and quantified, allowing for the identification of recrystallization and changes in preferred orientation. A schematic of the process is presented in Figure 2.1.





Note: not to scale

Figure 2.1: Schematic of X-ray diffraction analysis from mechanical loading influence on Debye ring to deviation strain profile in transformed ring.

Analysis is conducted in tailored in-house generated MATLAB<sup>TM</sup> codes based upon the original codes from 1-ID beamline scientists at the Advanced Photon Source. In this work, the analysis method has been refined and is of discussion in *Chapter 4* to account for high interference of select data of interest.

## **CHAPTER 3 MATERIALS AND EXPERIMENTAL SETUP**

Herein this chapter, the design and methodology for both segments of the study are to be detailed. The investigations on thermal barrier coating systems and ceramic matrix composite systems are presented independently, although they share equipment and measurement strategies. Discussion of the specimen materials, geometry, and experimental setup are elaborated upon. Synchrotron measurement techniques are discussed, along with the role of sample design to utilize X-ray diffraction and tomography for elucidating material mechanics non-destructively.

### **3.1 Thermal Barrier Coating System**

The study of aerospace ceramic composites focused on the multi-layer thermal barrier coatings deposited via electron beam physical vapor deposition, with emphasis on non-destructively characterizing the multiple layers in tandem.

#### **3.1.1 Sample Design**

This experiment used tubular dog bone shaped specimens specified in [116, 14]. The substrate was an Inconel 100 directionally solidified alloy, with an inner diameter of 4

mm and outer diameter of 8 mm. The coated length was 102 mm of the full length of 160 mm. The design with annotations is presented in Figure 3.1.

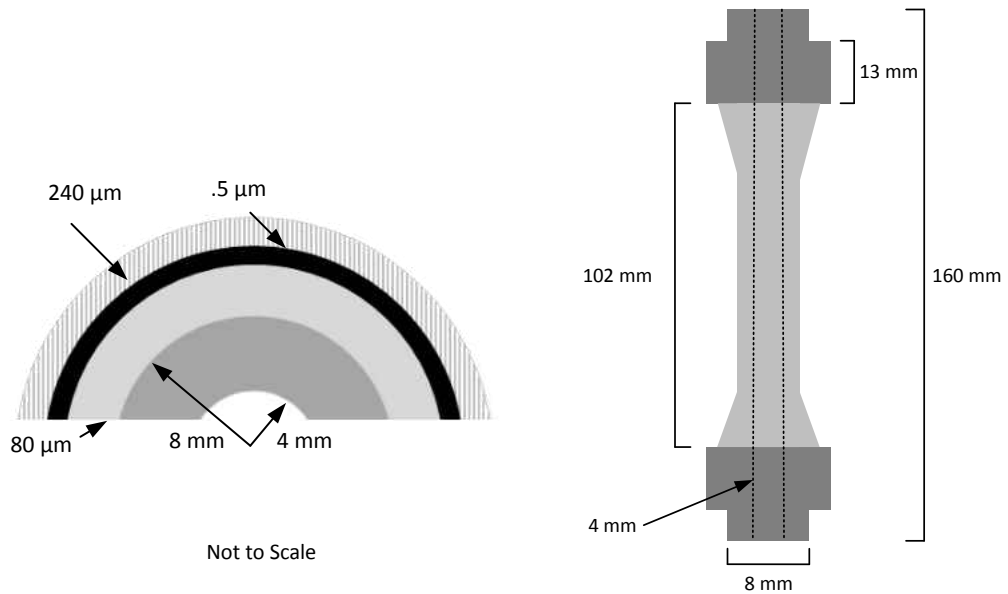


Figure 3.1: Annotated drawing of specimen design [91].

The bond coat of NiCoCrAlY was deposited via EB-PVD to a thickness of  $118 \pm 4$  microns, on which adhered a partially stabilized zirconia top coat with 7-8% yttria content at a thickness of  $211 \pm 4$  microns. The as-coated specimen is presented in Figure 3.2.



Figure 3.2: As manufactured specimen with an as processed coating [91].

The specimen was additionally threaded for testing under tensile mechanical loading. For a more complete look at the micro-structure, scanning electron microscopy is effective. Collaborative partners have done extensive examination of microscopy for thermal barrier coating systems [61, 62]. The specimen was aged in a uniform, isothermal, high temperature furnace for 304 hours at 1000 °C in air to develop the thermally grown oxide to approximately 5 microns and simulates representative thermal aging of the specimen. Prior work has examined the as-coated and lightly cycled specimens [90, 78] and is effective for comparison. However, in the prior work the thermally grown oxide presented an insufficient diffraction volume to be examined in the as processed condition. The work

presented in this study featuring the aged specimen allowed for the investigation of the oxide scale as well as the aged, more complex, ceramic top coat.

### 3.1.2 Material Properties

The mechanical and material properties known for the Thermal Barrier Coating system employed in this study are presented in Table 3.1, and have been used by researchers for simulating loading effects in literature [62].

Table 3.1: High Temperature and Room Temperature Material Properties for Thermal Barrier Coating System on IN100 Substrate [62].

	Substrate		Bond Coat		TGO		Top Coat	
	RT	HT	RT	HT	RT	HT	RT	HT
Elastic modulus, radial[GPa]	215.00	148.00	140.00	70.00	360.00	340.00	13.00	16.00
Elastic modulus, axial [GPa]	120.00	80.00	-	-	-	-	-	-
Poisson ratio, $\nu$	0.30	0.30	0.32	0.35	0.24	0.24	0.22	0.28
CTE, $\alpha[10^{-6}1/K]$	11.50	18.80	8.60	16.60	6.00	8.70	9.00	11.50
Thermal Cond., $\lambda[W/mK]$	15.00	30.00	8.70	27.50	23.00	5.00	1.88	1.60
Density, $\rho[g/cm^3]$	7.75	7.29	7.80	7.43	4.00	4.00	5.00	4.84
Heat capacity, $Cp[J/kgK]$	400.00	580.00	390.00	700.00	769.00	1261.00	500.00	630.00

Table 3.1 presents data showing that the room temperature properties are considerably different than the properties at high temperature. This is critical, particularly in the thermal expansion mismatch, and drives the high strains in the thermally grown oxide. While in this table of parameters the values are discretized for high and ambient

temperature, additional study has shown that this approximation may be able to improve through the course of the synchrotron studies.

### **3.1.3 Loading Conditions and Measurement Methods**

Herein the specifications of the loading and measurements conducted at the synchrotron source at Argonne National Laboratory are presented.

#### **3.1.3.1 Mechanical Loading**

To facilitate mechanical loading, superalloy grips were designed to hold and impart tensile load in line with the servo-hydraulic mechanical load frame. These grips were placed partly in the heating chamber and as such were required to handle the high thermal loads the specimen was exposed to. This challenge was surmounted by using Inconel 718 for the grip material. Type K thermocouples were placed on the top and bottom grips to ensure the integrity of the connection and to identify the amount of conduction taking place away from the sample. Further, environmental thermal measurements were added to ensure the servo-hydraulic thermal state was within nominal conditions. A schematic representation of the loading conditions is presented in Figure 3.3.

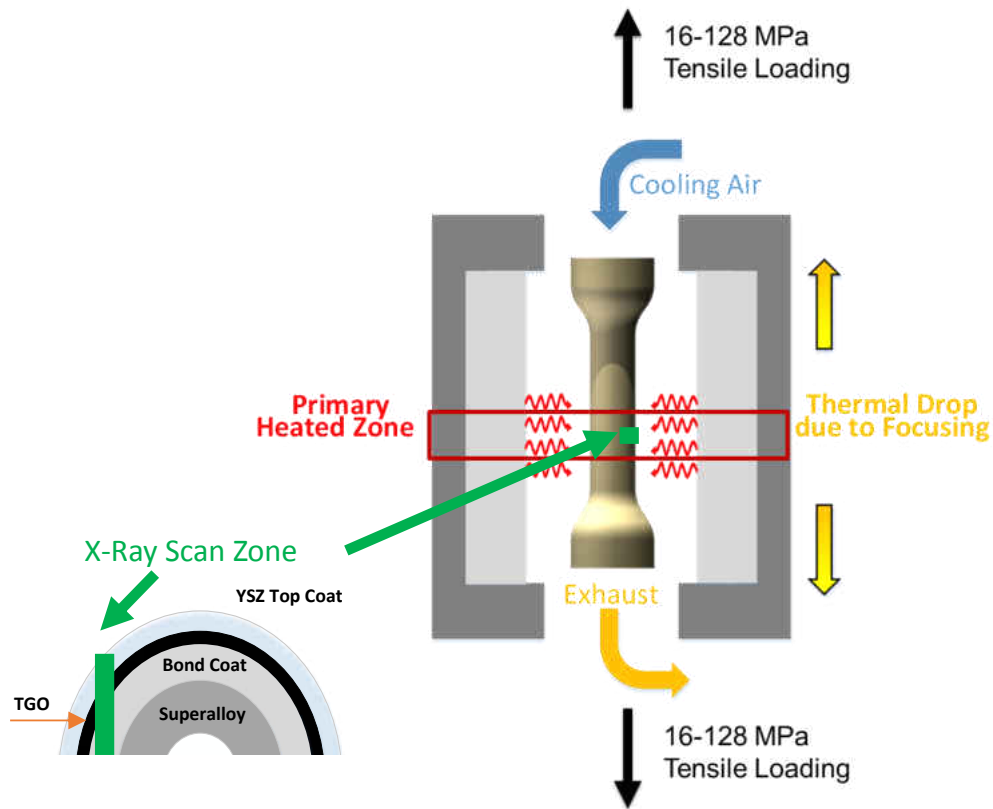


Figure 3.3: Schematic of the thermal gradient and mechanical loading for in-situ X-ray diffraction measurements [91].

### 3.1.3.2 Application of External Heating

High-temperature loading was applied using Precision Controls E4 High-temp Infrared Chamber Heater and Control System (Precision Control Systems Inc., Eden Prairie, MN). The system includes an 8 kW infrared (IR) heating chamber and a control system

with an interconnecting electrical cable. Radiation was applied by four quartz short wavelength lamps in a hinged clam-shell style chamber, focused onto the specimen in the center line of the furnace by way of elliptical mirrors. The chamber has four polished aluminum water-cooled aluminum reflectors to focus the IR energy on the target located in the center of the chamber. The chamber includes four 2 kW T3 lamps, protective quartz windows and dripless water connectors. The control system regulates the voltage to the lamps and includes a temperature controller that was configured for a type S thermocouple for these experiments, for the application's high temperatures. Samples were heated at ramp rates 50 K/min to temperatures up to 1000 °C. This is further documented in supporting publications [116, 76, 90].

### **3.1.3.3 Internal Flow Cooling**

Internal coolant flow was regulated via an Omega mass flow controller (FMA5400/5500) from 0-100 standard liters per minute (SLPM) [116, 76, 90]. The air was cleaned and regulated before entering the mass flow controller to avoid contaminants that could be undesirable at high temperatures. This provided a continuous and tuned supply of air coolant that was passed through the superalloy tensile grips, through the specimen interior, and through the lower superalloy grip before being exhausted into the ambient air. For experiments involving dynamic flow rate control, systematic controls were designed in EPICS (Experimental Physics and Industrial Control System) software.



### 3.1.3.4 Design of Measurements

The X-ray diffraction study utilized the Advanced Photon Source at Argonne National Laboratory, at the Sector 1ID station. Measurements were conducted with a 14 file depth-scan with the grazing technique tangential to the surface, with a  $50\ \mu\text{m}$  step in the depth direction. The data was collected at 5 frames per measurement, with an exposure time of 0.5 seconds per frame. This was done for a representative loading cycle with a high temperature hold at  $1000\ ^\circ\text{C}$  for 20 minutes with 20 minute thermal ramping durations. A schematic is presented in Figure 3.4 for additional clarity.

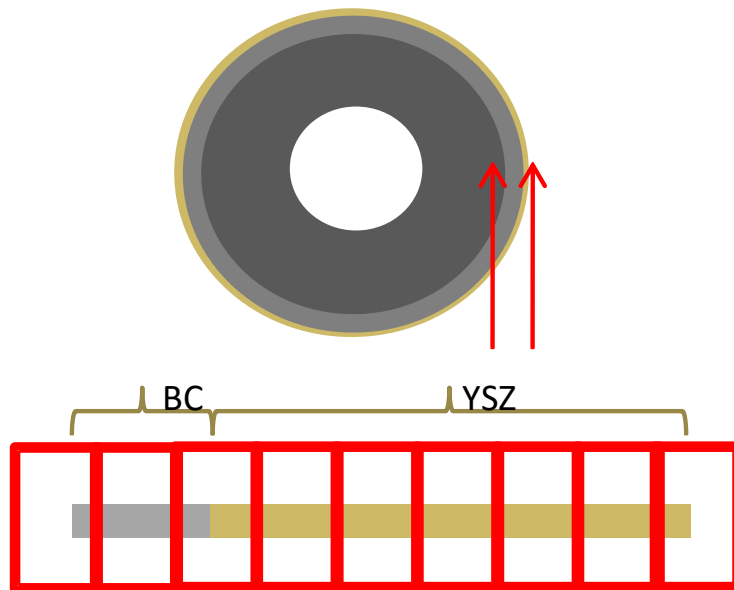


Figure 3.4: Specimen scanning methods in line with the X-ray source [116].

The associated thermal data was also collected from the various thermocouples in the system. Mechanical, thermal, and flow-rate data was collected for secondary measurements along with the X-ray diffraction data. Specifications regarding the design and setup of the in-situ measurement apparatus, along with the calibration of the beam parameters, can be found in the supporting publication [116]. Type S thermocouples, designed and calibrated at the German Aerospace Center, were used in a hoop fashion to measure the surface temperature and to provide feedback for the heater controller to maintain the ascribed surface temperature profile. The setup is further presented in Figure 3.5.



Figure 3.5: Specimen inside radiation heater with visible type S uninsulated thermocouple applied in hoop method for measurement and controller feedback [78].

### 3.1.3.5 Experimental Methodology

This experimental study focused on the aged TBC specimens to investigate the YSZ top coat and the sufficiently thick oxide scale. Experiments were designed to provide a multi-variable assessment of the role and magnitude of the following variables: mechanical

(axial) loading, external temperature, and internal cooling air flow. To understand the influence of the variables, three cases were determined. Unique to this study is the multi variable analysis, showcasing the interaction between the different variables. Herein it is discussed that the superposition of mechanical loading and internal cooling has an influence on the strain evolution, and cause a lag in strain response due to the imparted thermal gradient.

- *Case 1*: constant mechanical loading with variable internal cooling
- *Case 2*: constant internal cooling with variable mechanical loading
- *Case 3*: extrema of variable loading, such
  - Low mechanical loading/low flow rate
  - Mid-range mechanical loading/mid-range flow rate
  - High mechanical loading/high flow rate

These are graphically presented in Figure 3.6 for additional clarity. In tandem, these three cases provide insight into the role of the primary variables; namely, the influence of external loading, internal cooling, and applied mechanical loading.

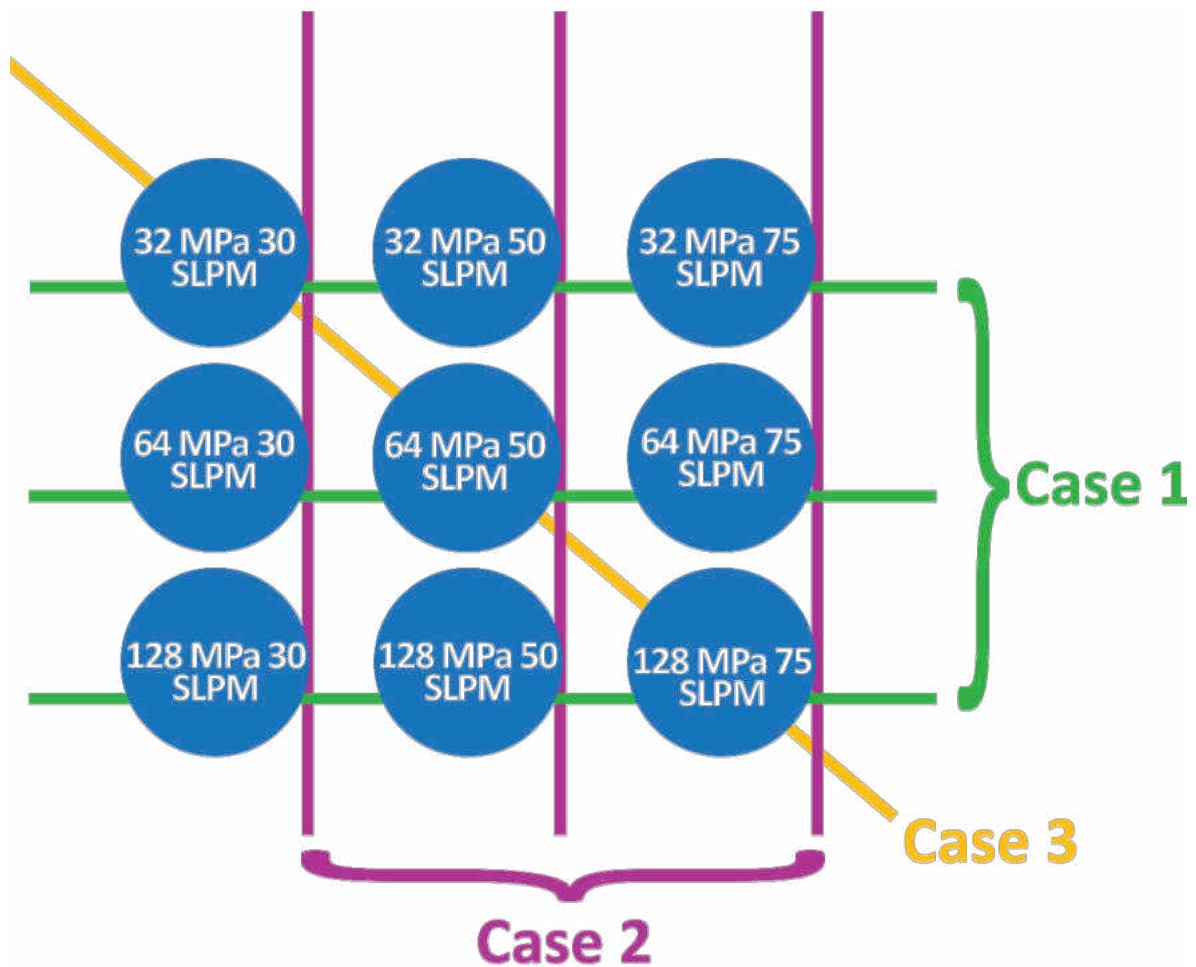


Figure 3.6: Mutli-variable loading experimental matrix for thermal mechanical testing.

**Individual cycles with thermal and mechanical loading:** In-situ strain measurements were designed with variations in both mechanical loads and internal cooling flow for representative cycles. Testing conditions included a 20 minute ramp from ambient to 1000 °C, a high-temperature hold for 20 minutes, and a decrease to ambient for 20

min. Additionally internal cooling air flow was implemented, with a mass flow between 0 and 100 Standard Liters Per Minute (SLPM).

Figure 3.7a represents the conditions employed on the specimen, during which depth strain measurements over the coating thickness were conducted. Cycles with superimposed constant mechanical loads providing a nominal tensile stress of 32, 64, and 128 MPa were paired with flow rate variations of 0, 30, 50, and 75 SLPM. This is detailed in Figure 3.7b. This produced a large matrix of results shedding light on material properties as a function of temperature, mechanical loading (stress), and dwell time; and the methodology has been detailed in supporting work [90].

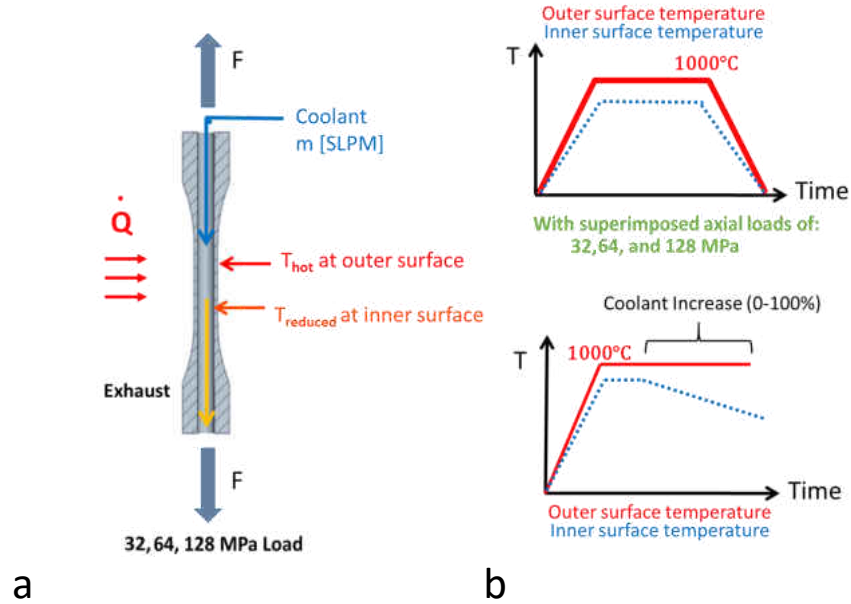


Figure 3.7: Loading methodology: a) Application of variable loading influences. b) Cycle loading schematics for individual cycles and flow rate study at high temperature [90].

**Increasing flow rate:** In an effort to identify the variation in strain for the coating system at a high temperature with respect to internal cooling, this experiment was conducted. After the surface of the coating system was stabilized at 1000 °C, the internal cooling flow was engaged and increased in small discrete steps accompanied by in-situ diffraction strain measurements. Measuring through the depth of the coating, the influence of the increasing flow rate on the strain of the YSZ top coat and TGO oxide scale was observed. Internal temperature measurements have proven highly difficult to implement, due to the difficulty to get accurate results from direct temperature measurements

through means of thermocouples or using a pyrometer; the methodology implemented has been detailed in Figure 3.7 and in publication [90]. From prior work [75], a maximum temperature gradient was measured at 135 °C at the full 100 SLPM internal cooling flow and was determined via the evolutions of crystallographic axis.

**Creep testing:** Investigations were made to determine the viscoelastic response by heating the specimen to high temperature and holding for stability at 800 °C and 1000 °C. At this high temperature hold, an instantaneous applied mechanical load of 128 MPa was engaged, with force control, to induce a visco-elastic response. This loading schematic is presented in Figure 3.8. Diffraction strain measurements measure elastic strain by identifying variations in the crystalline lattice spacing, but the measurement of how the elastic response decays can shed light on the inelastic high temperature mechanics.



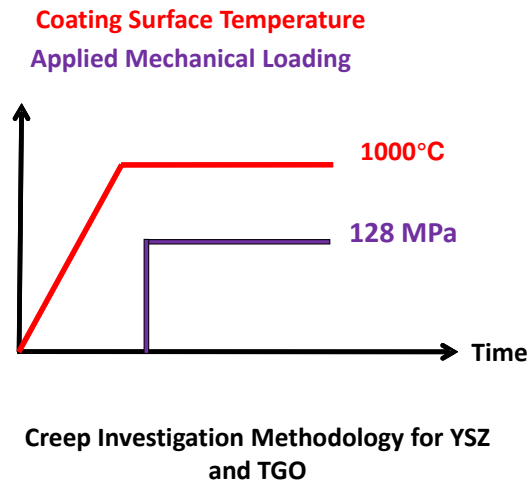


Figure 3.8: Loading conditions to measure viscoelastic response via synchrotron lattice spacing.

### 3.2 Ceramic Matrix Composites

Ceramic matrix composites for high temperature aerospace environments experience critical loading on the hot gas side by extreme temperatures and high compressive stresses, which can lead to high creep inducing response. The experimental and numerical simulation of the creep response required to understand the composite material's response, and to predict life time expectancy and performance in service, has suggested the need

for further testing and material characterization [6, 56, 4]. Of particular interest is the mechanical response of the high porosity matrix, which evolves with high temperature exposure, this is described in the proceedings manuscript [89]. The applied loading results in complex load partitioning between the highly porous matrix and strong reinforcement fibers.

The loading methodology varies in part from the testing of the thermal barrier coating system, but shares many details in common including segments of the equipment that were interfaced the Advanced Photon Source X-ray beam. This is detailed in the following subsections.

### **3.2.1 Sample Design**

Specimens were designed from WHIPOX<sup>TM</sup> ceramic matrix composites, which comprise Nextel<sup>®</sup> 610 alumina fiber bundles and a porous ceramic matrix. The composite is then produced by a computer controlled winding process with thermal processing [111]. The standardized weight of the fiber bundles is approximately 3000 denier, which is equivalent to 700-800 fibers with an estimated individual 11 micron diameter. For processing the raw composite, the fiber bundles are infiltrated by aqueous slurry of alumina particles. Drying and subsequent pressure-less sintering of the green body results in composite with a highly porous matrix, which provides the damage tolerant mechanical behavior of the CMC. The composite can be produced in a near net shape, making it an excellent candidate for next

generation combustion liners [43, 79]. For X-ray diffraction and radiography studies at the Advanced Photon Source, cuboid samples were designed with quasi-unidirectional fibers ( $\pm 2^\circ$ ) and were shaped to 5 x 5 x 10 mm. This is described in the proceedings manuscript [89]. Tomography specimens were designed using ultrasonic drilling to create the precise 1.6 mm diameter specimens by 3.2 mm in height, which was stipulated based on the diameter of the beam.

Representation of the specimen size and geometry is presented in Figure 3.9.

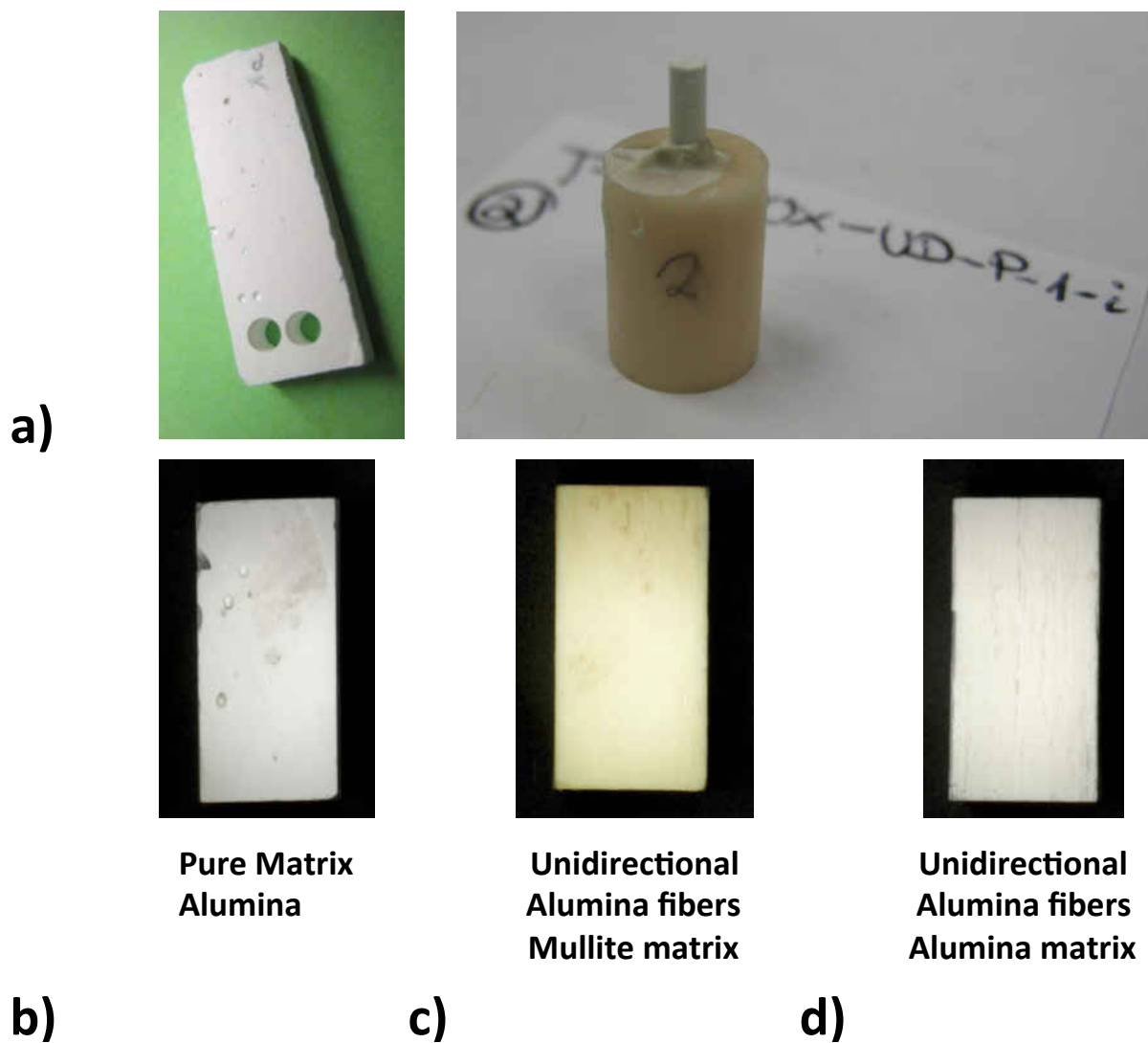


Figure 3.9: Design of WHIPOX<sup>TM</sup> specimens for thermal and mechanical testing (diffraction) and quantitative imaging (tomography): a) preparation of tomography specimens with ultrasonic drilling and mounted tomography specimen, b) pure  $\alpha$ -alumina matrix material, c) unidirectional composite with  $\alpha$ -alumina fibers and Mullite matrix, and d) full  $\alpha$ -alumina fiber reinforced composite.

### 3.2.1.1 Specimen List and Nomenclature

A large number of specimens were designed for this study and were named according to their properties. The nomenclature for the specimen naming is presented here in Table 3.2.

Table 3.2: Specimen naming nomenclature for WHIPOX<sup>TM</sup> samples.

Example Naming	Abbreviations	Description	Designation
T-Whipox-45-P-1-i	UD	Unidirectional	Diffraction or tomography
D-EBC-Whipox-45-VF-A-1	VF	Vertical Fibers	Description
	OA	Off loading axis fibers	Processed or Aged
	EBC	Envir. Barrier Coating	Specimen number in group
	45	plus minus 45 fiber weave	Initial or Final following annealing

Specimens were designed for either tomography or diffraction experiments, resulting in different sizing for matching the application based on the X-ray beam size for each measurement technique. The full specimen list for the study conducted at the beamline is provided here in Table 3.3.

Table 3.3: Specimen listing for tomography and diffraction experiments.

<b>Tomography Specimens</b>	<b>Diffraction Specimens</b>
T-Matrix-P-1-i	D-Matrix-P-1
T-Whipox-UD-P-1-i	D-Matrix-A-1
T-Whipox-45-P-1-i	D-Whipox-UD-VF-P-1
T-Whipox-UD-A-1	D-Whipox-UD-VF-A-1
T-Whipox-45-P-CR	D-Whipox-UD-PF-P-1
T-Whipox-45-A-1	D-Whipox-UD-PF-A-1
T-FB-NX720-ALOX-1	D-Whipox-UD-MM-VF-P-1
T-FB-NX610-ALOX-1	D-Whipox-UD-MM-PF-P-1
T-Matrix-P-1-f	D-Whipox-45-LD-P-1
T-Whipox-UD-P-1-f	D-Whipox-45-LD-A-1
T-Whipox-45-P-1-f	D-EBC-Whipox-45-OA-P-1
	D-EBC-Whipox-45-OA-P-2

Microscopy was conducted on the specimens and allowed for quantifying the dimensions along with defect assessment. Specimens with zones damaged during manufacturing were not selected for investigation, and multiple specimens were produced per batch. Specimens produced to the specifications of the tomography experiment are presented in Figure 3.10. Specimens were manufactured with either ultrasonic drilling of bulk plate material at a diameter of 1.6 mm, and from continuous infiltrated fiber bundles with diameters between 1 mm and 1.3 mm. This discrepancy in diameter is due to the pro-

cessing techniques for the fiber bundle. From the microscopy, complex micro-structures are observed. In Figure 3.10b the coating thickness of the environmental barrier coating is observed to be 895 microns, and coats the ceramic matrix composite substrate. Figure 3.10c identifies the large external cracks through the Mullite matrix of the 1 mm fiber bundle specimen, which can be compared with the all alumina composite in Figure 3.10d with a 1.6 mm diameter.

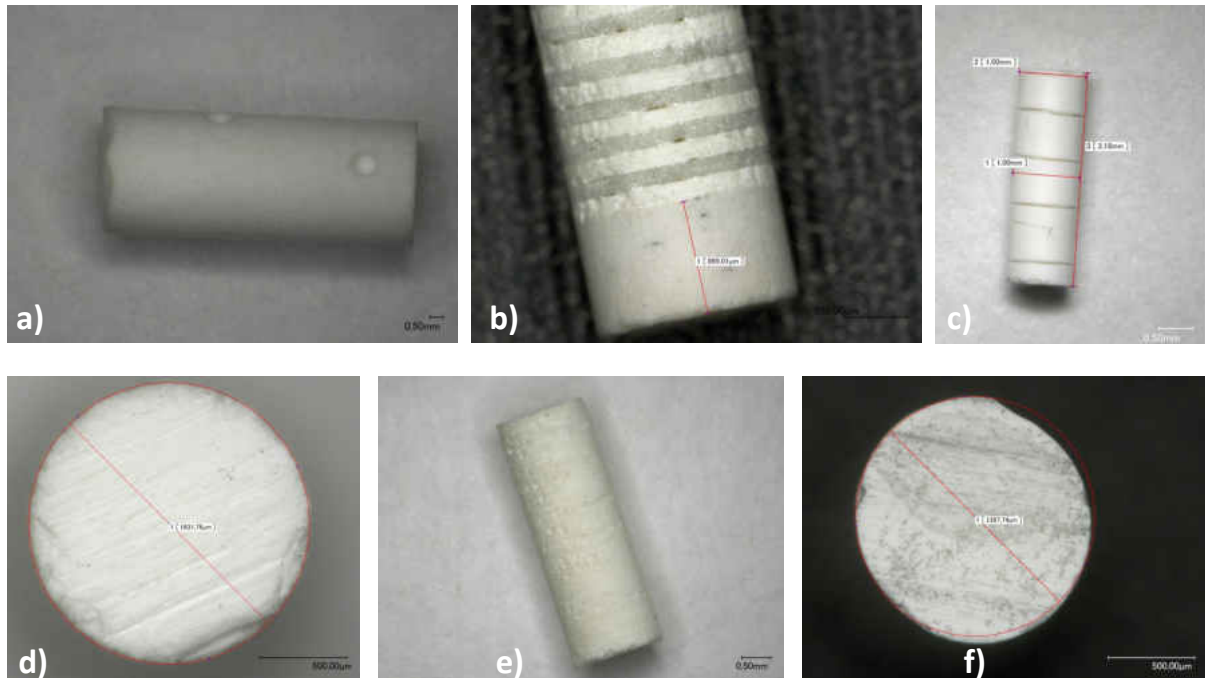


Figure 3.10: Specimens designed for tomography measurements: a) pure matrix specimen, b) EBC coated Whipox substrate, c) Alumina fiber bundles infiltrated with Mullite matrix, d) perpendicular uni-directional all alumina composite after aging, e) perpendicular uni-directional all alumina composite, and f) vertical uni-directional all alumina composite.

Cuboid specimens designed for x-ray diffraction were examined in Figure 3.11. All specimens conformed to the similar dimensions of 5 x 5 x 10 mm.

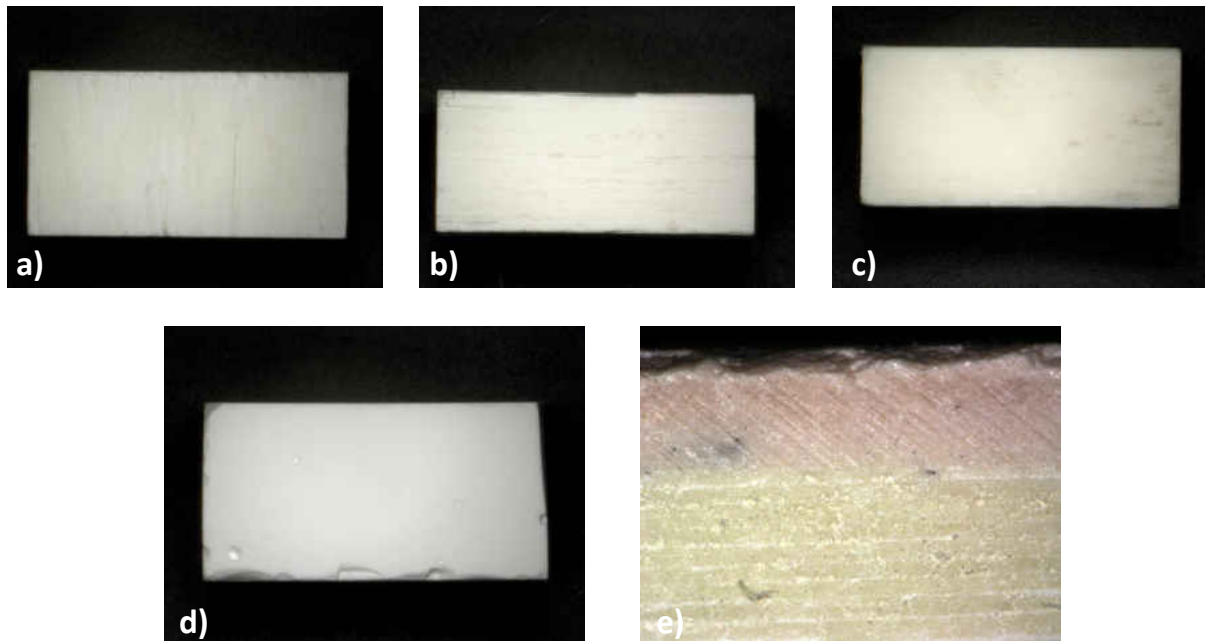


Figure 3.11: Specimens designed for diffraction measurements: a) perpendicular fiber alignment of all alumina composite, b) vertical fiber alignment of all alumina composite, c) Alumina fiber with Mullite matrix composite, d) pure matrix specimen, e) all alumina composite with yttria environmental barrier coating deposited.

Figure 3.10a, b, and c capture the specimens with variations in fiber orientation and with Mullite matrix inclusion, while in d the pure matrix specimen observed. The environmental barrier coated substrate is presented in Figure 3.10, with the pink hues from the coating.



### 3.2.2 Material Properties

The material properties of Whipox all oxide ceramic matrix composites have been explored by researchers [80, 111, 115]. Assessment of the mechanics of the composite is complex and processing techniques can leave high variation across the bulk plates that are formed, and this variation causes the mechanics and failure mechanisms to be more difficult to predict [109, 106]. Schmäcker et al [109] found that compression on the raw materials during the moist stage encouraged a more homogenous distribution of the inter-laminate matrix agglomerations, of which large agglomeration may be the critical defect structure. The design of the composite results in complex anisotropic elastic properties [106], and variations in fiber or matrix composition from pure alumina, alumino silicate, or mixed material result in different behaviors. The material properties vary between them, where use of Mullite can help to limit high temperature sintering and diffusion but trades strength. These properties are provided in Table 3.4.

Table 3.4: Material properties variation for all alumina composite, alumina matrix with Mullite fibers, and Mullite matrix and alumina fibers [111].

	Nextel 610 + Al <sub>2</sub> O <sub>3</sub> -Matrix	Nextel 720 + Al <sub>2</sub> O <sub>3</sub> -Matrix	Nextel 720 + Mullite Matrix
<b>In-Plane-strength</b> [MPa]	280 ± 20		130 ± 3.6
<b>ILSS</b> [MPa]	8.0 ± 2,5	9 ± 2	
<b>Young's Modulus</b> [GPa]	140 ± 14	110 ± 11	

The backbone of the WHIPOX<sup>TM</sup> specimens utilized in the study are woven Nextel 610 fibers drawn of pure  $\alpha$ -alumina. The fibers are woven on a 3D computer controlled winding machine into complex near net shapes. The fibers have excellent axial strength and retain their strength far into high temperature applications. A Weibull study has been conducted in literature [132] to understand the average strengths and diameters of the reinforcement fibers, and is presented here in Table 3.5.

Table 3.5: Material properties of pure Nextel 610 alumina fibers [132].

	Mean Strength	Strength	Diameter	Guage Length
Lot	MPa	Distribution	Distribution	Dependence
A0168	3080	10.9	2.7	
A0180	3030	11.2	2.6	
A0184	3500	12.1	4	
mean	3200	11.4	3.1	21.7

### 3.2.3 Loading Conditions and Measurement Methods

Diffraction measurements were performed at energies of above 65 keV. The data was collected with a 2D GE-41RT area detector at 1 frame with an exposure time of approximately 0.5 seconds per frame over 10 frames. Radiographic imaging was conducted during the ramping periods and during holding periods in conjunction with diffraction

measurements, where the diffraction detector and imaging camera could be interchanged rapidly. Radiographic imaging was conducted with a Retiga 4000DC charge-coupled device with 2048 x 2048 pixels. Imaging parameters were set for a 0.2 second exposure time with a frame rate of 30 frames per second.

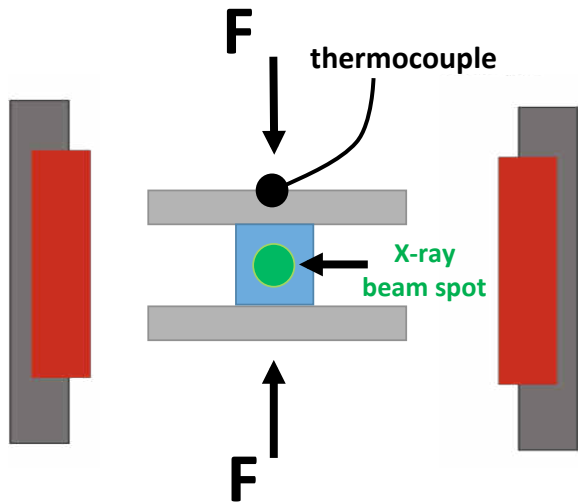
Tomographic analysis was made possible with an Aerotech air bearing rotary stage (ABRS-300MP) stack, with a resolution of  $0.174 \mu\text{rad}$ . A step size of  $0.2^\circ$  was used to capture  $360^\circ$ , resulting in 1800 images captured for reconstruction of the 3D volume. The same Retiga 4000DC charge-coupled device with 2048 x 2048 pixels was employed for measurement. Voxel size was determined as 1.3 microns with a uniform pixel shape.

Debye Diffraction rings were collected and analyzed for phase identification, grain characteristics analysis, and strain diffraction measurements [89]. Shadows of partial obstructions are identified on the 2D area detector, from the measurements conducted in 2014, which interfered with some of the outer diffraction rings. However, the effect is isolated to the exterior rings. Thermal measurements were collected via custom type S thermocouples produced and calibrated at the German Aerospace Center, and were employed in contact to the specimen's loading plate. Type K thermocouples around the system were used to monitor the system as to ensure the performance envelope of the system was not exceeded due to the extreme temperatures.

### 3.2.3.1 Mechanical Loading

Applied uni-axial compressive loading was delivered by using alumina push rods to transfer the load from the superalloy grips in line with the mechanical load frame of a MTS test machine (type 858), provided by the Advanced Photon Source at Argonne National Laboratory. Two WHIPOX<sup>TM</sup> support plates between specimen and ceramic push rods mitigated loading friction, and alignment was ensured by an in-line spherical ball of alumina placed below the specimen's lower support plate.

This has been detailed in proceedings [89]. An image of the compressive loading setup is presented in Figure 3.12.



**a)**



**b)**

Figure 3.12: Design of thermal and mechanical loading for Whipox: a) schematic of loading and measurement, and b) image of test setup including Whipox shielding for superalloy grips [89].

### 3.2.3.2 External Heating

In order to provide the extreme temperatures and heat flux required for appropriate testing, a new more powerful heater was designed with the support of Precision Controls E6 High-temp Infrared Chamber Heater and Control System (Precision Control

Systems Inc., Eden Prairie, MN). The system includes a 12 kW infrared (IR) heating chamber and a control system with an interconnecting electrical cable. The IR heater uses six short wavelength lamps in a hinged clam-shell style chamber. The chamber has six polished aluminum water-cooled aluminum reflectors to focus the IR energy on the target located in the center of the chamber. The chamber includes six 2 kW T3 lamps, protective quartz windows and dripless water connectors. Additional air cooling can be applied to the quartz halogen bulbs to lengthen the life duration of the equipment. The control system regulates the voltage to the lamps and includes a temperature controller that was configured for a type S thermocouple for these experiments. This allows for increased temperature of upwards of 1500 °C. For this testing, the surface temperature was measured by a type S thermocouple designed and calibrated at the German Aerospace Center, implemented in contact to the upper WHIPOX<sup>TM</sup> support plate of the sample. Thermal loading brought the surface temperature to 1200 °C. Above this temperature, this ceramic matrix composite is still effective in application but begins to sinter and revert to the bulk material. As such, the critical applications desirable for testing will remain below the maximum capacity of the testing equipment as well as the ceramic's true limitations. An image of the thermal setup is presented in Figure 3.13 showcasing the equipment. Secondary type K thermocouples were utilized to measure the grip material and shielding to identify any deviation in the temperature profile and to ensure the loading conditions were within nominal standards. Inconel 718 loading grips were shielded from the radiation lamps by WHIPOX<sup>TM</sup> crucibles machined to enclose the ce-

ramic loading rod, and additional air cooling was employed to protect the fixtures from the long duration heat exposure.

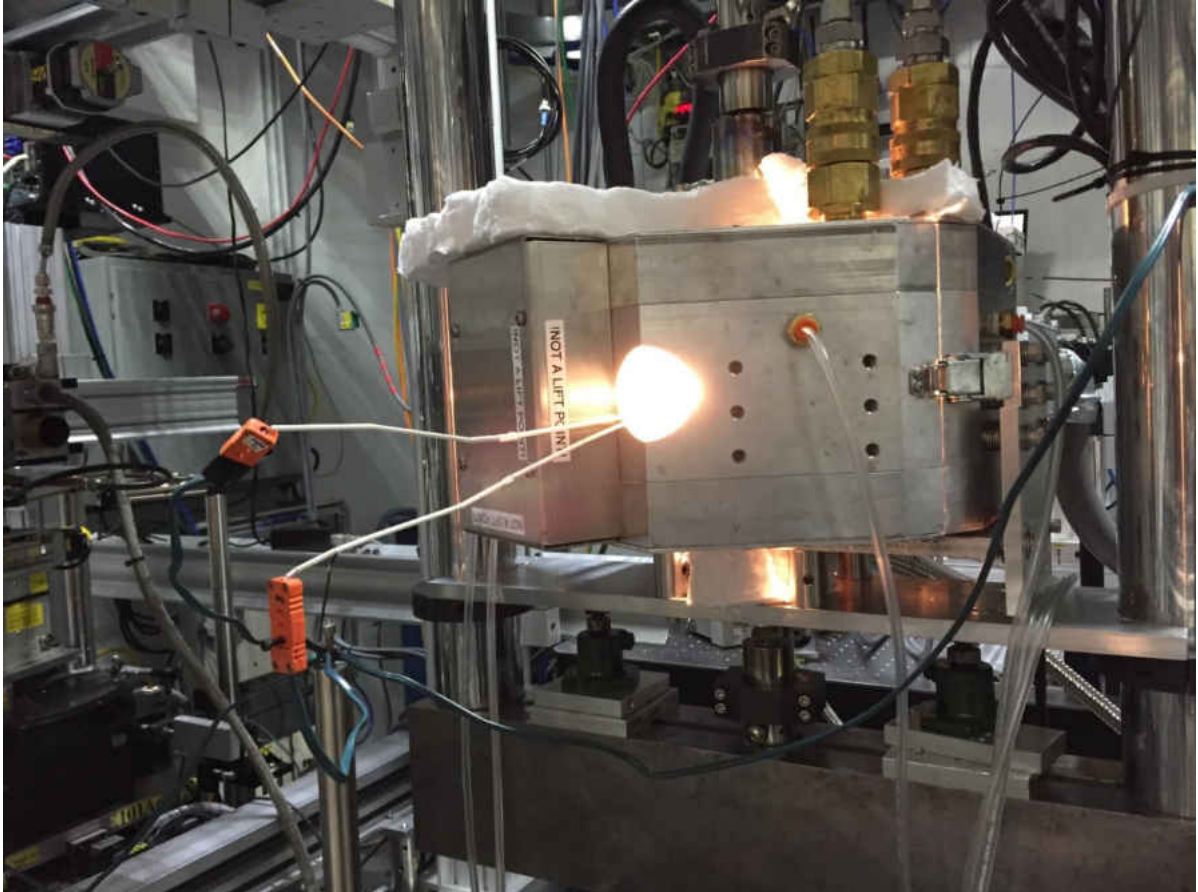


Figure 3.13: Ultra-high temperature heating chamber with measurement devices interfaced at synchrotron beamline and mechanical loading test frame.

### 3.2.3.3 Experimental Methodology

Diffraction experiments were conducted for cuboid WHIPOX<sup>TM</sup> specimens in an effort to determine the XRD and mechanical properties for each specimen with temperature and applied mechanical loading. This was done in an effort to explore the fiber vs matrix strain and load partitioning. For isolating the diffraction response for the fiber and matrix, the intention was to apply loading to force separation due to the nature of the elastic modulus varying by a factor of at least five [56, 6] and the grain size being extremely dissimilar. The loading methodology is specified in schematic form in Figure 3.14.



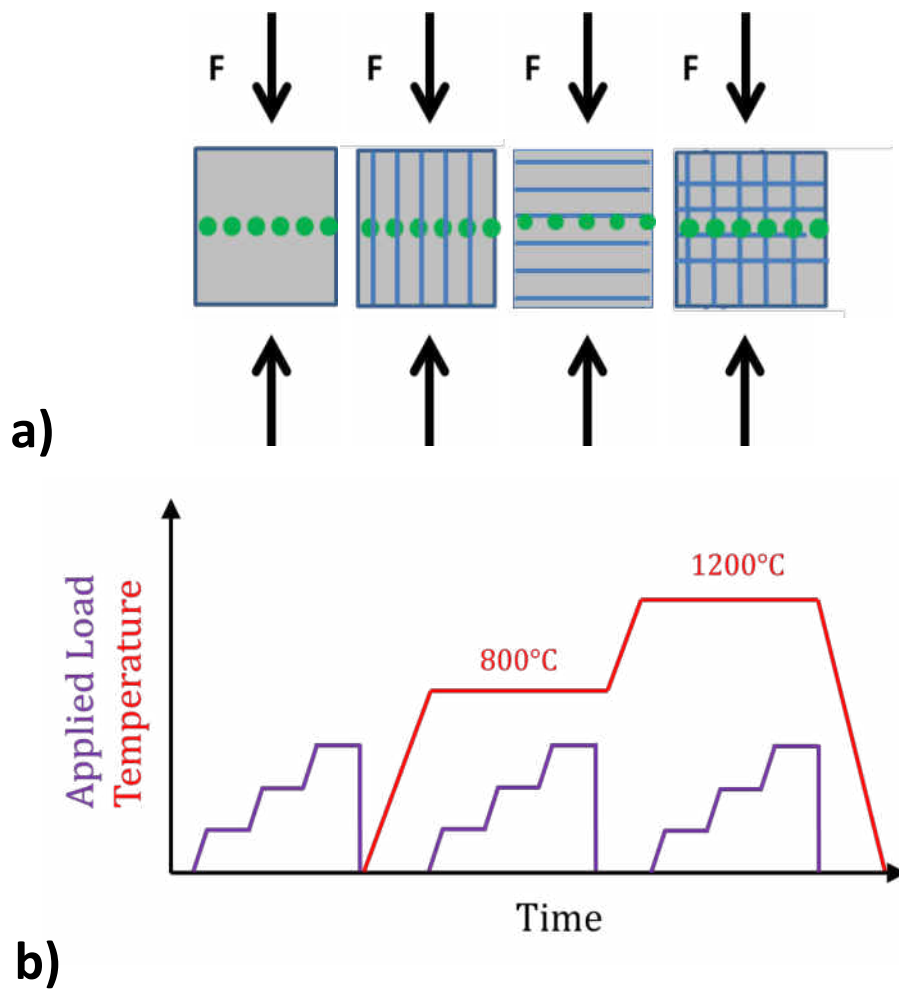


Figure 3.14: Experimental methodology: a) variations of neat WHIPOX<sup>TM</sup> specimens loading orientation, b) Thermal and mechanical loading profile for neat WHIPOX<sup>TM</sup> specimens of varying fiber orientations.

Five scan points were taken across the surface of the neat specimens to identify any variation from edge effects and macro-scale defects. Thermal ramping was applied at 30 °C per minute to an initial hold of 800 °C, and a designed high temperature condition

of 1200 °C. Mechanical loading steps were designed for nominal, 10 MPa, 20 MPa, and 30 MPa. However in practice the loading was changed to nominal, 15 MPa, and 30 MPa due to time constraints at the beam line. Additionally the pure matrix specimens were limited to only 10 MPa due to their fragile design.

Tomographic measurements were conducted for a large set of specimens to analyze variations in porosity and micro-structure due to fiber orientation as well as additional aging after processing. Measurements were designed for high temperature, but due to equipment limitations at the beamline these were unfortunately omitted.

## CHAPTER 4 INVESTIGATION OF THERMAL BARRIER COATINGS

In this study, in-situ X-ray diffraction data of tubular coated and aged specimens were collected under multi-variable loading conditions capturing their influence on the strain of thermally grown oxide layer and ceramic top coat in a TBC system. A multi-variable analysis has been conducted to determine the role and effect of the following variables: mechanical (axial) loading, external temperature, and internal cooling air flow. The mechanical testing rig is interfaced directly with the synchrotron X-ray beam allowing for in-situ high temperature measurements with applied mechanical loading.

### 4.1 Objectives

The primary study on the thermal barrier coating system was designed to meet three objectives. These objectives developed the three primary experiments featured in Chapter 3.

- *Objective 1:* Conduct full multi-variable analysis to determine the influence of loading variables during cycle evolution for YSZ and TGO ceramic layers
- *Objective 2:* Determine creep response and influences on viscoelastic mechanics
- *Objective 3:* Identify design elements for increased durability through tuning of system mechanics

From these main objectives, the experiments were designed to explore the strain response and evolution in the oxide scale and zirconia top coat. Measurements were taken during ramp up, high temperature hold, and ramp down for the cycle studies. Additional experiments for the influence of flow rate and viscoelastic response were conducted to supplement these measurements to more completely understand the loading influences.

## **4.2 Advances in Complex Diffraction Ring Fitting**

Fitting consideration is important to note for interpreting the strain results. This is particularly important for the low diffraction volume of the TGO oxide scale. Each resulting data point is a fit of an eccentric ellipse from the Debye rings produced by that crystallographic plane under strain. However through transmission scanning of the specimen captures multiple constituents simultaneously that can convolute and obscure diffraction rings for analysis. Herein a discussion on the challenges with the diffraction analysis, and the methods to overcome the complexity, are presented and discussed.

### **4.2.1 Resolving Oxide Scale Diffraction Rings under Interference**

For the alumina oxide scale, the (116) plane was selected as it had the minimum convolution with the bond coat peaks. However, at high temperature there is considerable thermal expansion and bond coat phase change due to precipitates. Approximately 4

scans across the thickness had alumina oxide peaks of varying intensity, however proceeding deeper into the specimen yielded additional bond coat precipitations that can convolute and obscure the faint oxide layer. Some of these considerations are shown in Figure 4.1.

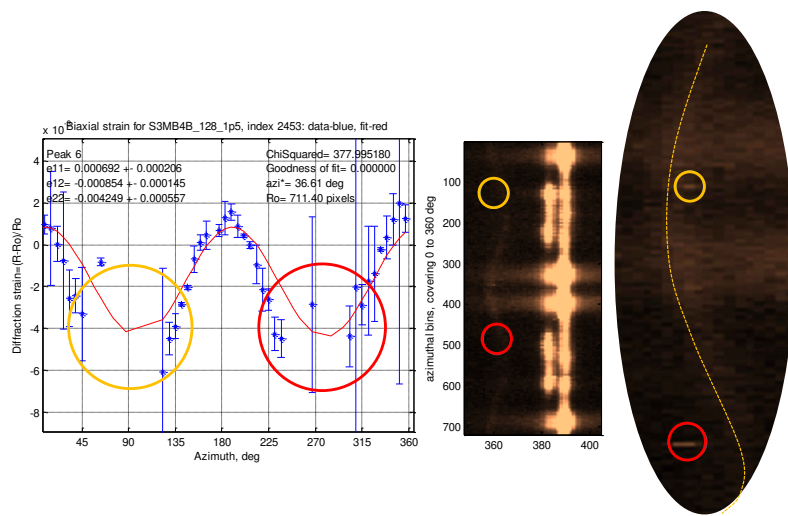


Figure 4.1: Fitting challenges for transformed Debye rings. Small bond coat precipitate beginning to skew the fitting of the thermally grown alumina oxide.

To mitigate this, a Fourier fitting method was employed to overcome fitting challenges where segments of the oxide were obscured by the bond coat. Distinguishing between the two overlapping phases was made more certain by the texturing or roping of the bond coat phases [24, 77], as well as its dramatic intensity difference in comparison to the

oxide. Error bars are generated for the average radius for all of the specific azimuthal bins segmented around the Debye ring. The full discretized ring is fit by a Fourier routine that considers all points. Confidence intervals are constructed for 90% confidence, providing an understanding of the variation for each strain fit. Error bars represent the maximum and minimum confidence range for each measurement point. For outliers multiple standard deviations away from the average, a bisquare robust regression is used to weight their influence on the full fitting curve. This is particularly effective for issues with bond coat peak interference, as seen in Figure 4.2a where azimuthal bins will fit neighboring higher intensity bond coat peaks and miss the obscured oxide scale peak. The stronger the data matches the Fourier sinusoidal shape, the stronger the predictive nature of the routine becomes. For strong signals with small areas of obscured data, this could include textured or interfered data segments, the routine is very effective for capturing the appropriate fits as seen in Figure 4.2b. An R-squared value for each fit is determined and used to determine the goodness of fit for every measurement point to further quantify the success of each strain fit. This improved the quality of the sensitivity of the analysis and allowed for a more accurate assessment of high temperature measurements with lower strain magnitudes.

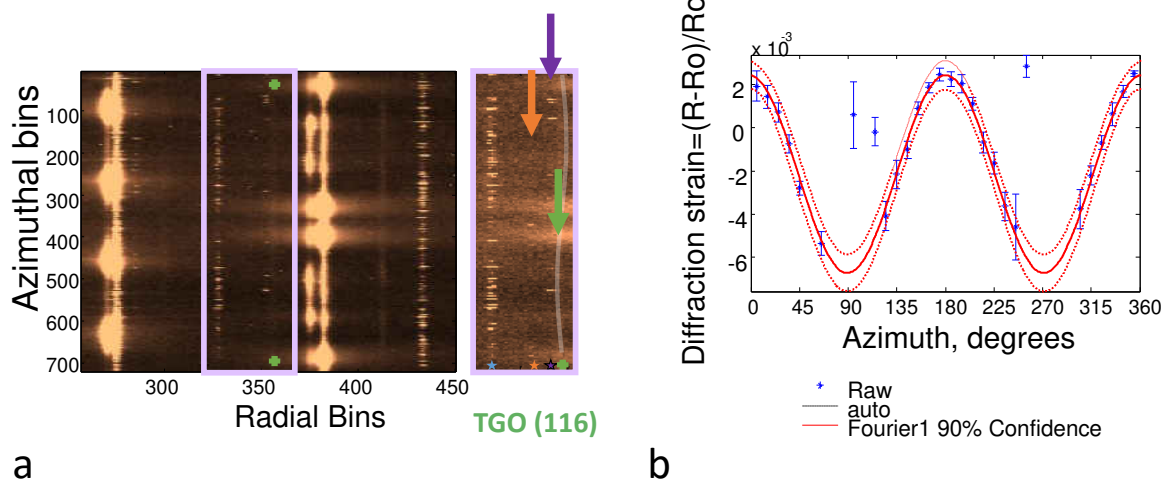


Figure 4.2: Solutions to fitting alumina peaks with obfuscation: (a) Examination of transformed Debye rings with precipitates obscuring oxide layer ring. Secondary peaks marked in blue interfere with faint oxide scale peak marked in green. (b) Fitting challenges for strain response with bond coat overlap over alumina peak.

#### 4.2.2 YSZ Texturing

As the XRD scanning investigations capture the through depth information, internal layer scans capture a combination of the diffraction rings including the bond coat, TGO, and YSZ top coat. Figure 4.3a shows the full response from the TGO interface with all con-

stituents present. The influence of peaks overlapping from multiple constituents causes challenges while fitting for strain analysis, but it is possible to overcome as discussed in Subsection 4.2.1. Investigating the YSZ through thickness strains was accomplished in prior work [78] and yielded findings relating the change in stiffness through the depth of the columnar structure. However, for the aged specimen the peak commonly used for strain analysis (111) at  $2.96 \text{ \AA}$  was not visible at the tangential surface level scans. This is seen in Figure 4.3b. Scanning further into the depth revealed a highly textured peak that gradually shifted into a less preferred orientation complete ring, as presented in Figure 4.3c.



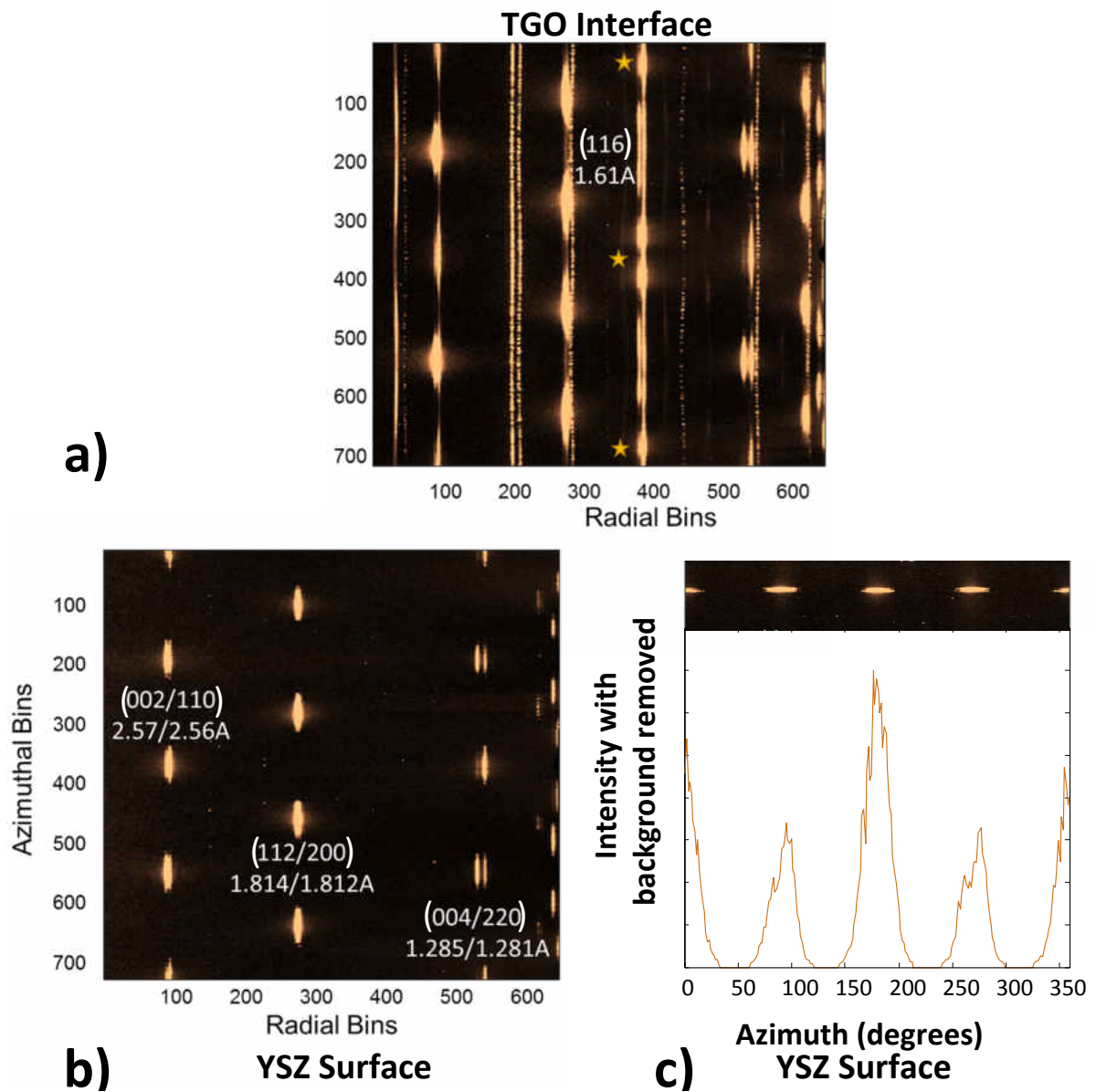


Figure 4.3: Variation in texturing for YSZ: a) multi-constituent diffraction patterns from interior TGO interface, b) textured YSZ diffraction pattern from tangential surface scan with (111) plane not visible, and c) quantification of YSZ (111) texturing pattern from sub-surface scan where plane becomes visible.

As this type of diffraction response varied from the prior investigations, it led to considerable questions as to what could cause the variation. Investigating the processing parameters, including rotation speed during deposition, it was found that the primary factors that can deviate the micro-structure were held constant [140, 112, 138]. It was concluded that the influence of variable columnar pointing, which can deviate across the axial length of the specimen due to deposition contact angle [114], was the cause of the change in texturing from the as processed specimen. Due to these challenges, the strain results reported in this manuscript are from the location at the interface between the YSZ and TGO where the texture effect was not as prominent.

### **4.3 Strain Evolution**

The experiments produced high-resolution 2D diffraction data yielding the systems' constituents strain data of the multi-layer system. This work offers the capacity to use the measurement results to establish design strategies for internal cooling that would prevent the generation of tensile strains within the TGO for jet engine blade coatings, potentially designing to avoid damage mechanisms and extending durability.

### 4.3.1 TGO Investigation

A full multi-variable testing procedure was performed to understand and quantify the influence of the mechanical loading, thermal loading, and internal cooling testing parameters. Of primary importance was the comparison of constant mechanical load with variable flow rate and constant flow rate with variable mechanical loading. Comparing the resulting 9 individual full system tests, Figure 4.4 was produced for the primary comparison. From Figure 4.4a, b, c the role of mechanical loading against variable flow rate can be deduced. Increasing internal coolant flow drives the thermally grown oxide scale, comprised of  $\alpha$  alumina, to be increasingly in compression. Application of axial tensile loading has the influence of driving the oxide scale increasingly into tension. As seen in the  $e_{22}$  strain evolution for the testing profile in Figure 4.4b, c, these competing factors draw the oxide layer increasingly closer to the strain free condition from compression, or even draw it into the tensile condition if sufficiently loading. Further, in Figure 4.4d, e, f, the response was re-plotted for the comparison of the in plane  $e_{22}$  strain evolution for constant flow rate with variable mechanical loading is presented. The full matrix of the multi-variable testing to compare the influences of mechanical loading and internal coolant flow in conjunction with a thermal cycle profile is presented in Figure 3.6. Resulting strain evolution profiles are presented for the oxide layer. From these findings, the trends and influences of the multiple variables and their effect on the oxide scale can be identified and discussed.

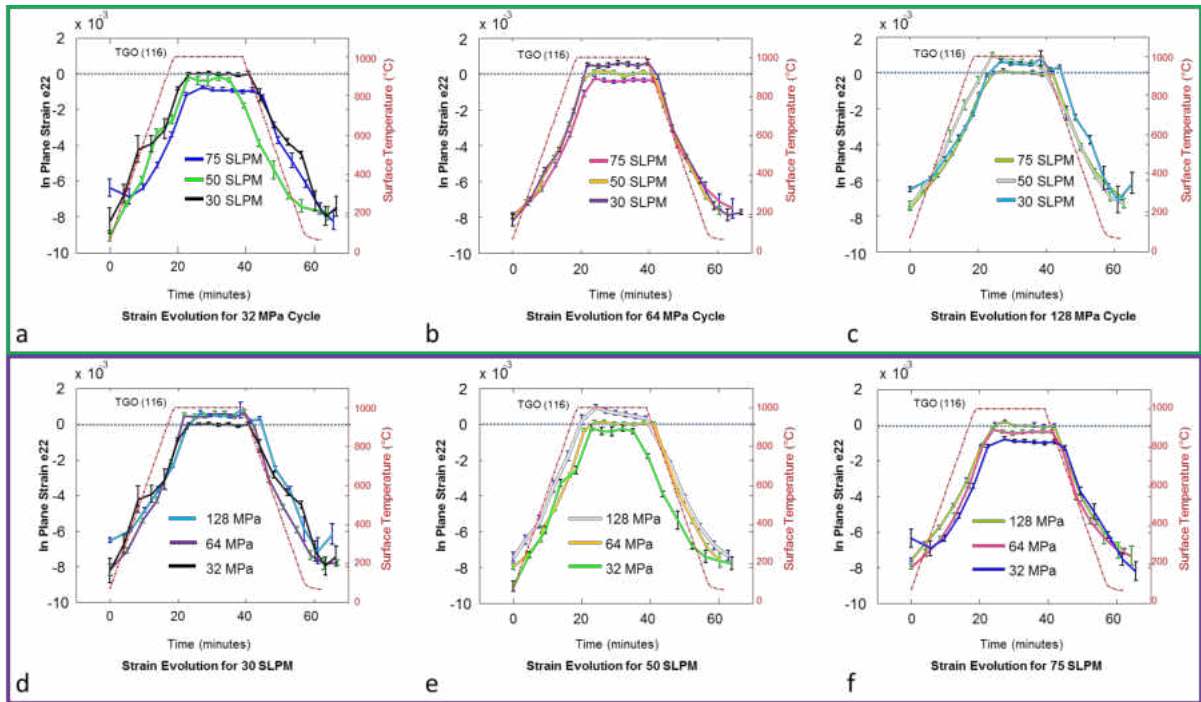


Figure 4.4: TGO  $e_{22}$  strain response over thermal cycle for constant mechanical load with varying flow rate (a, b, c); and re-plotted for constant flow rate with varying mechanical loading (d, e, f).

The second objective of the study was to evaluate each variable's influence. This was achieved by taking Case 3, as detailed in the Figure 3.6, which tested mechanical loading-internal cooling at low-low, mid-mid, and high-high conditions over the applied external thermal loading temperature profile for the cycle. Figure 4.5a and b show the strain evolution for both in plane and out of plane ( $e_{22}$  and  $e_{11}$ ) for the tubular test specimens. This extrema testing provides the opportunity to compare the dominance of each variable against each other, shedding light on the true mechanics of the layers.

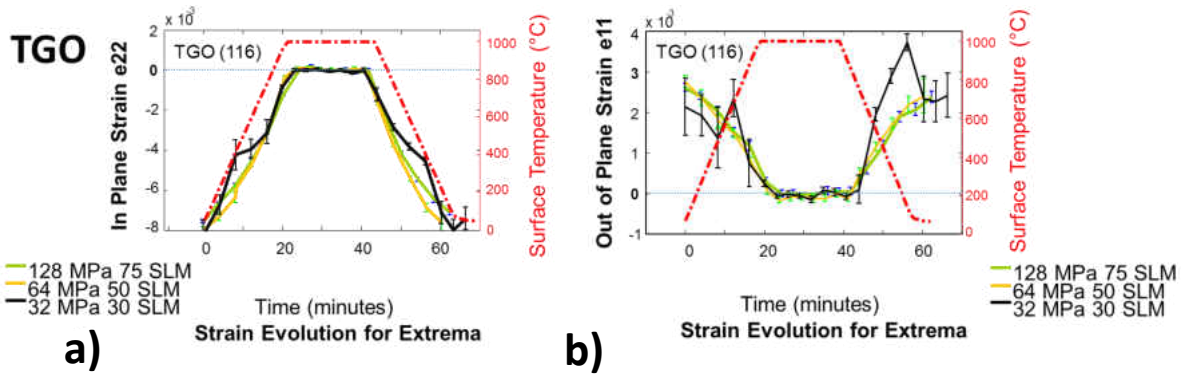


Figure 4.5: (a, b) Extrema testing strain evolution of low, medium, and high mechanical load and internal flow rate.

In Figure 4.6 the experiment to determine the influence of internal flow rate and the resulting strain evolution for the thermally grown oxide scale is presented. While at a constant surface temperature of  $1000^{\circ}\text{C}$ , internal cooling flow rate was gradually increased from 0 SLPM to 85 SLPM. The resulting in plane and out of plane ( $e_{22}$  and  $e_{11}$ ) strain results are plotted, and the influence of increasing coolant can be quantified. The trends follow an expected non-linear response, which results from the heat transfer coefficient being non-linear for transitioning internal pipe flow [2, 130]. This is seen to level out the resulting strain response between 40 and 60 SLPM. For the  $e_{22}$  response, the maximum flow rate is observed to result in  $-1.5 \cdot 10^{-3}$  (compressive) strain. Conversely for  $e_{11}$  response, the maximum flow rate increases the strain to  $4 \cdot 10^{-4}$  (tensile).

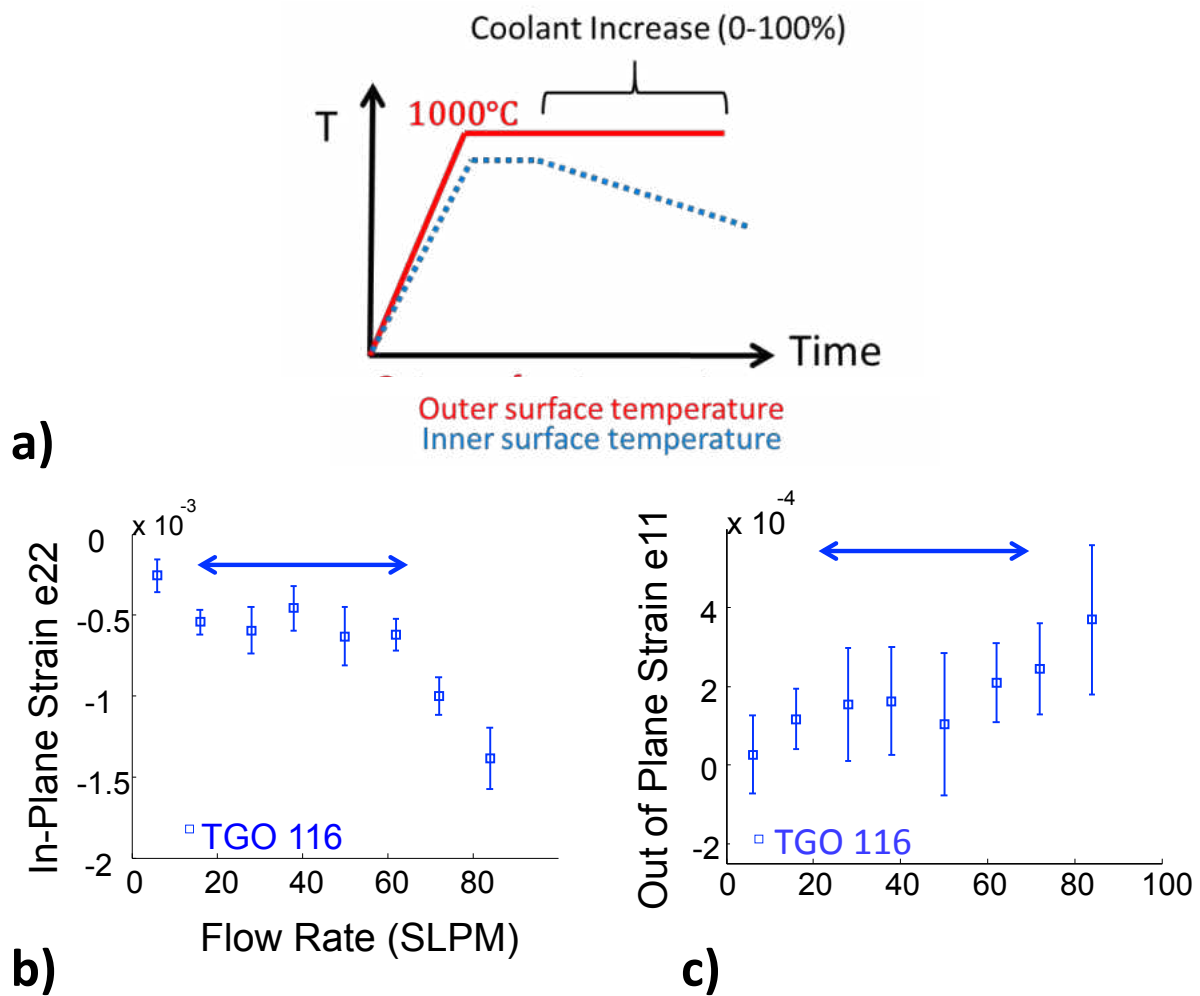


Figure 4.6: Isolating internal flow rate influence: a) Experimental design of flow rate study at 1000 °C high temperature hold and increasing internal coolant flow. Variation of (b) TGO  $e_{22}$  strains and (c)  $e_{11}$  strain.

With X-ray diffraction, there is an intrinsic sensitivity challenge for measuring extremely small strains. For synchrotron diffraction with 2D area detectors, the resolution limits are extremely precise with values in the range of  $10^{-4}$  being deciphered. How-

ever, it is necessary to note that the uncertainty increases approaching zero strain, but decreases with increasing strain. As such, values of certain response curves at high temperature in the range of  $10^{-5}$  microstrain are considered effectively zero. In Figure 4.4c and f there are distinct points with no error bars where the values of the strain are too close to zero to overcome the minimal noise in the system. As such the effects of high temperature hold non-linearity due to creep are limited when they remain that close to zero. For slightly large strain in the range of  $10^{-4}$  this is no longer an issue.

Below the zirconia top coat and oxide scale remains the EB-PVD bond coat which is a complex alloy comprised of NiCoCrAlY. Though various types of bond coats have been developed and are in application, this family of alloys is quite common. The alumina thermally grown oxide scale forms from the constituents in the bond coat, and can deplete a region of the bond coat of alumina. This creates variations in mechanical properties as well as chemistry that complicate our understanding of the system [119, 13].

### **4.3.2 YSZ Investigation**

Similarly to the TGO assessment, the YSZ  $e_{22}$  and  $e_{11}$  strain evolution was investigated for the mutli-variable assessment to elucidate the role and dominance of the mechanical loading, thermal evolution, and internal cooling variables applied to the YSZ. Of primary importance was the comparison of constant mechanical load with variable flow rate and

constant flow rate with variable mechanical loading. Comparing the resulting 9 individual full system tests, Figure 4.4 is produced.

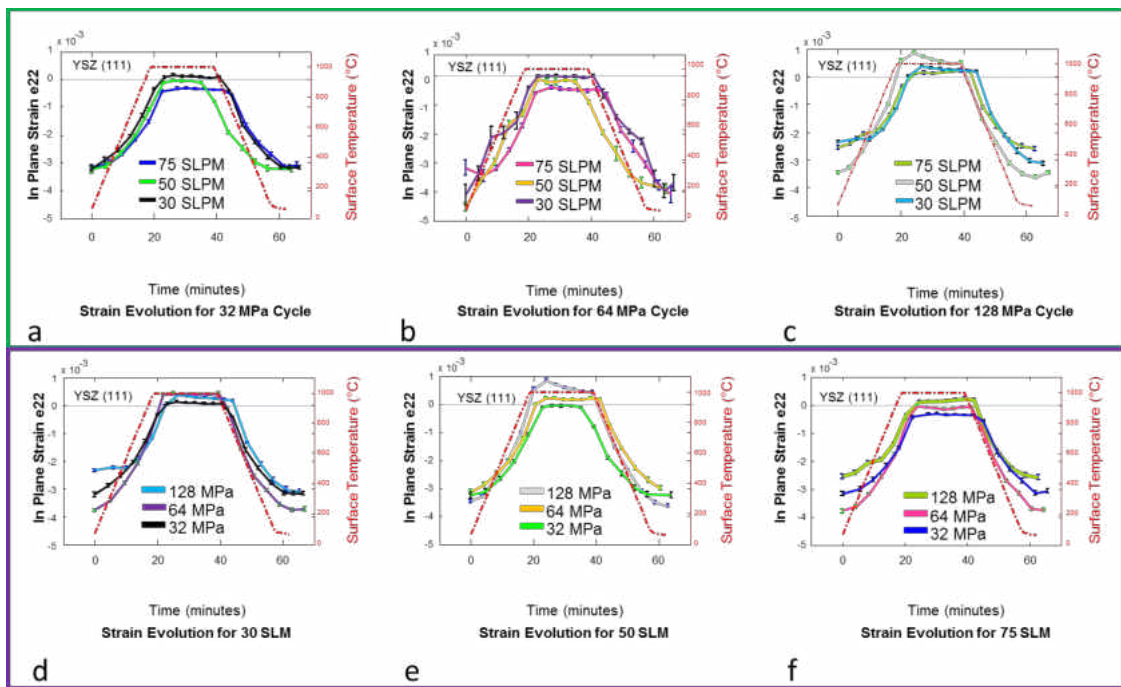


Figure 4.7: YSZ  $e_{22}$  strain response over thermal cycle for constant mechanical load with varying flow rate (a, b, c); and re-plotted for constant flow rate with varying mechanical loading (d, e, f).

The results show similar findings to  $e_{22}$  TGO findings in Figure 4.4. In Figure 4.7a, b, and c compare constant mechanical loadings of 32, 64, and 128 MPa with variations in



internal cooling of 30, 50, and 75 SLPM. The thermal cycle is constrained to the surface of the YSZ, and as such here at the TGO interface the temperature lags during ramp up and is more substantial as the internal cooling level is raised. Increasing mechanical tensile loading is seen to force the YSZ layer into the tensile regime at high temperature holds, where elevated tensile strains such seen in Figure 4.7c and e express more dramatic strain relaxation at high temperature, surmised to be the role of visco-elastic mechanics.

Reported additionally in Figure 4.8 is the full mutli-variable assessment of the YSZ for the out-of-plane  $e_{11}$  strains. As the columnar micro-structure of the YSZ behaves more anisotropic, the  $e_{11}$  findings are valuable to the simulation and modeling for lifetime prediction. The results demonstrate how the applied tensile loading can cause the  $e_{11}$  strains to turn to the compressive regime. This reversal of strain is detrimental to the durability of the coating. At the maximum compressive strains, time dependent strain relaxation is observed more prevalently as would be anticipated.

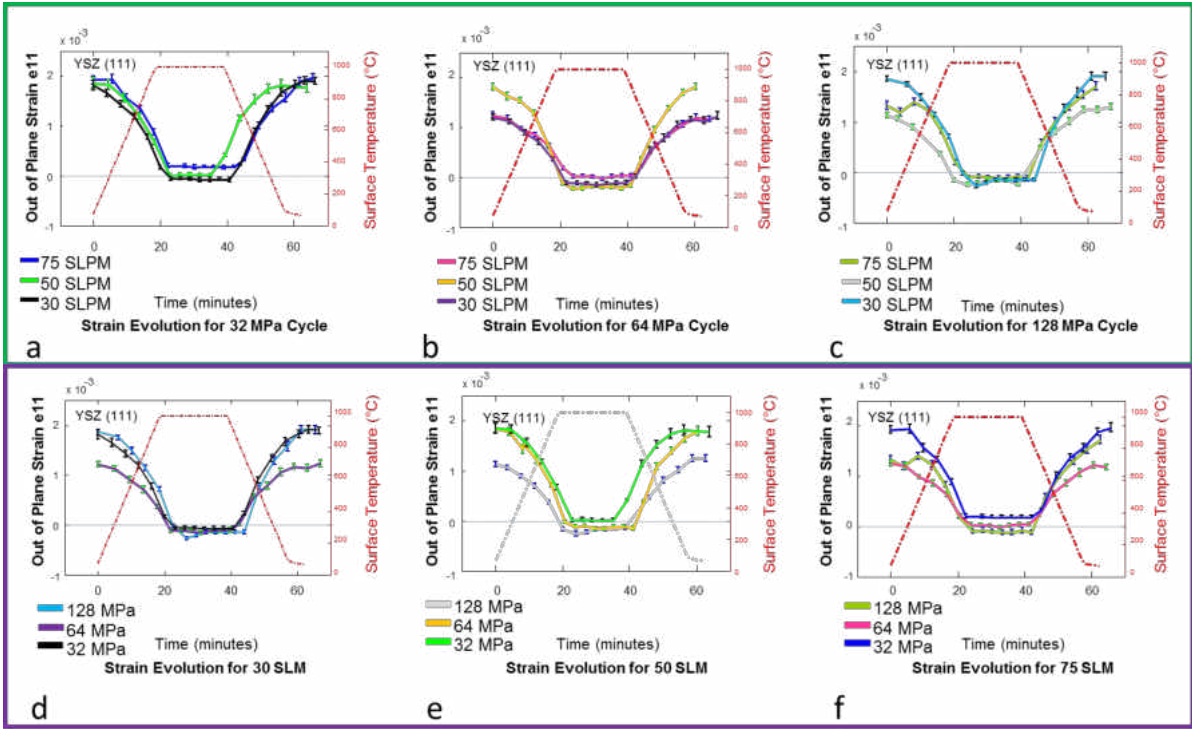


Figure 4.8: YSZ  $e_{11}$  (out of plane) strain response over thermal cycle for constant mechanical load with varying flow rate (a, b, c); and re-plotted for constant flow rate with varying mechanical loading (d, e, f).

Examining the effect of increasing internal cooling flow rate at high temperature hold for the YSZ, it was shown that the strain response is non-linear, which highlights that the variation between 30, 50, and 75 SLPM. This is featured in Figure 4.9. This entails not a purely linear increase in effect due to non-linear heat transfer and flow properties for the internal pipe flow. The trends follow a much more linear profile than observed in

the YSZ layer, although there is still a reduction in inferred cooling around 25 SLPM.

The remaining increase in flow rate volume is met with a near linear response.

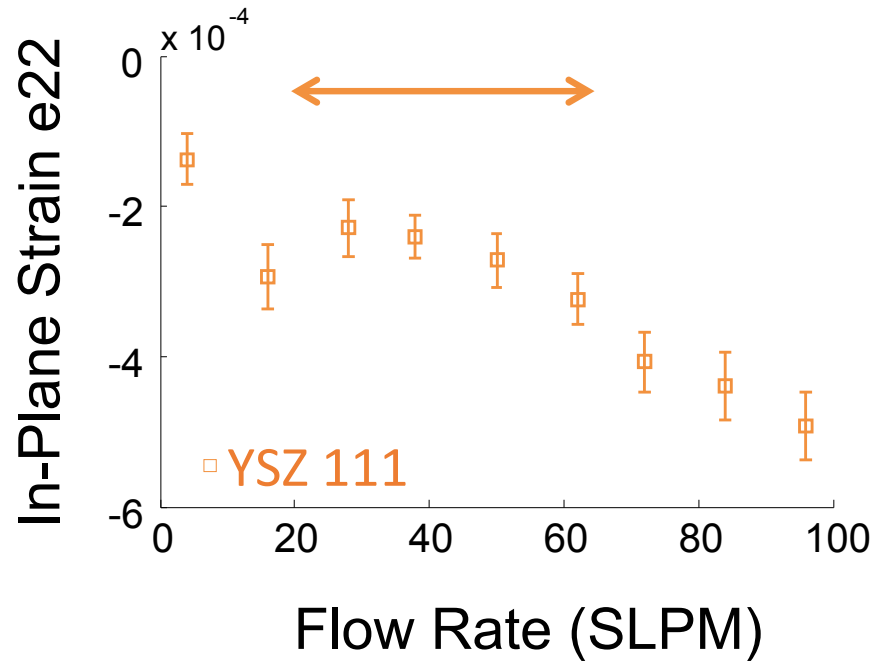


Figure 4.9: YSZ  $e_{22}$  (in plane) strain response over internal cooling flow rate increase during high temperature hold.

The extrema conditions were investigated for both the YSZ  $e_{22}$  and  $e_{11}$  strain profiles, as detailed in Figure 3.6, which tested mechanical loading-internal cooling at low-low, mid-mid, and high-high conditions over the applied external thermal loading temperature profile for the cycle. Figure 4.10a and b show the strain evolution for both in plane and out of plane ( $e_{22}$  and  $e_{11}$ ) for the tubular test specimens. This extrema testing provides the opportunity to compare the dominance of each variable against each other,

shedding light on the true mechanics of the layers. The YSZ  $e_{11}$  and  $e_{22}$  both demonstrate that the superposition of the mechanical loading and additional internal cooling have a converse influence on the strain profile. The resulting findings demonstrate that the high temperature strain profile may be tuned such that strain reversal can be avoided.

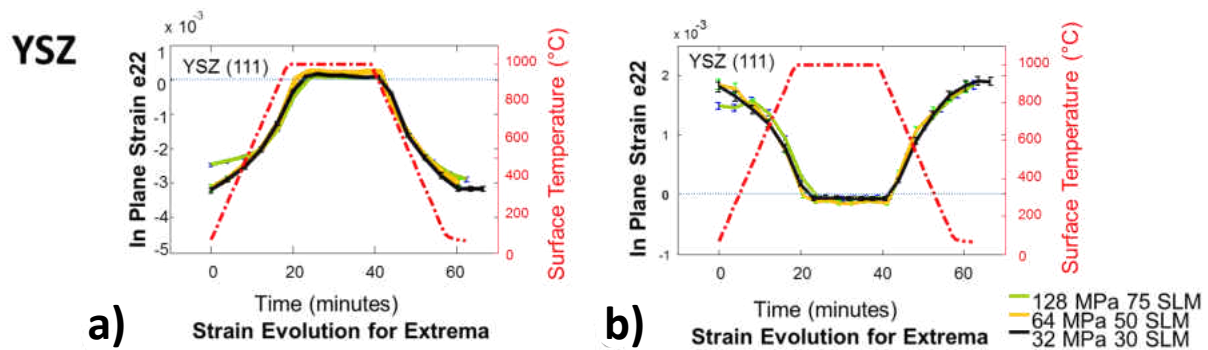


Figure 4.10: (a, b) Extrema testing strain evolution of low, medium, and high mechanical load and internal flow rate.

#### 4.4 Investigating Strain State Deviation Between Cycles

When investigating the YSZ strain profiles, it was observed that there was in fact some deviation of the residual strain state at ambient conditions as observed in Figure 4.7. This was unexpected, as plastic strain consideration should be low for ceramics at low temperatures [87]. To understand what the driving factors were behind this, additional analysis studies were developed and are presented herein with the hypothesized interpretation.

#### 4.4.1 Investigating the YSZ $e_{11}$ vs $e_{22}$ Ratio

Few studies have been conducted to investigate the influence of YSZ oxidation and sintering on the mechanical properties [27, 88]. Lughì et al [88] discusses the influence of surface undulations and how their existence influences the sintering and neck growth. Busso et al [27] has explored some of the simulation and experimental processes that revealed that initial feathery morphology smooths out before sintering and fusing through a process of external porosity consolidation. Featured in Figure 4.11 the  $e_{22}$  and  $e_{11}$  strain ratio is presented to demonstrate the high variation over the thermal ramp up. This deviation under the same applied mechanical loading, but with variations in internal flow rate, was not expected to exist at ambient condition. The figure highlights the variation over a small measurement window, where columnar pointing and surface roughness may be a factor, and where irreversible plastic strain evolution is inferred to exist.

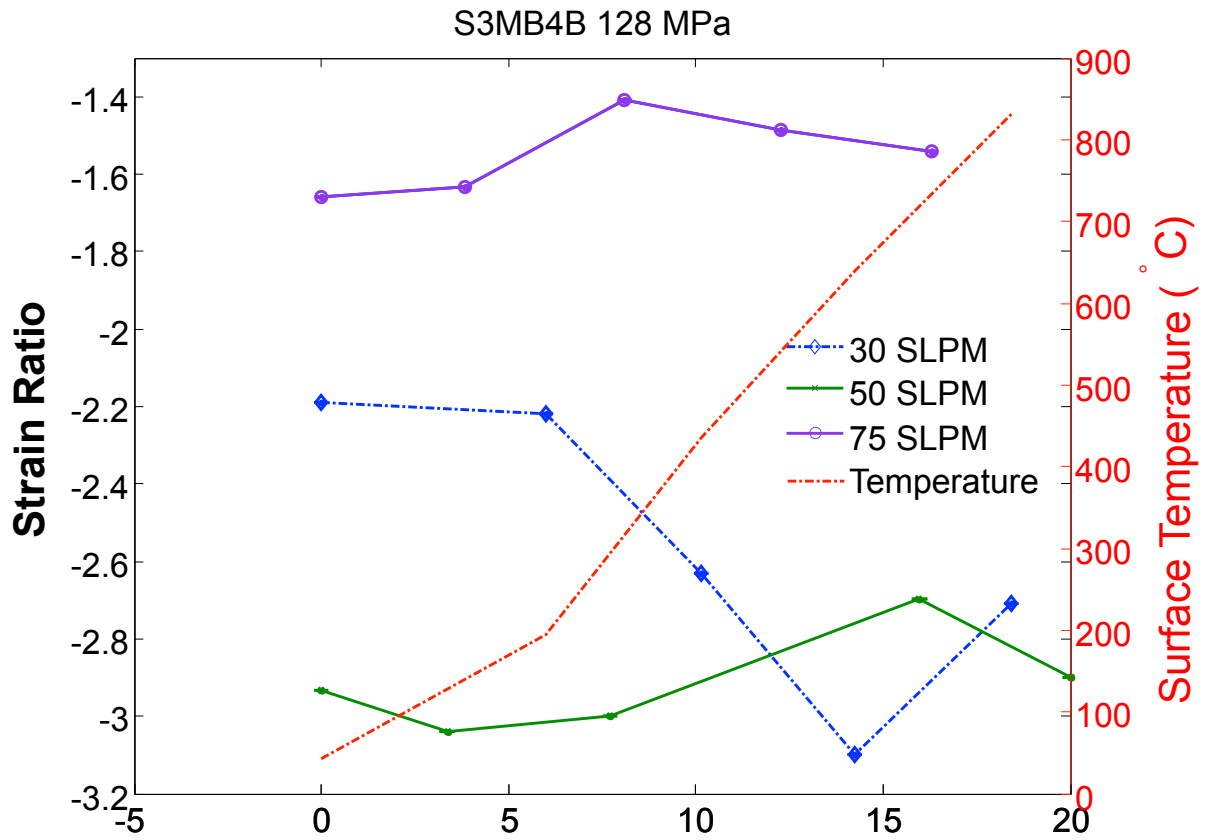


Figure 4.11:  $e_{22}/e_{11}$  strain ratio response over thermal ramping cycle for YSZ layer for constant mechanical load (128 MPa) with varying flow rate showcasing the change in residual strains as well as loading ratio.

#### 4.4.2 Observing Grain Rotation

After observing the variation in elastic strain ratio and residual strain variation, investigations into crystallographic plastic strain were conducted. While X-ray diffraction is

traditionally utilized for elastic strain measurements and phase identification, it can also shed light on grain size growth and crystallographic plastic strains [3, 67]. As each lattice plane has a particular intensity, re-crystallization and grain rotation can be identified through the evolution of texturing, or preferred orientation, identified in the diffraction Debye rings [93, 72]. Studies on lattice plane re-orientation, namely the evolution of different diffraction planes intensities increasing under the influence of loading, has been presented in literature [120, 136, 67].

It is known that texturing orientation will evolve under the influence of plastic deformation [93], and that grain sliding and dislocation processes are associated with deformation behavior [72]. Through analysis of this study, the 2D Debye rings azimuthal texturing orientation was identified. This is presented in Figure 4.12 and represents the (111) YSZ lattice plane.

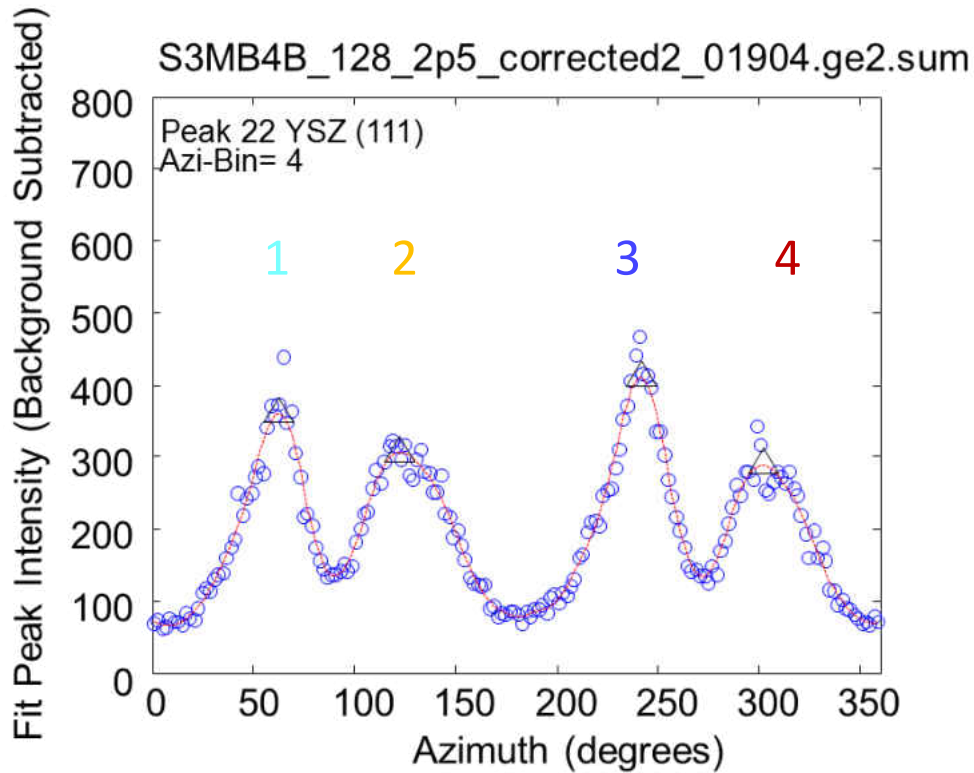


Figure 4.12: YSZ (111) plane azimuthal texturing and variation fitting, highlighting the four independent preferred orientations.

Taking the 2D Debye ring and fitting the intensity variations around the  $360^\circ$  azimuth, four distinct intensity peaks were identified, consistent with the tetragonal crystalline structure. As the ring is continuous, it can be understood that diffraction particle statistics are sufficient. The fitting of the azimuthal quartet was normalized by the full intensity area to minimize any variations due to depth, which may vary 50 microns with



thermal expansion. The fitting of the normalized quartet was conducted for the 128 MPa cycles with variable flow rate at 50 SLPM. The quartet was fit over the thermal cycle with constant mechanical loading and is presented in Figure 4.13.

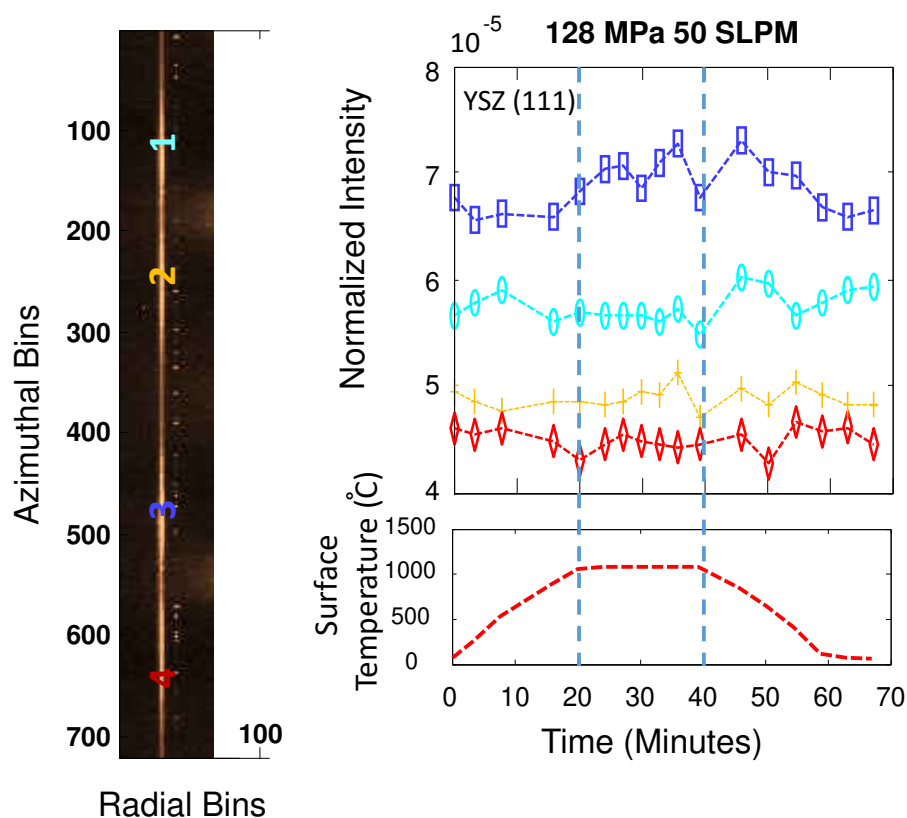


Figure 4.13: YSZ (111) plane azimuthal texturing and variation through cycle: a) transformed Debye ring with azimuthal texturing fitted peaks called out, b) through cycle intensity peak deviation for each azimuthal intensity peak.

Here the evolution of the azimuthal texturing through the thermal cycle is compared across the thermal cycle. During the ramp up phase the blue (peak 3), orange (peak 2), and red (peak 4) show the shifting negative from the initial orientation. Conversely cyan (peak 1) seems to grow under the thermal ramp before declining at high temperature. At high temperatures, sudden grain rotation initially takes place. This suggests a correlation with the variations in Figure 4.7, and the grain rotation through the high temperature hold is indicative of the strain release. The blue (peak 3) is seen to grow at high temperature, but with a rise, fall, and rise profile. This may also be mirrored in orange (peak 2). The results are similar during cool down as the ramp up period, however the process is not completely reversible.

While the results seem to be promising, it was not possible to delineate trends across all of the flow rates within the sensitivity on the measurements. This may be due to the intensities not being maximized, the complexity of fitting the textured ring intensity, and the normalization process to compare each measurement point to the rest of the cycle. The process results in very low normalized intensities where it is challenging to conclusively establish the cause of the variation.

This will lead to the development of additional experiments to maximize the signal to noise ratio of the measurements, and may provide the opportunity to conclusively identify the plastic lattice strain component of the high temperature mechanics which results in strain relaxation and visco-elasticity. The method has the potential to be applied to a number of different high temperature materials, including metallics, and will be refined

as a future work. If successful it would lead to an extension of the capacity of the synchrotron strain measurements to investigate the grain mechanics. In tandem with high temperature digital image correlation and 2D lattice strain measurements, this may push the envelope in defining high temperature mechanics for aerospace materials.

#### 4.4.3 Creep Investigations

Of interest to the investigation was the creep response for the oxide and YSZ layers at high temperature under an immediately applied mechanical load of sufficient magnitude to incite a relatively quick creep response. From the designed experiment, the resulting strains were captured for both layers at high temperature hold. To have the results be applicable for analytical simulation models which include the Norton-Bailey Creep Law [99, 99, 7, 20, 96, 117, 6], the strain response was investigated. The Norton-Bailey Creep Law has long been used to provide a model for the visco-elastic response in engineering materials and is applicable for quantifying mechanical behavior in multi-layer ceramics and ceramic matrix composites. X-ray diffraction is traditionally utilized to capture elastic strains via changes in lattice plane spacing, however it can be inferred, with sufficient experiment design, from the decline in elastic strain.

The equation is presented below in Equation 4.1.

$$\dot{\epsilon} = A \cdot \sigma^n \cdot e^{-Q/R \cdot T} \quad (4.1)$$

Here  $\dot{\epsilon}$  is defined as the strain rate response, while  $A$  and  $n$  are temperature dependent constants. In this study while lattice strains were obtained using the diffraction measurements, global displacements were not obtained. For future experiments, the addition of high temperature extensometers and digital image correlation to aid in the global measurements will be implemented. As such the resulting measurements are presented in crystallographic strain and strain rate, which is applicable for supporting numerical simulation. It is often difficult to assess whether the creep is resulting from grain sliding primarily or diffusional creep at these loading conditions [102, 107, 37, 32], although an effort here is made to lend interpretation. Presented in Figure 4.14 is the in and out of plane strain response and Power Law Fit coefficients. From the fitting, which demonstrated exceptionally high goodness of fit, the strain rate for both  $e_{22}$  and  $e_{11}$  directions was generated.

Power Fit Coefficients (with 95% confidence bounds):

$$y = ax^b + c$$

$a = 5.563 \cdot 10^{-4}$  [4.831, 6.295]  $\cdot 10^{-4}$   
 $b = -0.3717$  [-0.442, -0.3015]  
 $c = -4.656 \cdot 10^{-5}$  [-12.16, 2.845]  $\cdot 10^{-5}$

$a = 9.455 \cdot 10^{-5}$  [3.526, 15.38]  $\cdot 10^{-5}$   
 $b = 0.4617$  [0.2718, 0.6516]  
 $c = -0.0003761$  [-4.397, -3.125]  $\cdot 10^{-4}$

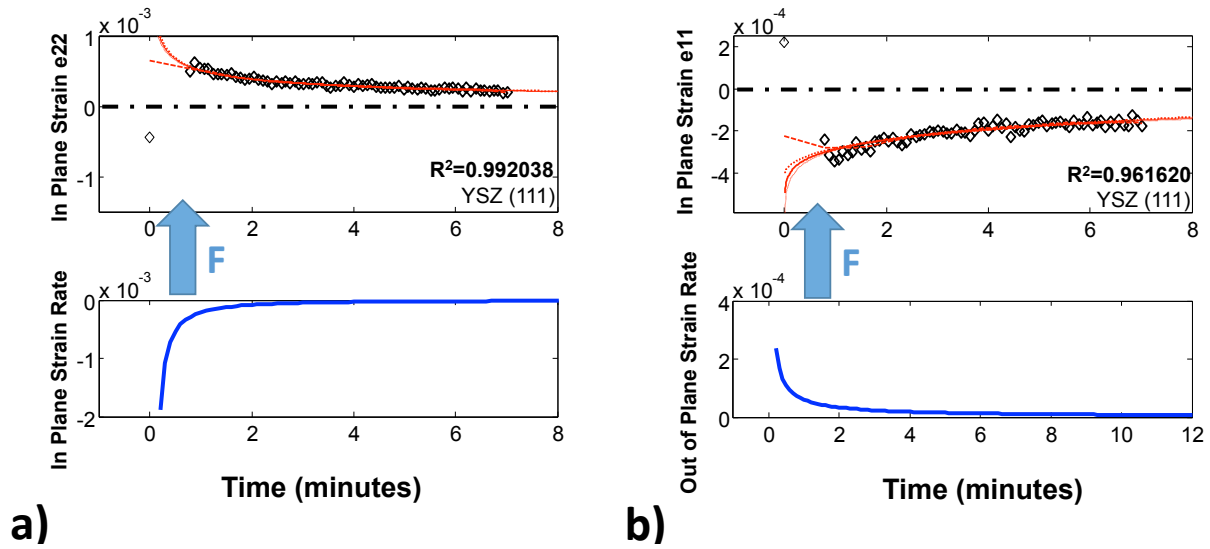


Figure 4.14: Creep response and fitting for YSZ (111): a)  $e_{22}$  strain response and Power Fit (top) with corresponding strain rate, and b)  $e_{11}$  strain response and Power Fit (top) with corresponding strain rate.

Of particular interest to modeling and assessing the influence of creep on the YSZ is the ratio of the in-plane and out-of-plane creep strain rate response. The finding is presented here in Figure 4.15 and helps to link the coupled creep response due to the aged columnar structure of the YSZ. This is particularly important for thrust generating

engines, traditionally with coatings deposited via EB-PVD producing feathery columnar structures that through the aging process sinter and evolve.

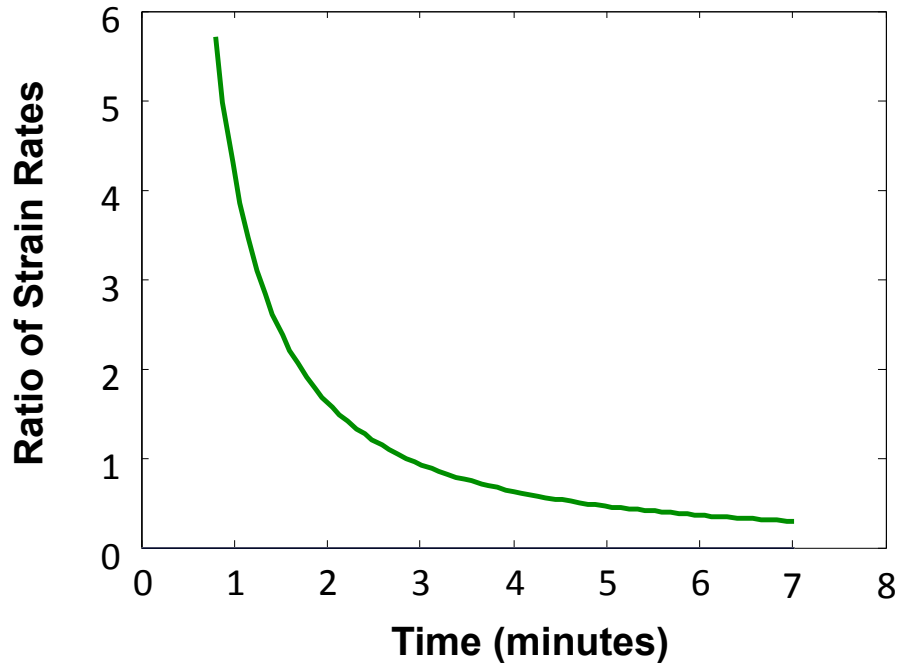


Figure 4.15: Strain relaxation rate under induced creep loading for YSZ (111): ratio of  $e_{22}/e_{11}$  strain response numerical fitting.

As noted before, it is of great difficulty to determine the primary influencer on why the creep response is produced. In an effort to interpret the influence of the high temperature mechanics, investigations in the variation in preferred orientation were conducted as highlighted in Figure 4.12. These four azimuthally oriented peaks in the (111) plane were fit and subsequently normalized by the area under the entire azimuthal curve. The findings are presented in Figure 4.16.

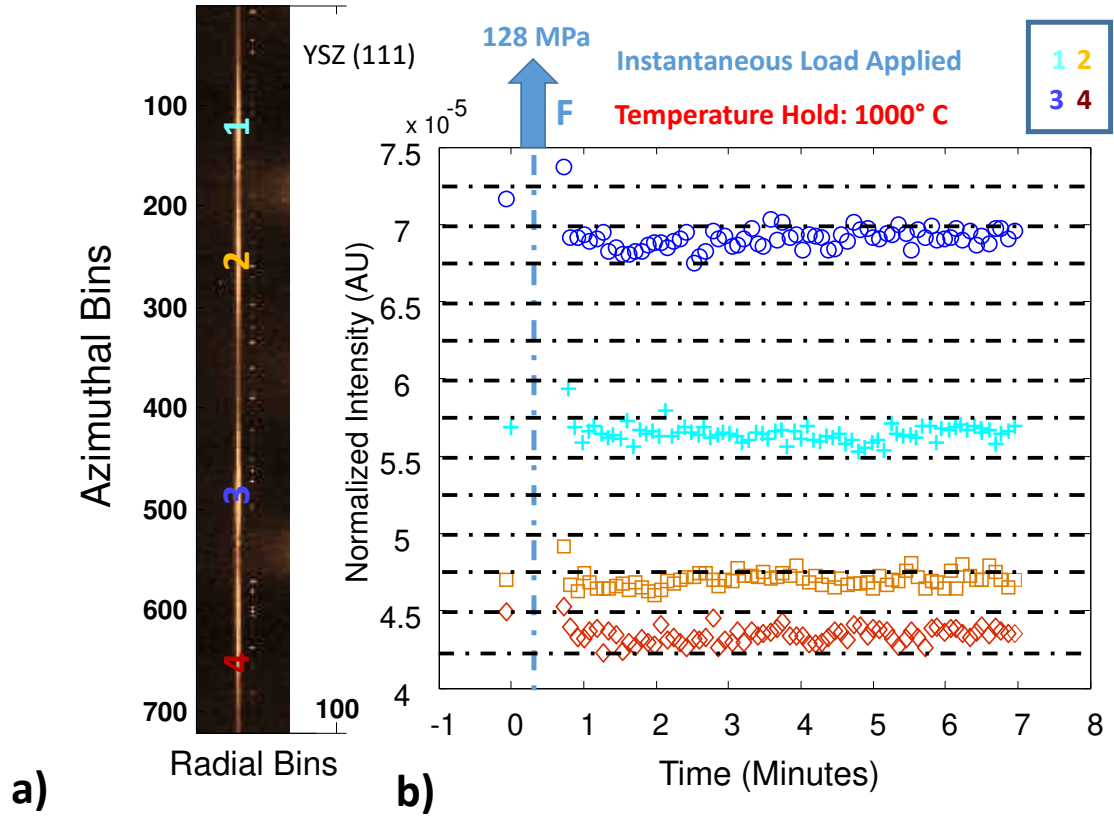


Figure 4.16: Grain rotation response for YSZ (111) under creep loading: a) transformed Debye ring with azimuthal texturing fitted peaks called out, and b) preferred texturing peaks evolution under creep loading and time.

The variation in azimuthally resolved peak intensity suggests that the grains may be re-orienting in response to the applied mechanical load during high temperature. At this time the interpretation of the trends has not yielded the confidence with respect to the influence of instrumentation uncertainty compounded by the analysis procedure. How-

ever, grain rotation at high temperature may be one of the driving mechanisms for strain relaxation and un-linear high temperature mechanics. Material scientist investigating metallic and nano-structured materials [93, 72] have used similar techniques to explore grain alignment. Margulies et al [93] investigated how preferred orientation sheds light for pure aluminum specimens on how grains reshape and evolve under loading, and how crystallographic orientations must rotate with respect to each other due to coupling at the grain boundaries; while, Ke et al [72] investigated nano-structured materials mechanics including how deformation behavior was influenced by grain boundary sliding, dislocations, and viscoelastic creep mechanics. From the literature is clear that the results in the study suggest similar phenomena, namely that grain re-orientation and particularly the rotation of the grains throughout the thermal cycle contributed in large part to the strain relaxation.

Highlighted in the results in Figure 4.16, it can be seen that after the initial instantaneous loading at 1000 °C there is a brief spike in preferred orientation at every azimuthal peak. Following the response, a decrease in orientation is immediately identified, and for the peaks 1 and 4 the intensity falls considerably below the initial value pre-loading. However, as time at temperature persists, the intensities for peaks 3 and 4 more noticeably increase than that of their counterparts. It can be inferred that through the loading hold, that grains are re-orienting in line with peak 3 and 4 which results in a reduction in strain. Notably, the trend seems to slow as time continues which reflects and correlates to the settling of the strain rate.



## 4.5 Discussion of Trends and Design for Durability

1. Increased internal cooling flow rate, at high temperature holds and constant mechanical load, is shown to move the  $e_{22}$  for both YSZ and TGO strain towards increased compressive strains. This is clearly seen in Figure 4.4a, b and c. The application of mechanical tensile load opposes the effect of internal flow cooling on the TGO and YSZ strain. Further, although the role of increased internal flow rate from low to high flow rates is distinct, midrange flow rate (50 SLPM) show decreased confidence and sensitivity.

2. Increased mechanical loading, at constant flow rate and constant external temperature, will push the oxide scale  $e_{22}$  strain into tension. This is of specific interest at high temperature holds, where sufficient axial loading can take the oxide scale from compression or near zero strain and pull it into tension. This is seen in Figure 4.4c and further visible in Figure 4.4d, e, f. In previous work [62] it has been shown that further tensile stresses may form due to creep relaxation over cyclical loading. However, when coupled with internal cooling, the variables compete and the resulting superposition is reflected. This is evident in the progression in Figure 4.4d, e, f. This holds true as well for the YSZ  $e_{22}$  strains, as seen in Figure 4.7. For the YSZ  $e_{11}$  strain evolution, the converse is true where increased mechanical loading at constant flow rate and constant external temperature draws the out of plane strains into the compressive regime from its residual compressive state.

3. Response on high temperature hold depends on the strain level resulting from the combined applied mechanical load and internal cooling rate. For the TGO reaching more prevalent tensile strain, significant strain relaxation is observed in the  $e_{22}$  strain profile, which can be seen clearly in Figure 4.4c and in Figure 4.7c. When the strain during hold is compressive, slight increase of compressive strain occurs, as displayed in Figure 4.4 a and f. These observations can be explained by considering the two competing mechanisms of creep relaxation and accumulation of growth strain as investigated via numerical analyses in literature [62]. At high temperature it is assumed that TGO growth results in thickening of the TGO and may increase the state of compressive strain at the ambient [70].

While the growth strain is always increasing the compressive strain creep relaxation is driving the strain always towards zero. Thus, at high tensile strain level creep relaxation and growth strain are acting both to reduce the strain. In contrast, at high compressive strain level, creep relaxation and growth strain are counteracting. Depending on creep parameters, growth rate, and yield strength of the TGO an equilibrium strain or stress will be reached after certain hold time. At strain levels close to zero the sensitivity of synchrotron strain measurements is decreased due to superposed signal noise.

4. Attributed to mechanical loading, visible in Figure 4.4 and Figure 4.7, the increased applied tensile loading affects the rate at which the oxide scale and YSZ top coat reaches the zero strain condition (or passes the zero line). Effectively, the applied stress changes the slope (and shifts to the left), of the strain evolution. Additionally, the increase in

internal coolant flow rate as seen in Figure 4.4 has the effect of causing the oxide scale temperature to lag increasingly with respect to the top coat surface temperature. This results in the curves shifting to the right as the TGO and YSZ take longer to achieve its high temperature, and can be seen in Figure 4.4a, b, c. Mechanical loading and increased internal cooling both stretch the curves in both ramp up and ramp down condition. Conversely during ramp down, increased flow rate begins to dominate and drives the strain response back to the compressive state at an increased rate; this acts against the applied tensile stress, which works to slow the response's return to compression.

5. Herein it is discussed that the superposition of mechanical loading and internal cooling has an influence to cause a lag in strain response to decreasing external temperature. In Figure 4.10 and Figure 4.5, the results for the experiment which tested mechanical loading-internal cooling at low-low, mid-mid, and high-high conditions over the applied external thermal loading temperature profile for the cycle are plotted. It was further shown that higher mechanical loading and internal cooling have a opposing influence on the TGO and YSZ strain. This is presented visually in Figure 4.17. This superposition suggests that the variables may be tuned to offset each other, as their magnitudes of influence are similar but of opposite direction. This is of great interest as the equivalent mechanical loading and thermal profile across the axial length of the blade vary. The findings suggest that the inclusion of variable flow rate cooling channels may be able to offset the tensile strain spikes for the  $e_{22}$  strain profile during the most

critical loading times, namely take-off and climbing for thrust powered engines, and by doing so minimize or halt any strain direction reversals that may lead to damage.

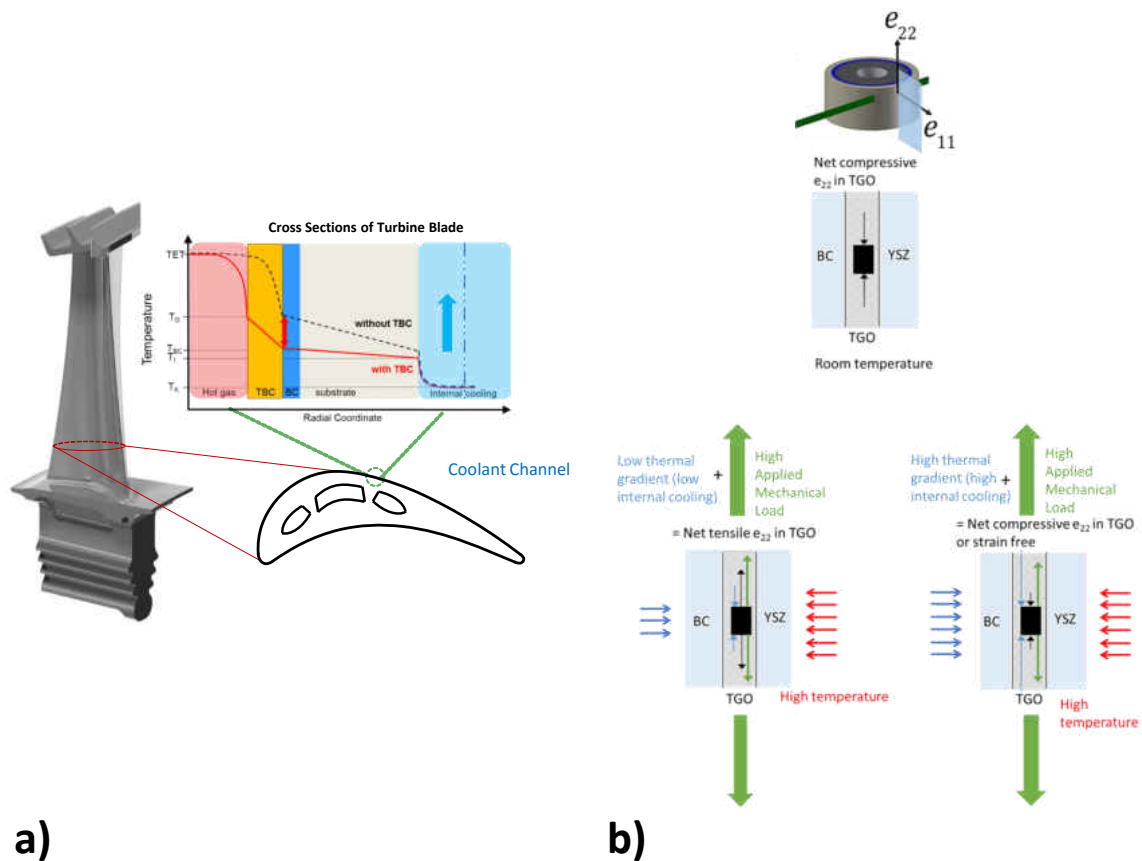


Figure 4.17: Influence of loading conditions: a) Schematic of turbine loading and implementation of internal cooling b) visual schematic to emphasize how the influence of loading variables enables the tuning of the resulting superposition that alters strain evolution.

The breakthrough of establishing the competing influences of applied loads and thermal gradients on the internal strains lies in identifying critical cycle scenarios that can

lead to tensile strains within the TGO which have a negative on impact durability. This work offers the capacity to use the measurement results to establish design strategies for internal cooling that would prevent the generation of tensile strains within the TGO, potentially avoiding damage mechanisms and extending the durability and life duration of the coating system.

## 4.6 Conclusions

In this study, in-situ X-ray diffraction data of tubular coated and aged specimens were collected under multi-variable loading conditions capturing their influence on the strain of thermally grown oxide layers in a TBC system. Of significance is the finding that increased applied tensile mechanical loading can result in subtle tensile strains at high temperature for the oxide scale. This is remarkable as the TGO develops extremely high internal residual compressive stresses due to thermal expansion mismatch and its growth. This factor competes against the induced thermal gradient, where the internal coolant influence pushes the conditions towards compression. Quantifying such variation over the turbine blade will provide a path to improving the lifetime assessment of TBC systems significantly and enable design strategies for durability enhancement. The bond coat has been shown to have a large influence on the diffraction patterns of the oxide scale. Only one viable oxide peak was available for strain analysis, and during high temperature transmission was interfered with by bond coat precipitation. The development of addi-

tional fitting methods including a predictive Fourier fitting with adjustable constraints allowed for precise strain analysis. This work offers the capacity to use the measurement results to establish design strategies for internal cooling that would prevent the generation of tensile strains within the TGO for jet engine blade coatings, potentially designing to avoid damage mechanisms and extending durability.

Investigations into the high temperature mechanics for the YSZ layer resulted in quantification of the azimuthal texture for the (111) plane's ring in an effort to identify potential causes for the non-linear behavior. Through cycle measurements were evaluated and plotted to compare the four primary textural peaks and revealed subtle trends that may link high temperature strain relaxation to the grain mechanics of lattice rotation. At this time the trends cannot be conclusively distinguished from sources of uncertainty, and raising the confidence in the measurement sensitivity will be a focus of the forward work. The technique is anticipated to be applied to high temperature metallic specimens to investigate the lattice strain state more completely and to compare the response with global strain measurements such as digital image correlation or high temperature extensometers. This may afford the opportunity to correlate and define the cause of complex high temperature mechanics for multi-layer composites and metallics.

## **CHAPTER 5**

### **MECHANICS OF CERAMIC MATRIX COMPOSITES**

Ceramic matrix composites (CMC) have shown great promise due to their thermal stability, coupled with low density and quasi-ductility due to mechanisms such as crack deflection and fiber pull out [31, 30]. Their high temperature deformation mechanics are still a subject of research, particularly how the composite transfers loading. In an effort to extend this knowledge, simulation studies to refine the deformation response envelope for isochoric and compressible have been explored matrix [89]. Results were shown for how the variation in material properties will influence the fiber rotation in the system; in an effort to explore the material's experimental response, a series of synchrotron studies were designed to illuminate the composite mechanics. Due to the high variation in processing micro/meso-structure, and the difficulty estimating the composites' properties for simulation, investigations to decipher the composite mechanics have been proposed to more clearly capture experimentally the mechanics to validate and enhance simulation studies.

#### **5.1 Objectives**

The goals of the investigation were rooted in the hypothesis that the all alumina oxide could be distinguished in terms of fiber and matrix via synchrotron studies for analysis based on the composite's grain size, porosity, and discrepancies in load partitioning and

elastic modulus. If successful this could enable the individual constituents' mechanics to be more fully understood. Using quantitative imaging and synchrotron diffraction measurements, the investigation was designed to meet the following:

1. *Objective 1:* Compare micro-structure of WHIPOX<sup>TM</sup> variations and investigate how defects arise from processing and in application loading.
2. *Objective 2:* Isolate the mechanics and load partitioning of the fiber and matrix by developing methods for examining anisotropy and texturing.
3. *Objective 3:* Comparison of diffraction strains for varying orientations and compositions of WHIPOX<sup>TM</sup> substrate to shed light on the mechanics of the system.

## 5.2 Non-destructive Isolation of Fibers and Matrix

Synchrotron studies were designed to evaluate and characterize all oxide ceramic matrix composites. WHIPOX<sup>TM</sup> composites utilize Nextel<sup>TM</sup> fibers ranging from pure  $\alpha$  alumina (610) or alumino silicate (720). The grain size inside the approximately 11 micron fiber diameters is estimated between 50 and 75 nanometers, which produces high elastic modulus capable ceramic fibers [1] reaching between 260 and 380 GPa. The matrix material is generally produced through ball milling with particulate sizes between 0.1 and 1 micron [105] and results in approximately a 70% matrix porosity. This yields highly ductile behavior due to matrix compaction and cracking. The mechanics of the compos-



ite are challenging to model, and the aging process results in matrix densification and a change in applicable mechanics. Due to the dissimilar grain size and the elastic modulus varying by at least a factor of 5 [56, 6] between the matrix and fiber, the hypothesis formed that through synchrotron studies the individual constituent mechanics could be elucidated.

X-ray diffraction measurements were conducted at ambient and nominal applied loading conditions, and the initial scans were utilized for phase and plane identification as well as examination of any texturing. The identification is presented in Figure 5.1. In Figure 5.1a the raw Debye rings are examined for initial texturing. The rings showcase good particle statistics and minimal texturing. Two partial obstructions are visible on the 2D area detector that interfered with some of the outer rings, however the effect is minor when performing strain analysis due to the azimuthal binning of the ring. This was corrected in the continuing experiments and has been presented in [89]. In Figure 5.1b the phase identification shows only  $\alpha$ -alumina planes including (300), (116), (024), (110), (113), and (104). Additional trace amounts of zirconia, which is a contaminant during the matrix powder manufacturing, are identified. A visualization of different crystallographic planes used in analysis is presented in Figure 5.1c, with the (110) and (113) planes for  $\alpha$ -alumina highlighted.

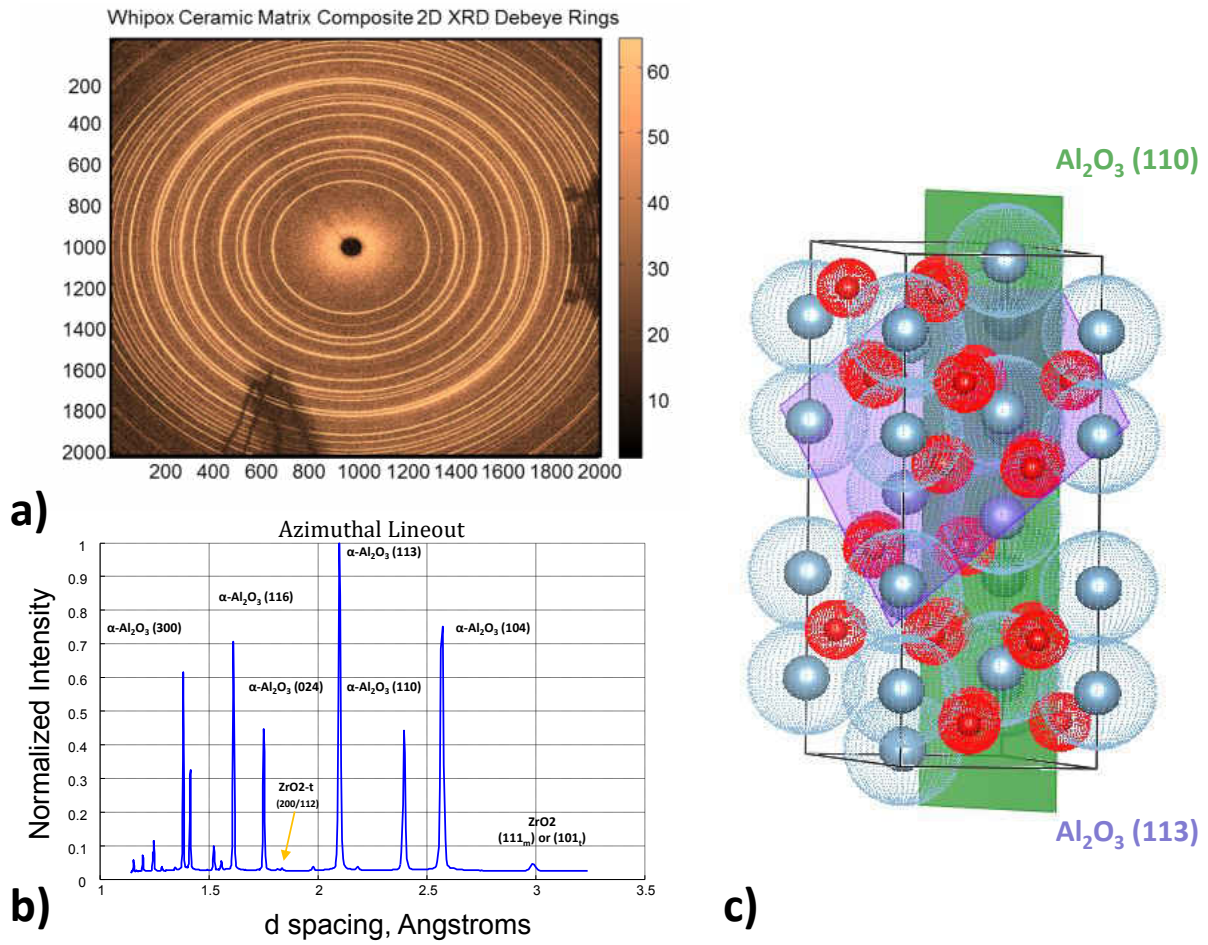


Figure 5.1: Synchrotron X-ray diffraction assessment for all alumina WHIPOX™ composites: a) 2D Debye rings for composite, b) peak identification of ring set, and c) representation of crystallographic planes for  $\alpha$ -alumina crystals [89].

Strain analysis was conducted on the diffraction rings for the all alumina composite at the extreme environment with high temperatures of 1200 °C applied and the addition of compressive mechanical loading of applied 40 MPa. This is shown in Figure 5.2. From the diffraction rings the lattice plane strains  $e_{11}$  and  $e_{22}$  were determined for six planes

of interest. Additionally in Figure 5.2, the calculated elastic constants associated with the respective planes are presented for comparison, which have been calculated in the DECalc software with single crystal data from Gladden et al [49, 92].

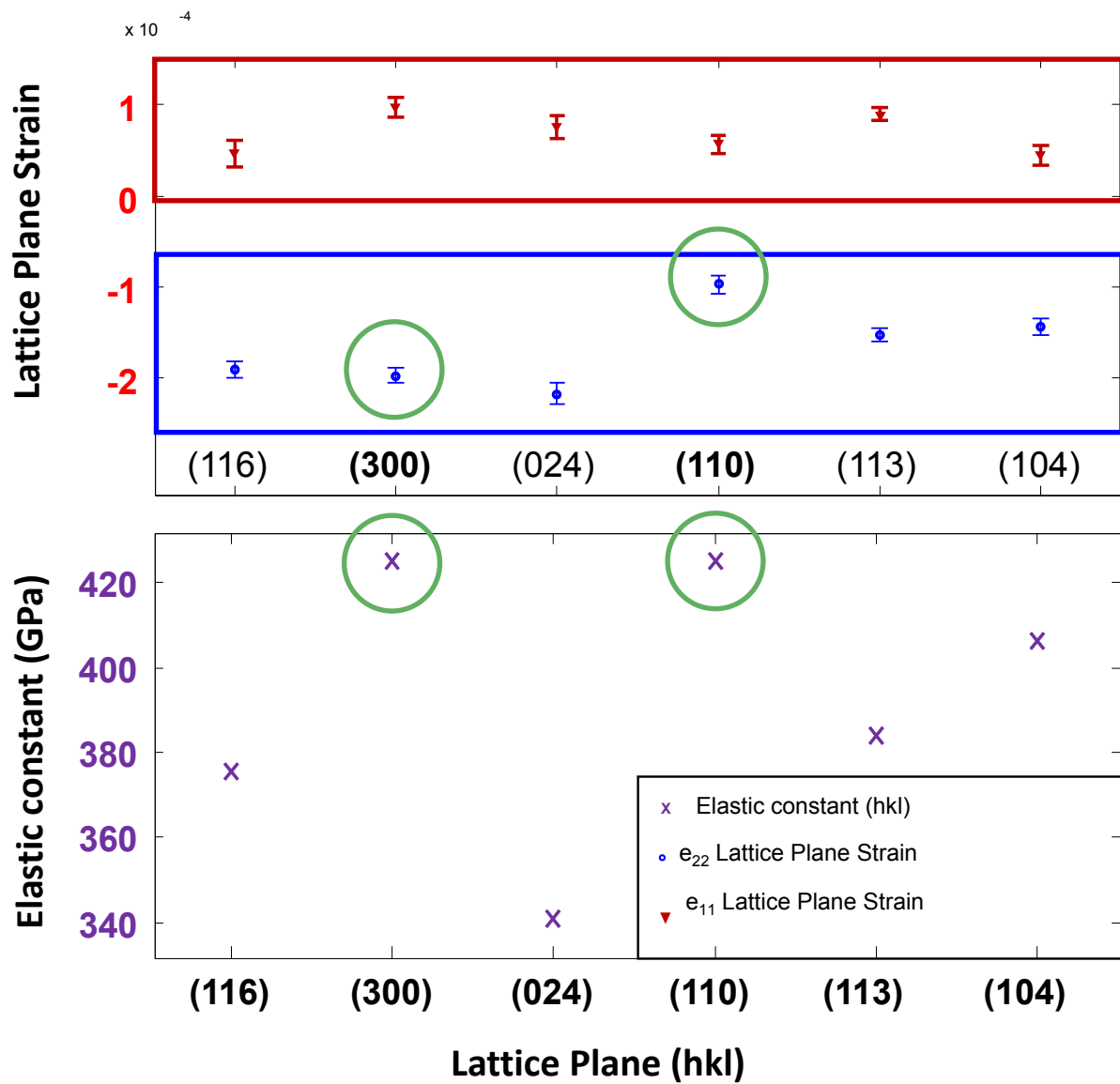


Figure 5.2: High temperature mechanics under constant loading producing strain response for six crystallographic planes. Lattice plane strains were plotted for  $e_{11}$  and  $e_{22}$ , and compared directly to their calculated (hkl) dependent elastic modulus.

The (110) plane shows significant difference from the (300) plane in strain. Interestingly, the lattice plane strain data for the (300) and the (110) planes differ, even though their respective calculated elastic constants are equivalent. This was reported in [89] and demonstrated that high degrees of anisotropy exist including under high temperatures and mechanical loading. This encouraged the outlook that perhaps either the fibers or matrix would express dominance in a certain crystallographic plane based on preferred orientation and grain growth.

### 5.2.1 Tomographic Isolation

Imaging presented herein was conducted at room temperature, although techniques for capturing measurements at elevated temperatures have been developed in the course of this work for future experiments. Tomographic imaging was conducted over  $180^\circ$  of rotation, and data reconstruction. Following reconstruction, analysis was conducted in a combination of Avizo Fire<sup>TM</sup>, ParaView<sup>TM</sup>, and ImageJ<sup>TM</sup>. Segmentation was conducted for isolating a region of interest. Subsequently effort was made to bypass filter the fibers and matrix respectively. The challenge here is that the materials, being identical in chemical formula, have near identical attenuation coefficients. In Figure 5.3 the isolated constituents are presented side by side after thresholding and filtering.

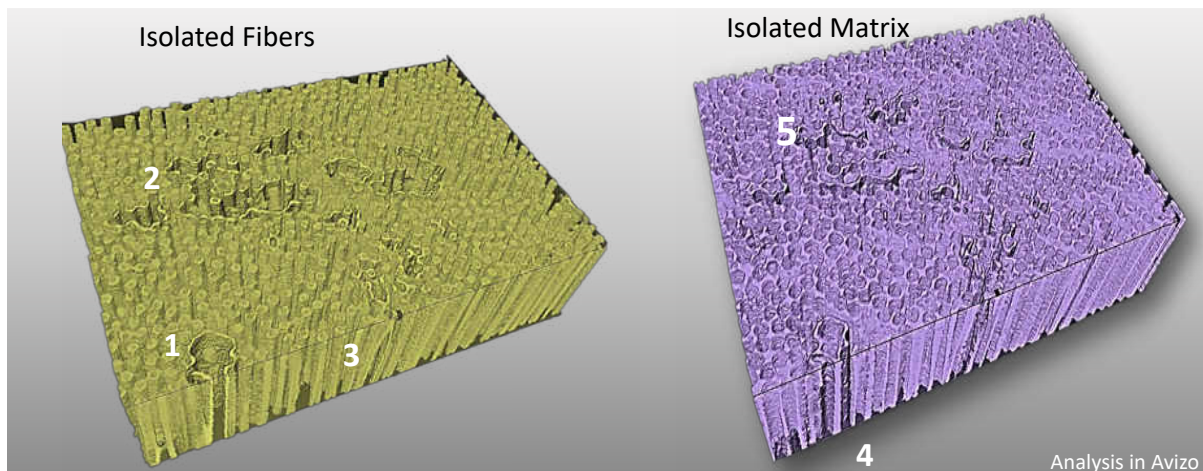
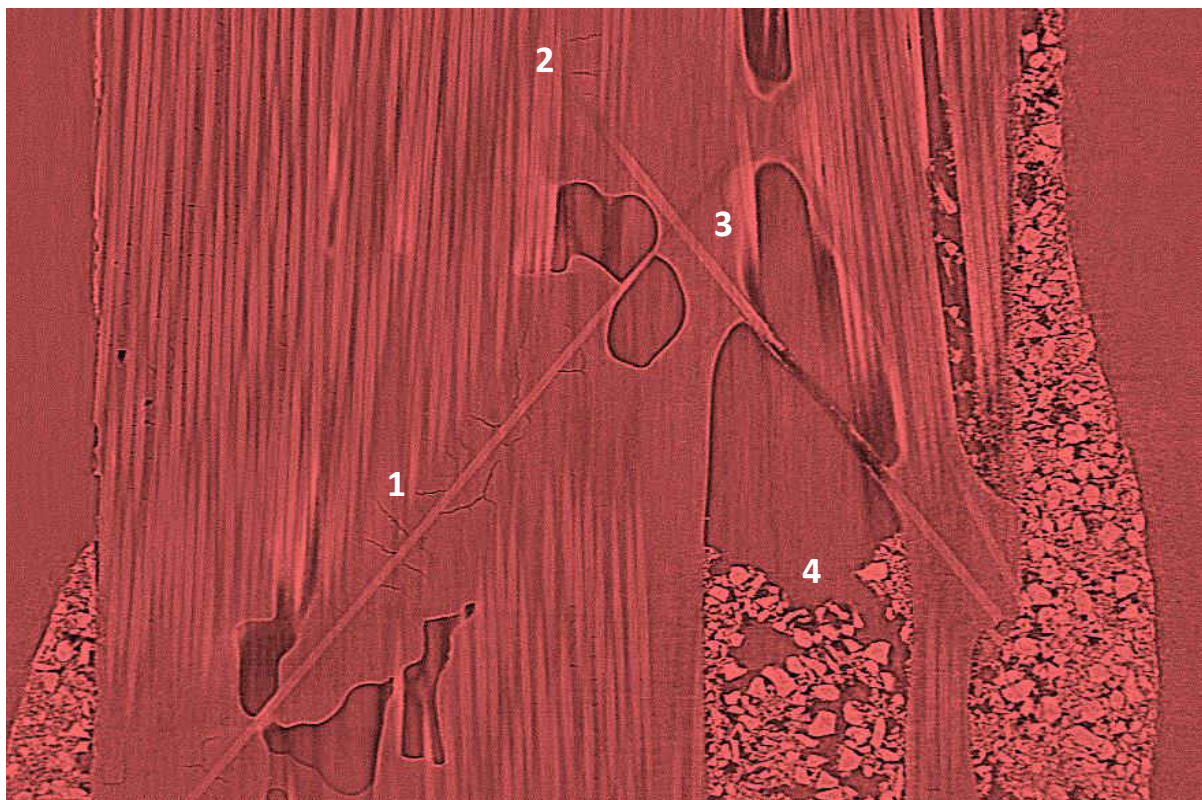


Figure 5.3: Isolated fiber and matrix segmentation showcasing zones of interest. Image produced in Avizo Fire™.

This visual assessment provided interesting perspectives of the fiber forest, including identifying the variation of columnar angles and zones where broken fibers create a matrix dense region. Isolation of the matrix showed the non-uniform interface between the fiber and matrix resulting during the infiltration of the fibers and bundles with the slurry. At point 1) it can be seen a large vesicle column devoid of fiber. These large pockets of air or raw matrix appear throughout the system. In point 2) it can be seen the large scale porosity, where broken or missing fibers give way to infiltrated matrix rich zones. At point 3) fiber rotation can be observed and further analysis as such will allow for quantifying the fiber rotation angles. Point 4) shows texture of the matrix to fiber interface, suggesting that it may be possible to identify the interactions between the sponge like matrix and fiber reinforcement. Finally in point 5) it is observed that inside

the matrix rich zones there exists some extensive void chains while other areas are filled with matrix slurry.

For further examinations, a vertical 2D interior slice of the all alumina specimen was constructed is presented in Figure 5.4 with four specific zones of interest marked.



**All alumina specimen, ambient temperature**

Figure 5.4: Vertical slice of all oxide composite showing processing defects. Image produced in ImageJ™.

The first zone of interest is marked in Figure 5.4 showcases a broken fiber that has misaligned and disturbed the micro-structure. The high angle deviation produces crack-

ing in the orthogonal direction. In zone 2 it is identified small horizontal drying cracks that form due to processing. Zone 3 observes a secondary broken fiber that has realigned deviating from the principle direction. It is postulated that the broken fibers during manufacturing give way to large voids that are infiltrated by pure matrix, which has a lasting influence on the composite mechanics throughout its lifetime. This defect forms a bubble of matrix rich slurry internally, deviating the local damage mechanics and aging behavior. The edge of these matrix rich voids may include zones with a thick rind of more compactly packed matrix. The highly porous composite was shown to be very absorbent, and the zirconia adhesive applied to hold the specimen was absorbed in part by the internal voids and is visible by the large grain high intensity features on the external side of the specimen.

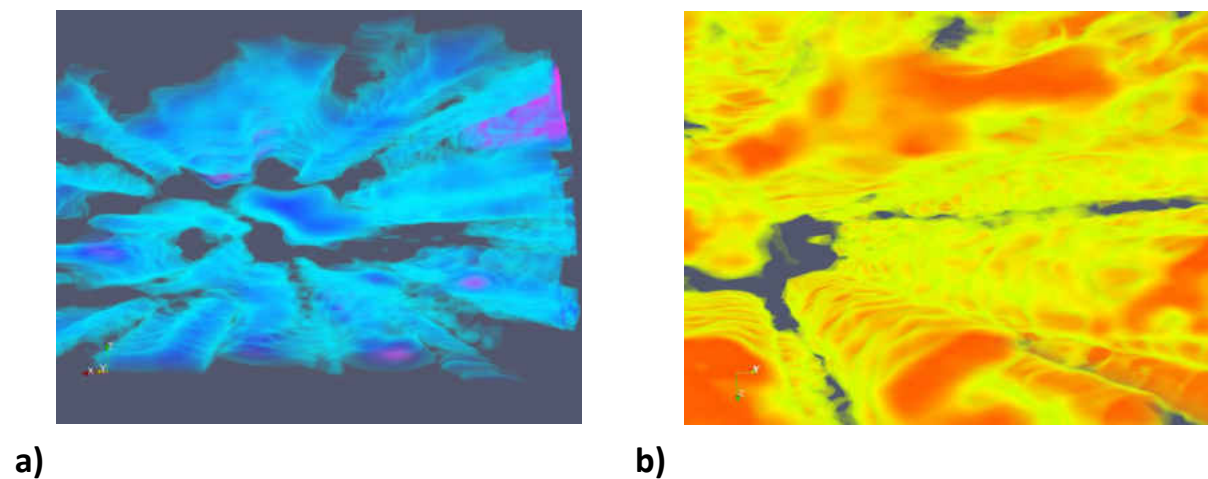


Figure 5.5: Isolation of fiber matrix interface: a) alumina matrix isolated from fiber and b) isolated alumina fibers with visible axial roughness. Image produced in ParaView<sup>TM</sup>.



Further isolation was conducted in ParaView<sup>TM</sup> and is presented in Figure 5.5. Additional filtering and coloring allowed small subsections of the composite to be isolated, where the matrix structure is presented in Figure 5.5a and fiber bundle in Figure 5.5b. Air voids can be identified in dark blue and bright pink. Of interest is the fiber pathways and channels through the matrix. The non-uniform surface pattern suggests that during the processing that there are some sintering effects active between the two constituents and that the matrix infiltration is rich in some zones while weaker in others.

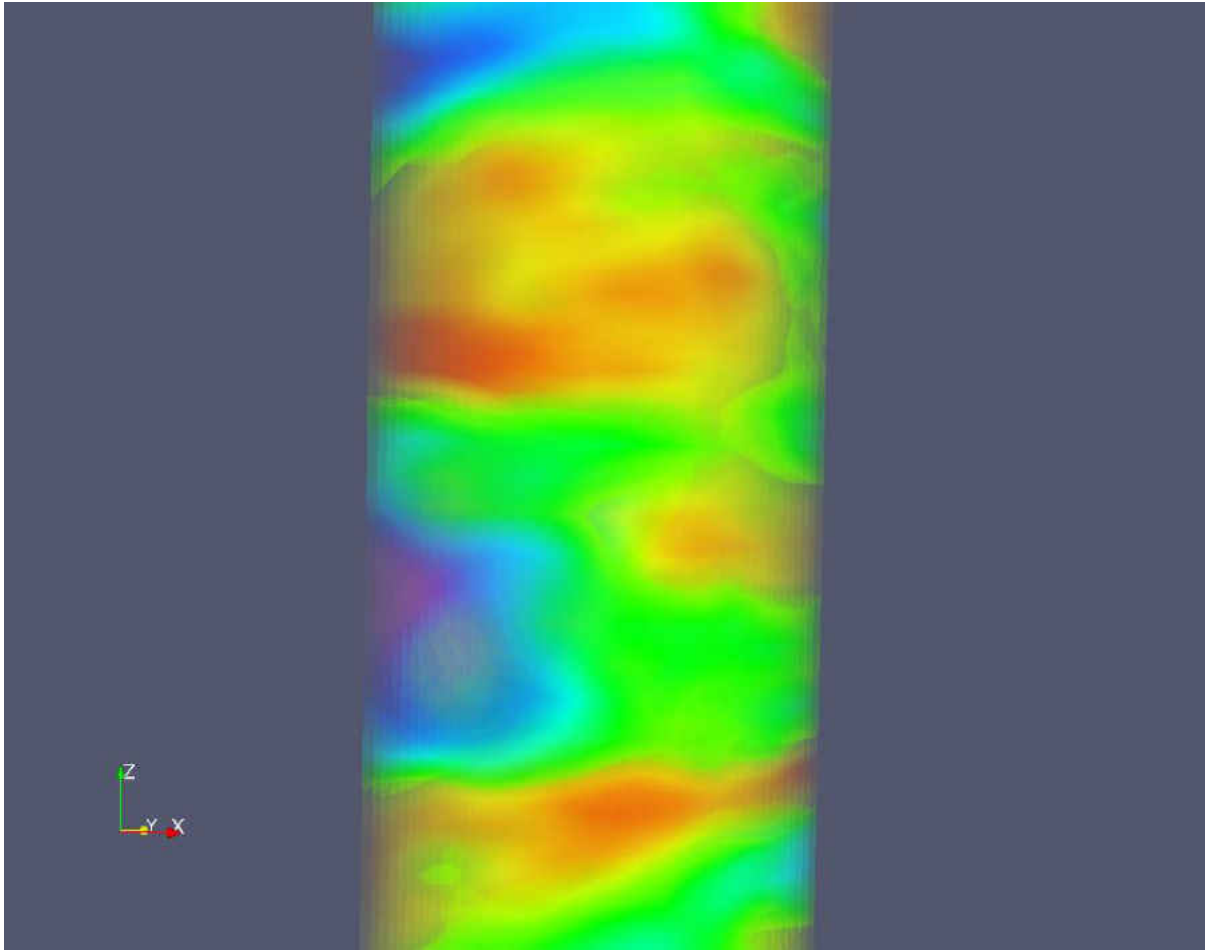


Figure 5.6: Isolation of sub-volume with fiber (red), matrix (green), and porosity voids (blue) for all alumina composite. Image produced in ParaView™.

Shrinking the sub-volume of interest, a small cuboid of material was visualized to highlight the composite partitioning. This is featured in Figure 5.6, where the fibers are colored in yellow/red, the matrix in green, and porosity in blue/purple. The fibers are running in the direction into the page on a  $45^\circ$  incline. The partitioning of the sub-volume features the expanse of the matrix between the fibers, and how porosity accompanies the

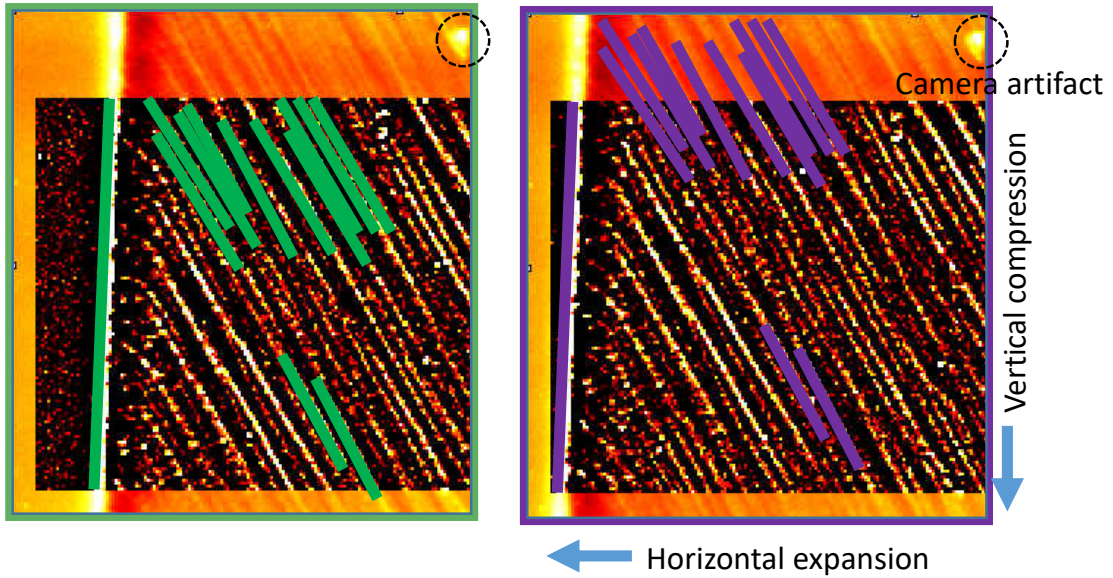
fibers. Quantitative analysis by DLR scientists has identified that porosity achieved was 35% [11].

In addition to tomographic measurements, radiography imaging was conducted under extreme environments to observe the degree of fiber rotation and compressible matrix to compliment the simulation studies. This measurement presented in Figure 5.7 looked to shed light on the simulation conducted by [6] which investigated the impact of isochoric and compressible matrix properties. Analysis was conducted during high temperature hold at 1200 °C and 40 MPa of applied compressive loading. Under these conditions, radiography measurement were conducted for 16 minutes and the in-situ fiber response was observed. The fibers can then be tracked to show the orientation throughout the conditions expected to trigger visco-elastic response [89]. This was conducted in an effort to identify the role of matrix compaction and shear against fiber re-alignment.

## High temperature measurements 1200° C and 40 MPa Compression

$t_m$ : Mid-hold 11 minutes

$t_f$ : End of hold 16 minutes



a)

b)

Figure 5.7: Radiography assessment: Tracking fiber motion and specimen rotation via radiography for conditions of 1200 °C and 40 MPa compressive loading at the *a*: mid-hold at  $t_i = 11$  minutes and *b*: at the conclusion of the hold  $t_f = 16$  minutes [89].

A zone of interest was set identify the specimen edge, and image processing was conducted to isolate and enhance the ease of tracking of the fibers. The condition at the mid point of the high temperature hold, ( $t_i = 11$  minutes) is presented in Figure 5.7a. In Figure 5.7b, the condition at the conclusion of the high temperature hold is presented ( $t_f = 16$  minutes), and the fibers have been tracked from their initial to their new resulting

location over the five minutes under the loading conditions. Displacement and orientation was inferred by the motion of the tracked pixels. The specimen edge motion was assessed to be 18 pixels in horizontal displacement direction with a fiber rotation realignment of  $-1^\circ$  [89]. The fibers are estimated to be on the order of  $10\ \mu\text{m}$ , which encompass approximately 3 pixels, suggesting a global extension on the order of  $5\ \mu\text{m}$  resulting from the applied compressive loading and application of the high temperature environment.

With the synchrotron techniques such as computed tomography and radiography, the fiber matrix system was successfully isolated for elucidating the mechanics of the composite and the influences of processing conditions on the system. Despite the nature of the all alumina composite, variations in grain size and packing allowed for a unique isolation perspective along with identification of zones of interest from processing that lead to variations in the mechanics spatially.

### **5.2.2 Investigating Azimuthal Texturing**

In an effort to identify fiber specific and matrix specific properties from diffraction measurements, experiments were designed to establish a baseline for X-ray diffraction properties under nominal loading and ambient conditions. This included utilizing composite constructed with alumina fibers in a Mullite matrix as well as specimens of pure alumina matrix material. For each specimen, the variations around the investigated lattice planes' corresponding Debye rings were quantified. The (110) and (113) planes for  $\alpha$

alumina were selected representing planes from sufficiently different spacial orientations,, as evident in Figure 5.1c. From literature it was anticipated that the fibers would show some distinct preferred orientation [110] especially with additional aging.

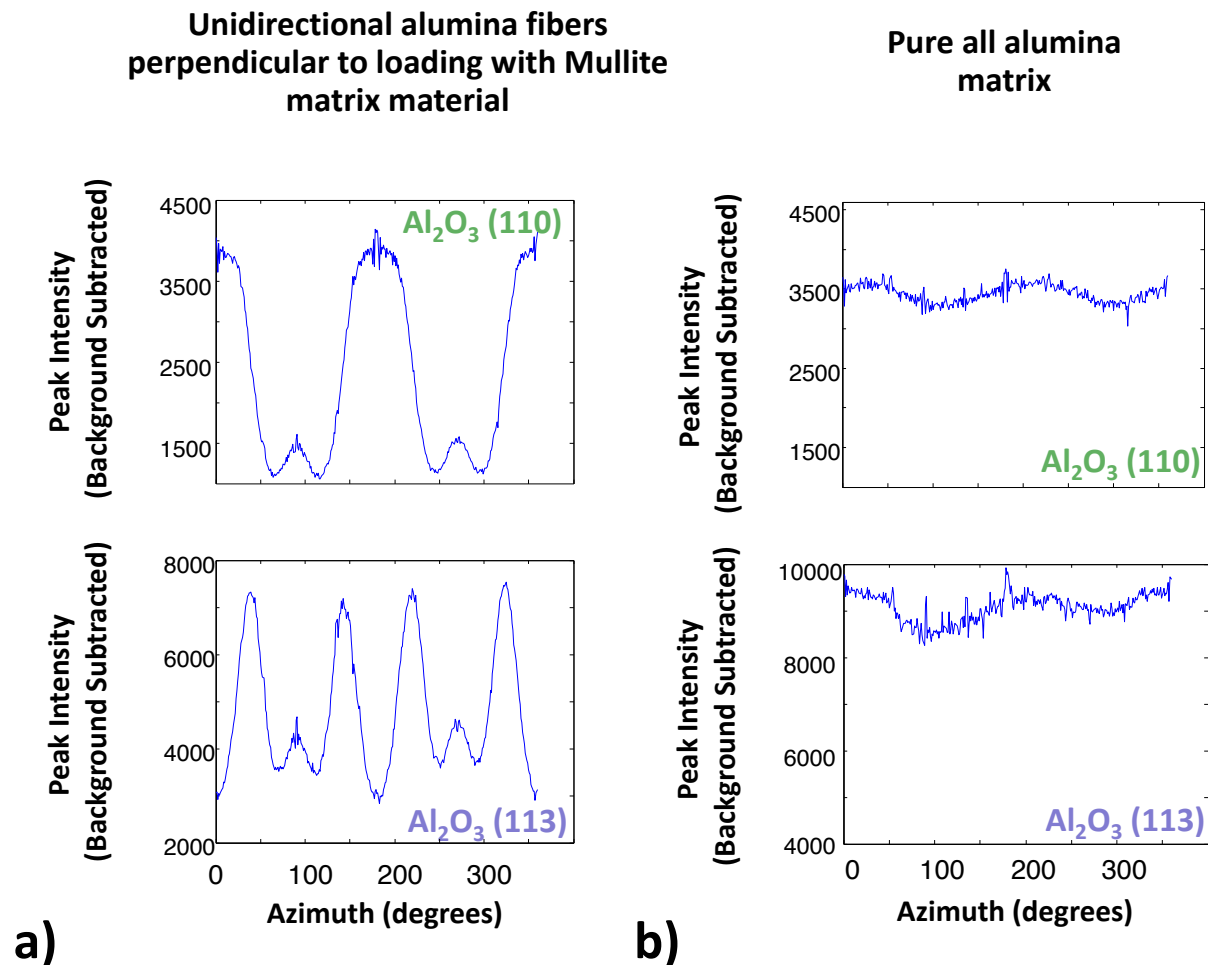


Figure 5.8: Azimuthal texturing investigation: a) Peak intensity plots for alumina (110) and (113) planes around the azimuth resulting from Nextel™ 610 (alumina) fibers in a Mullite slurry matrix, and b) azimuthal texturing for (110) and (113) pure alumina matrix specimens.

Presented in Figure 5.8 are the resulting azimuthal intensity variation for both lattice planes of investigation and both the alumina fiber in the Mullite matrix and the all alumina matrix specimens. For consistency the relating assessed lattice planes for the isolated fiber and pure matrix specimens are held with the same intensity variation range, where the maximum intensities may vary between specimens. The fiber assessment identifies sufficiently high azimuthally dependent intensities, with a very fine and consistent ring. This fine ring is attributed to the sufficiently high particle statistics and the nano-crystalline grains that build up the fibers. In contrast, the pure matrix material specimens show much lower azimuthally dependent variations, with a more coarse distribution; this is attributed to the larger grain size and size variation in the slurry [105, 68].

The distinction between with the isolated fibers and pure matrix specimens demonstrated that the dissimilar nature of the material would be identifiable under X-ray diffraction measurements. Its important to note for the sensitivity of the results that in the Mullite matrix there likely remains small amounts of unprocessed  $\alpha$  alumina in the Mullite mixture that may detract from from the overall clarity of the measurements, but these amounts are considered inconsequential on the overall trends of the composite system. Considering the nature of the specimens as pure  $\alpha$  alumina, the isolation techniques presented an exciting advance for utilizing X-rays for non-destructive evaluation and characterization for composites with self consistent reinforcement.

### 5.2.3 All Alumina Composites

The experimental methodology called for variations in specimen design to assist in identifying the constituent specific mechanics for the composite. These experiments were compared with the all alumina specimens. One challenge with identifying the mechanics of the composite is that the system evolves with heat treatment, such pure matrix material will evolve differently when independent from the fiber system. This is due to the influence of sintering and diffusion with the fiber [105, 69]. However, in the as processed condition large expanses of matrix rich material exist having different mechanical evolution over the course of its lifetime.

For comparison with the baseline texturing measurements, investigations into the evolution of pure matrix azimuthal intensity and peak characteristics were made. The findings are presented in Figure 5.9 and illuminate some of the effects of thermal aging for the pure matrix material. In Figure 5.9a, the comparison of the diffraction azimuthally integrated lineouts are presented. The as processed condition (blue) is overlaid with the aged condition (red), and highlights the difference between the two aged conditions. Two specimens were investigated which were cut from the same batch, but with only the aged specimen going through the prescribed thermal aging condition. The aged specimen demonstrates a negative peak broadening, which is indicative of a strain relief as well as a more uniform strain profile. This can lead to the conclusion that the aged matrix is increasing its density and continuing to sinter. Tomographic imaging was prescribed to



evaluate if additional strain relieving cracks were visible to further the assessment, and will be presented.

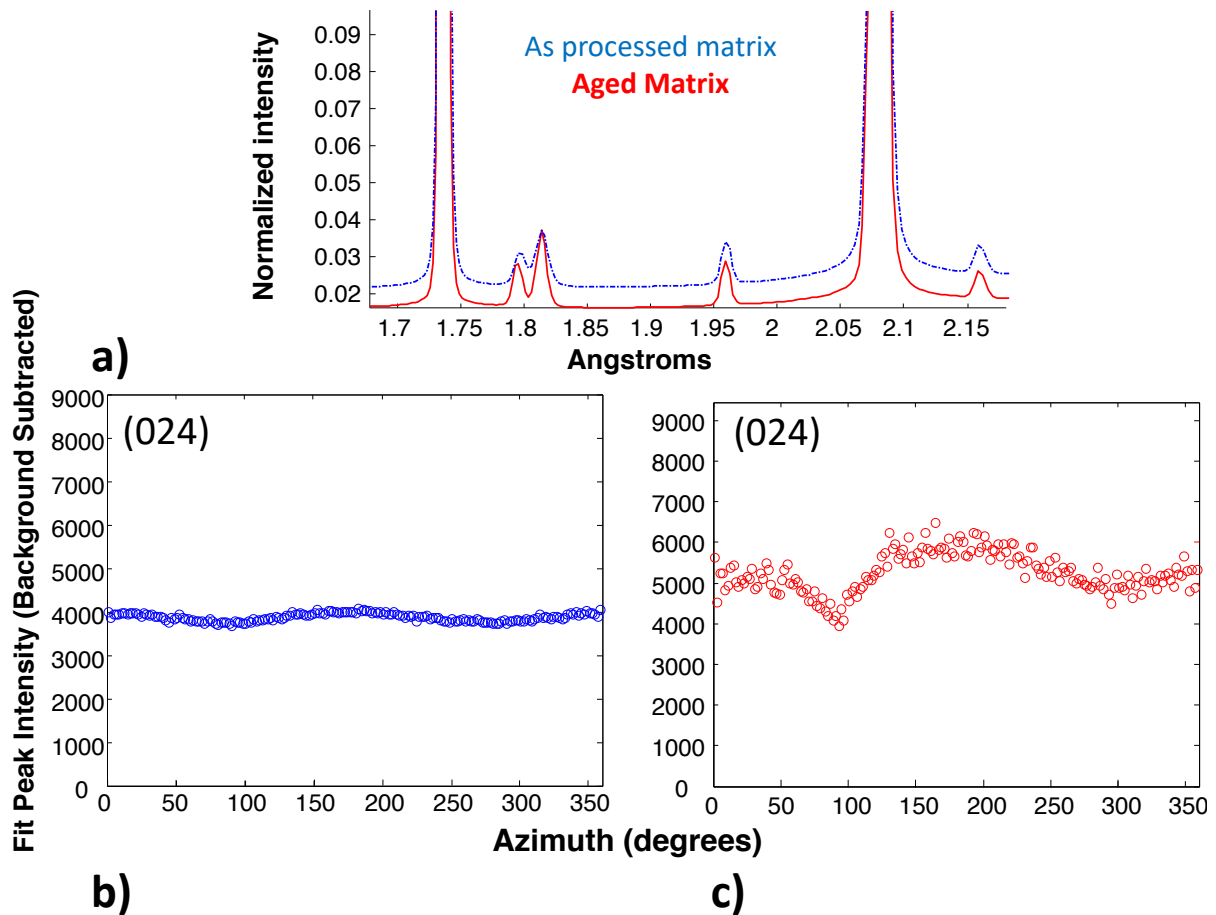


Figure 5.9: Azimuthal texturing investigation: a) comparison of diffraction ring intensity and peak broadening for pure matrix and aged pure matrix specimens, b) azimuthal texturing for (024) lattice plane for the pure alumina matrix specimen, and c) azimuthal texturing for lattice plane (024) for the heat treated aged pure alumina matrix specimens.

In Figure 5.9b and c, the azimuthal intensity variation is presented for the (024) lattice plane for  $\alpha$  alumina. It again shows minimal texturing variation, and is consistent with the other planes investigated. The aged specimen (red) plotted on the same intensity scale shows further intensity variations along with a less resolute trend due to the thermal aging process and its influence on the grain structure of the specimen. Further, tomographic measurements were used to investigate the micro structure evolution from as processed to the aged condition. This is presented in Figure 5.10.

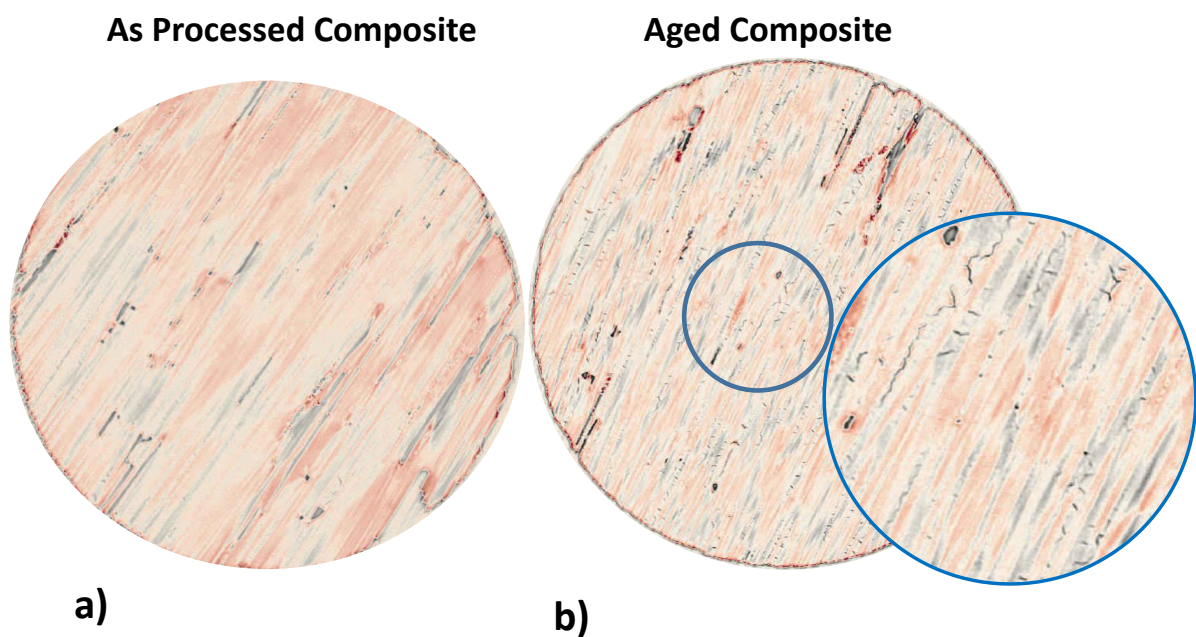


Figure 5.10: Tomographic inspection and comparison of cross sectional slices for a) pure alumina matrix specimens and b) heat treated aged pure alumina matrix specimens. Image processed in ParaView<sup>TM</sup>.

Comparing the as processed condition in Figure 5.10a with the aged condition in b, a clear distinction is made with the micro-structure. Cross sectional tomographic visualizations were made to compare the specimen's evolution. The aged composite shows a much higher amount of drying cracks, observed to form perpendicular to the fibers. Additionally, the meso-scale cracks appear to be exasperated and of larger size on average compared to the as processed specimen. This is attributed to the increasing density of the matrix acting to shrink the matrix which can enlarge or consolidate porosity or void structures. For clarity, the two specimens represent the same batch of matrix material with only the aged specimen going through the thermal treatment. As such, there is not a direct correlation between any void or crack structure in the two specimens. However, they can be used for correlating the evolution of the batch under thermal aging.

#### 5.2.4 Alumina Mullite Composites

Diffraction measurements were conducted for specimens utilizing a Mullite matrix with alumina reinforcement fibers, in an effort to provide a baseline for the alumina fiber's diffraction properties. These specimens feature  $\alpha$  alumina fibers and an alumino silicate matrix, with small amounts of raw alumina powder remaining in the matrix due to processing. This composite form of WHIPOX<sup>TM</sup> has been shown to have a reduction in mechanical properties [111] but offers increased creep resistance. Diffraction measure-

ments were conducted under nominal applied loading at ambient temperatures, and the azimuthally averaged lineout plot is presented in Figure 5.11.

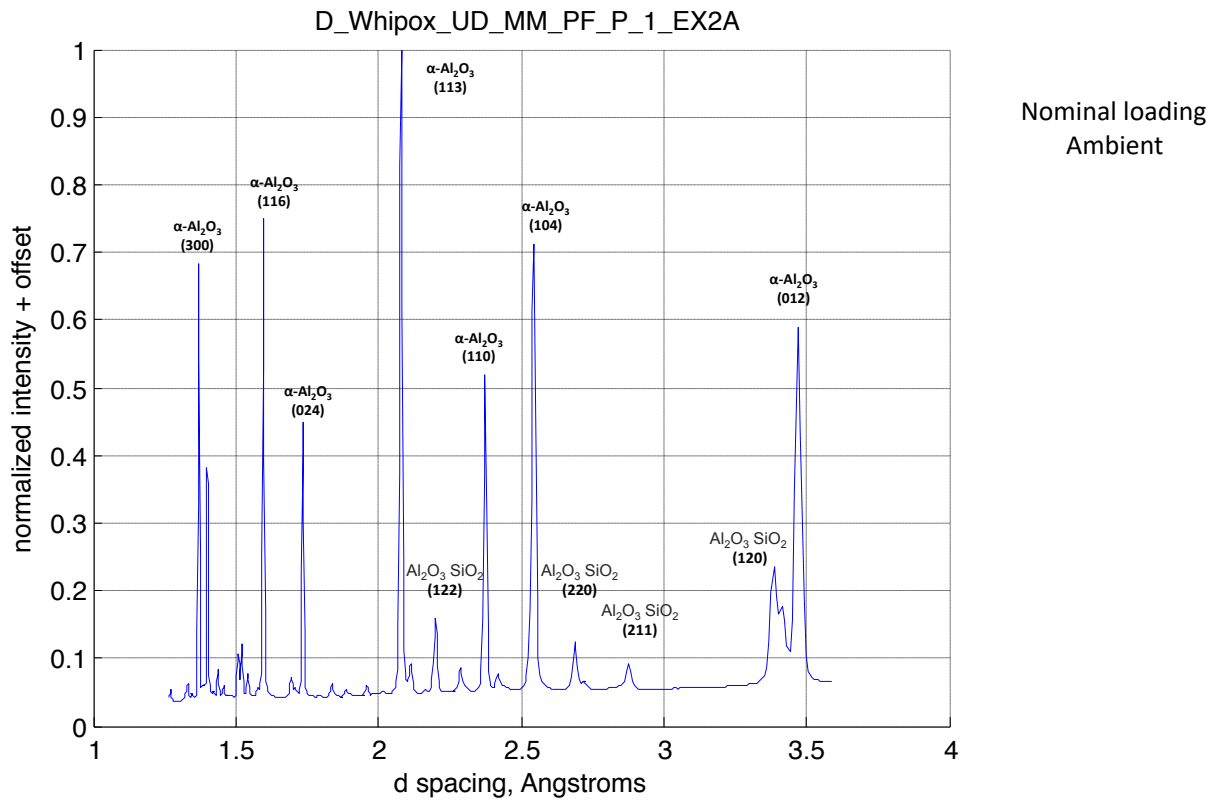


Figure 5.11: Diffraction ring lineout plots with peak and constituent identification for composites with alumina fibers with Mullite matrix.

The azimuthally averaged lineout plot enabled phase identification and lattice plane identification, and this is featured on the graph. The fibers of  $\alpha$  alumina are identified as the dominant peaks with the maximum intensities, while the Mullite matrix peaks are between 10% and 20% of the alumina peaks. This expected as the fibers represent the

higher diffraction volume of the system. Of particular interest is that of the matrix peaks appear to have a convolution of a low intensity peak to the right of its peak center, or some peak broadening, which is thought to be attributed to a duality in the strain state for the matrix existing in both tensile and compressive strain states across the diffraction volume.

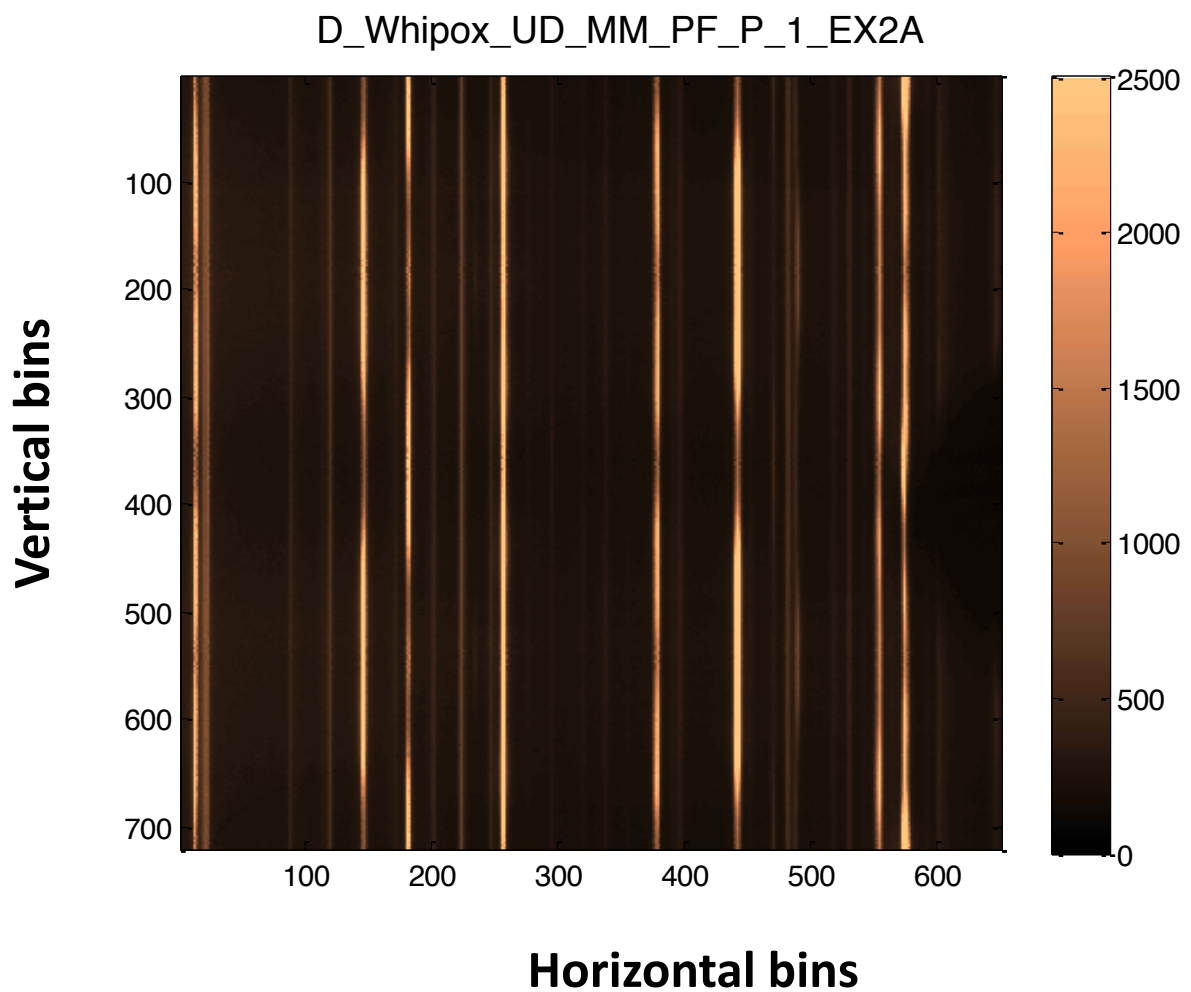


Figure 5.12: Transformed Debye rings for composite specimen with alumina fibers with Mullite matrix.

In Figure 5.12 the transformed Debye diffraction ring set is presented, featuring both alumina lattice planes and Mullite lattice planes. Visually it can be identified the intensity variation between the identified fiber peaks and the matrix peaks, where the fibers have some distinguishable azimuthal intensity texturing.

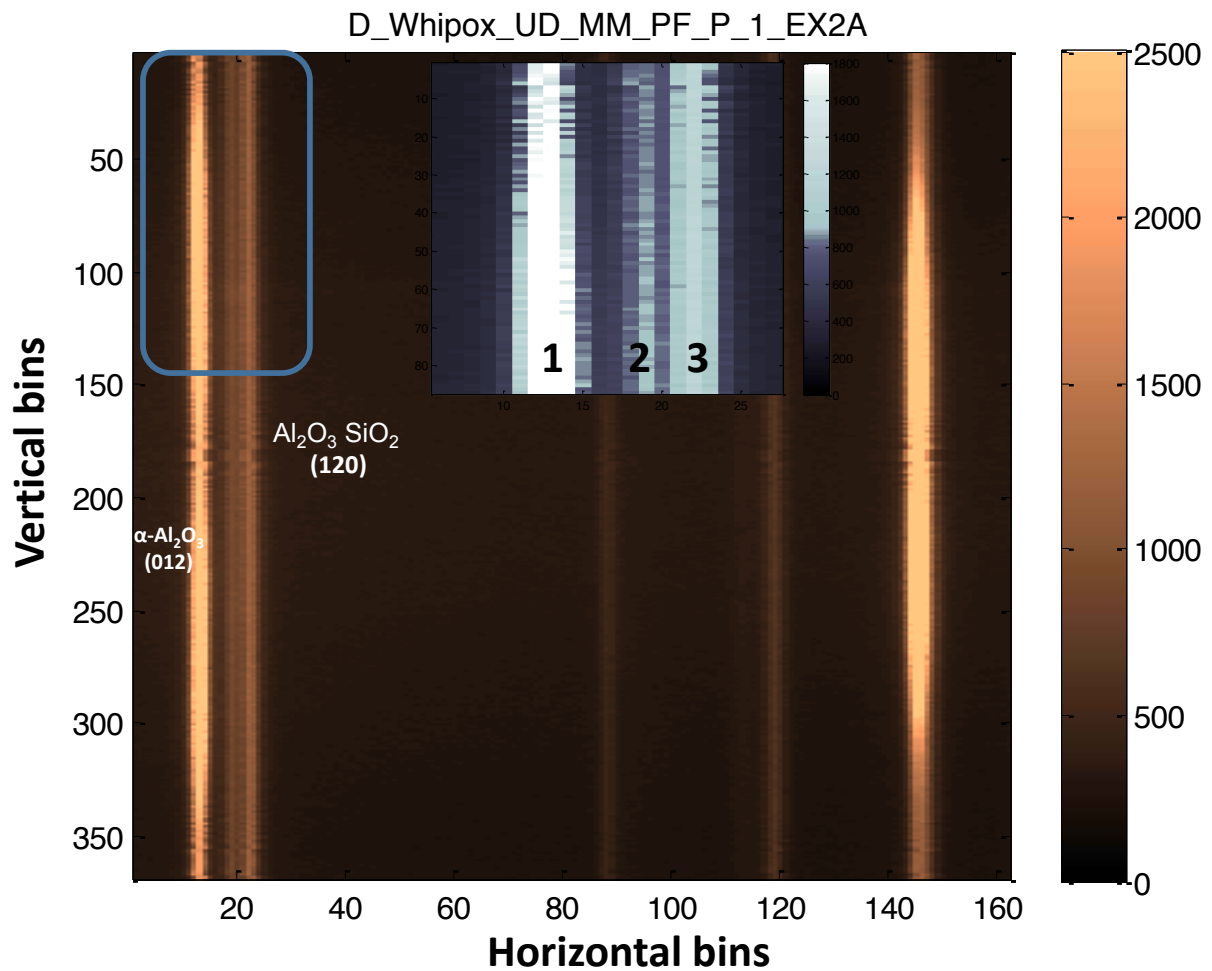


Figure 5.13: Zone of interest highlighted on the transformed Debye rings for (120) Mullite diffraction plane for composite specimen with alumina fibers with Mullite matrix.

Highlighted in Figure 5.13 is a segmented set of the matrix and fiber peaks representing the  $\alpha$  alumina (012) plane and Mullite (120) plane. Varying the colorbar and zooming into the ring set makes it possible to identify the satellite Mullite peak highlighted in zone 2. This could be attributed to either a dual strain state, with matrix components in both tensile and compressive strains due to processing, or that two stoichiometric states of Mullite exist simultaneously in the system [42]. Further investigations as to the mechanical loading and response were investigated to further elucidate the condition.

### 5.3 Mechanical Response

To understand the mechanics of the system further, experiments were conducted to compare the vertical and perpendicular ( $90^\circ$  and  $0^\circ$ ) fiber orientations for all alumina composites. Applied loading was elevated from nominal (87 N) to upwards of 1300 N which corresponds with an applied stress of 50 MPa across the cuboid specimens. It was postulated that the loading response for the fiber compared with the matrix would be appreciably different for the two dissimilar fiber orientations.

#### 5.3.1 Vertical Fiber Orientation

For all alumina specimens with vertical fiber orientation the compressive loading was aligned with the fiber's axis. While the alumina fibers have very high tensile strength

properties, the aspect ratio in compression for continuous fibers with a near 10 micron diameter puts the fibers into a condition expectant for micro-buckling or kinking [83, 131]. Kyriakides et al [83] and Fleck et al [47] both describe the mechanisms for fiber composites under applied compressive stresses may lead to micro buckling and plastic events, where fiber misalignment accelerates the condition. From this work's tomography analysis, it is expected that some misalignment of fibers exists along side matrix rich zones that disturb the stress distribution across the specimen spatially. From this, it was expected that the specimens would demonstrate very high lattice strains without exhibiting the same global effects.



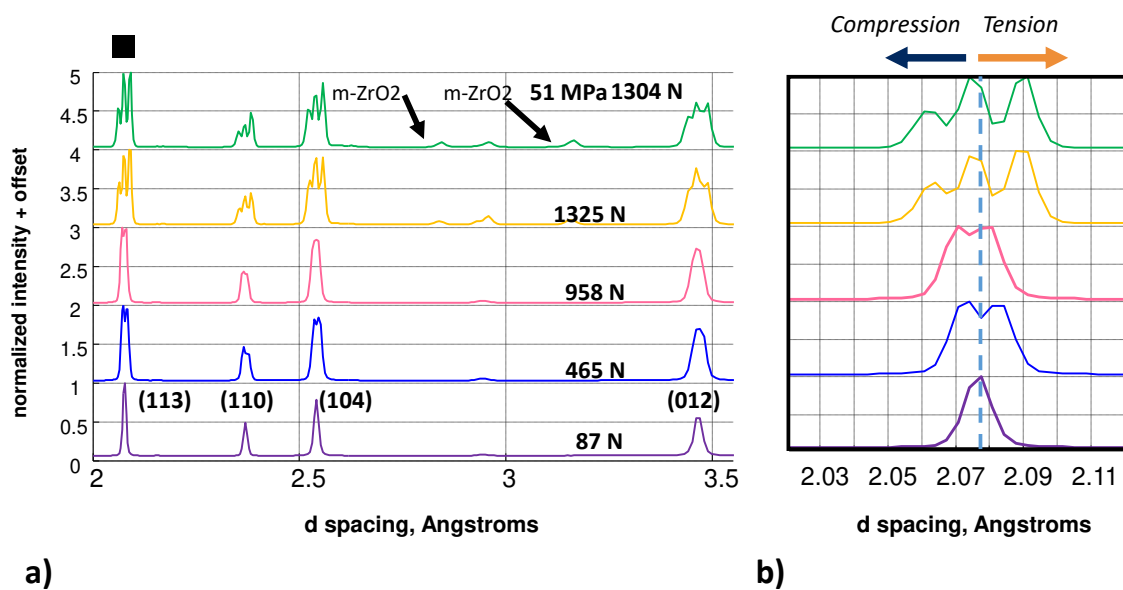


Figure 5.14: Diffraction azimuthally averaged lineout plot for all alumina composite with vertical fiber orientation with variations in applied nominal loading at ambient temperature: a) overview of main diffraction planes and b) highlighted subsection for the (113) alumina plane at approximately 2.07 Å.

Diffraction measurements were conducted for the specimen with increasing compressive load from nominal to upwards of 1300 N. Azimuthally averaged lineout plots are presented for the all alumina vertical fiber orientation under mechanical loading in Figure 5.14. Starting at the nominal condition, the observed peaks are identified for their corresponding lattice planes. The peaks begin as thin and clearly defined spikes, and with increasing applied mechanical loading the peaks begin to broaden. This is indicative of

an increasingly varied strain state for the averaged diffraction volume. Trace amounts of zirconia are visible beginning with the nominal loading condition, yet increase with applied loading. This is postulated to be in part due to the compressive state changing the probed volume that held more trace amounts of zirconia from the milling process, and the inclusion of trace amounts of contamination from the high temperature zirconia adhesive were present on the specimen. The monoclinic zirconia can be identified as a superposition of the fine grain resulting contamination from the milling process of the matrix, and the course grain found in the high temperature adhesive.

Of particular interest is the phenomena, identified in the azimuthally integrated lineouts, that shows that in response to the mechanical loading the  $\alpha$  alumina peaks first splitting into a doublet. This is clearly seen in Figure 5.14 for the lower load steps. This experiment was uniquely conducted as the loading axis was misaligned from the specimen's center axis, which resulted in much higher locally applied stresses than the 50 MPa loading would deliver otherwise. This resulted in the specimen losing alignment from the load path and the experiment halting at the end of the last load step (1304 N). It is important to clarify that the prior 3 load steps were sufficiently induced over the full duration of their 5 depth scans, starting from the tangential edge and moving towards center. Figure 5.14b highlights the (113) lattice plane for  $\alpha$  alumina and how the peaks broadening and subdivide across the applied loading variations. The peaks are assessed to broadening quite rapidly, resulting in over twice the overall peak width expansion. This is indicative of high variations in the strain state of the material.

An examination of the azimuthally averaged diffraction lineout plots and the corresponding transformed Debye ring images are presented in Figure 5.15. Here the depth scans are highlighted from the nominal applied loading case Figure 5.15a, b, and c; and compared with the intermediate loading step of 667 N in Figure 5.15d, e, and f. From the imaging plots (Figure 5.15b, c, e, and f) we can compare the tangential grazing location with the specimen central scan location and identify that there is not an obstruction for the beam nor a competing diffraction volume. Each measurement location was located in increasing 0.4 mm towards center, with a total of 5 measurement points including the tangential edge scan.

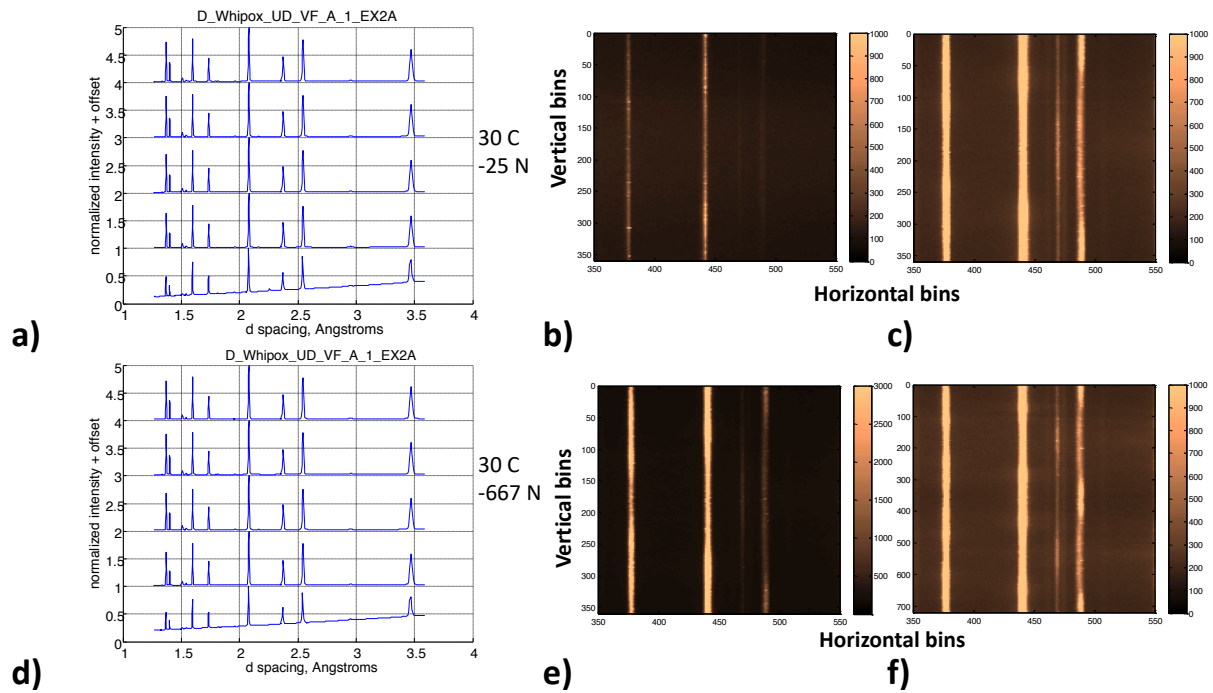


Figure 5.15: Investigation of aged all alumina composite with vertical fiber orientation: a) depth scans starting from tangential edge to sample center nominal applied loading, b) transformed Debye imaging for edge scan for nominal loading and c) transformed Debye imaging for center scan for nominal loading; d) depth scans starting from tangential edge to sample center for mid-level loading (667 N), e) transformed Debye imaging for edge scan for mid-level loading (667 N), and transformed Debye imaging for center scan for mid-level loading (667 N).

Examining the tangential edge scan featured in Figure 5.15a and d, the 0 condition on the stacked azimuthally averaged lineouts, it is readily identified that the beam passed through the specimen tangentially along with empty air. From the transformed diffraction ring set in Figure 5.15b and e, the diffraction response provides clues as to the fiber

and matrix response to mechanical loading. For the nominal applied loading where the diffraction volume includes empty air, the volume probed included a more even distribution of matrix and fiber material. Two grain structures are observed, including a fine continuous diffraction ring as well as an overlay of discontinuous coarser ring, due to a larger grain size. Comparing this response with the loaded condition in Figure 5.15e, the loaded response induces a peak broadening with the center shifted towards the right. This corresponds with a decrease in lattice plane resulting from compression.

From the specimen center scan location, Figure 5.15c and f yield higher intensity responses with broader rings. Visible intensity variations are detected between the two loading states, where Figure 5.15c shows the azimuth from  $0^\circ$  to  $180^\circ$  and Figure 5.15f presents  $0^\circ$  through  $360^\circ$ . For the higher loading step, there is more horizontal deviation which relates to the elastic strain in the composite. Also interesting to identify is that the fine grain response is superimposed with the coarser grain, and that this feature is more pronounced for increased mechanical loading. Evident from the transformed ring, noted at approximately 475 horizontal bins, is that the peak is splitting into two pronounced ring sets with a different grain structure. This was further compared with higher mechanical loads, presented in Figure 5.16.

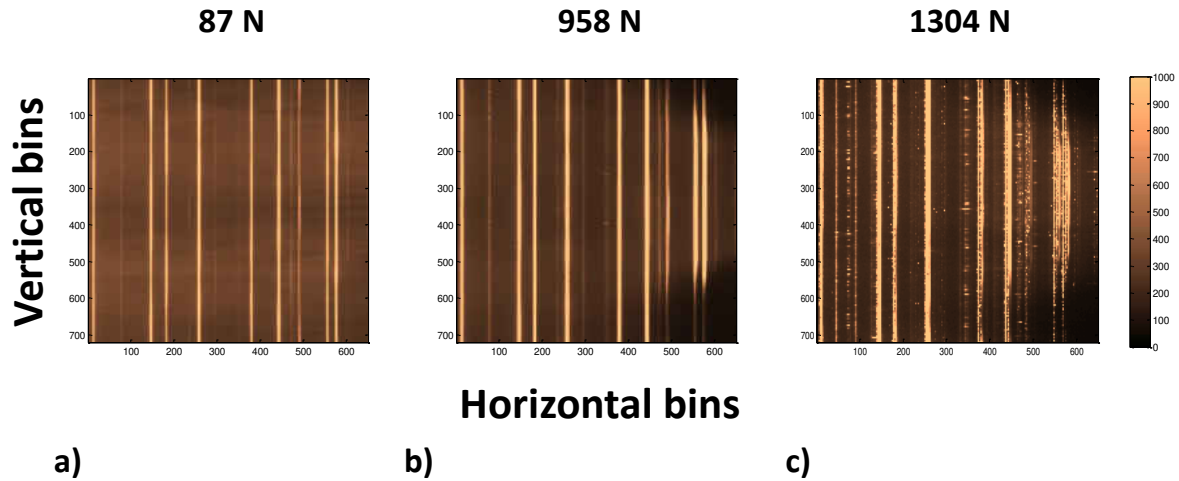


Figure 5.16: Comparison of Debye transform imaging for variations in applied loading on uni-axial (unaged) aligned alumina fibers in an alumina matrix from a) nominal, b) 958 N, to 1304 N while held at ambient temperature presenting the evolution of composite strain manifested in ring splitting.

Figure 5.16 presents three loading conditions including the nominal, 958 N, and 1304 N to compare the azimuthal variation that resulted in the azimuthally integrated lineouts demonstrating the evolution of single, doublet, and triune ring peaks in Figure 5.14. Each measurement scan represents the center scan location and is plotted on the same color bar intensity map for the full  $360^\circ$  azimuth. The superimposed fine grain and coarse grain diffraction ring textures grow to be more evident as the mechanical loading increases, with initial observations clearly apparent in the intermediate and high load

steps. Evidence of this superposition was also made available by altering the color bar for the nominal condition, though it is much less pronounced. The condition is further explored in Figure 5.17.

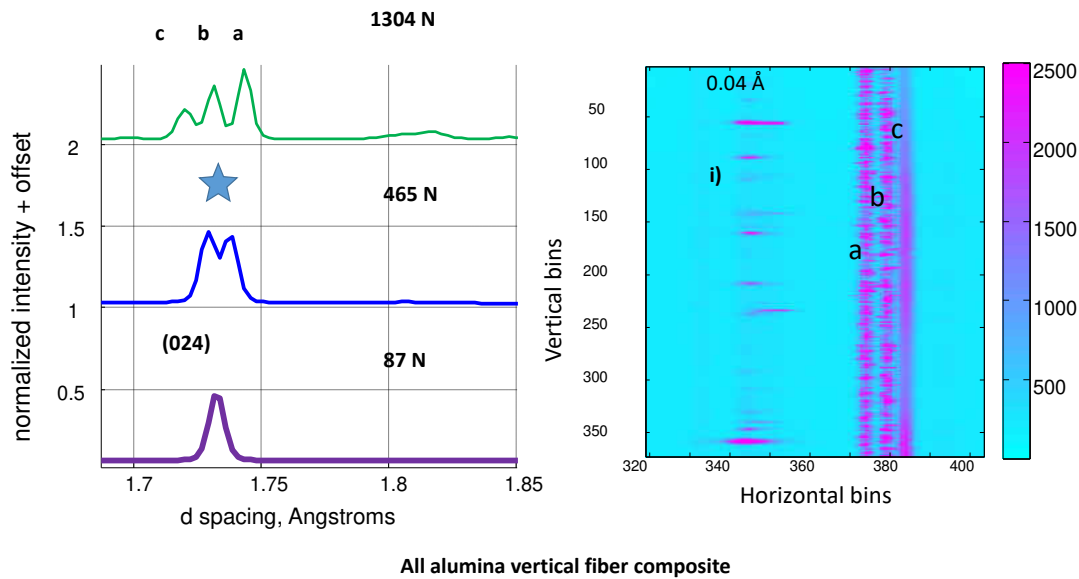


Figure 5.17: Identification of alumina (024) satellite peak formation and division with increased applied loading from nominal at ambient temperature: a) diffraction lineout peaks and b) transformed Debye ring imaging. Fiber (c) and matrix (a, b) peak subdivision is identified, along with zirconia contamination (i).

In Figure 5.17 the nominal condition is compared with a low mechanical loading of 465 N and high mechanical loading of 1304 N. The azimuthally integrated lineouts show the progression from the singlet thin peak to the more complex response. A highlight segment of the transformed rings for an azimuth of  $0^\circ$  to  $180^\circ$  is presented covering the

(024) plane, representing the 1304 N applied mechanical loading. Visually the transformed ring imaging demonstrates the subdivision of the representative lattice plane, evidence of an extreme variation in lattice plane dimensions. Highlighted in a, b, and c the triplet response demonstrates two very different grain structures. The contrast between the coarse and fine response is representative of the variation in grain size, while the horizontal imaging direction sees elongation and the vertical imaging direction sees increased azimuthal spacing. The vertical direction corresponds to the azimuthal direction while the horizontal represents the inverse of lattice plane spacing. Featured in i) is a group of well defined highly coarse grains, which are identified to be monoclinic zirconia, which may be the superposition of the trace zirconia residual from the matrix processing in addition to coarse grain zirconia cross contamination from the high temperature adhesive utilized in the setup. It is noted that the zirconia and alumina peaks have significant lattice plane spacing which allowed any contamination to be ruled out to be resulting in the high intensity peak splitting.

Figure 5.18 visually compares the nominal loading transformed diffraction rings with the high applied loading step of 1304 N. Here the zones of interest are aligned to compare the evolution of the peak locations, breadth, and azimuthal texture for both load steps. The nominal loading condition presents as continuous and thin rings, which is highly contrasted by the triplet split with highly azimuthally textured rings and fine continuous rings in parallel.



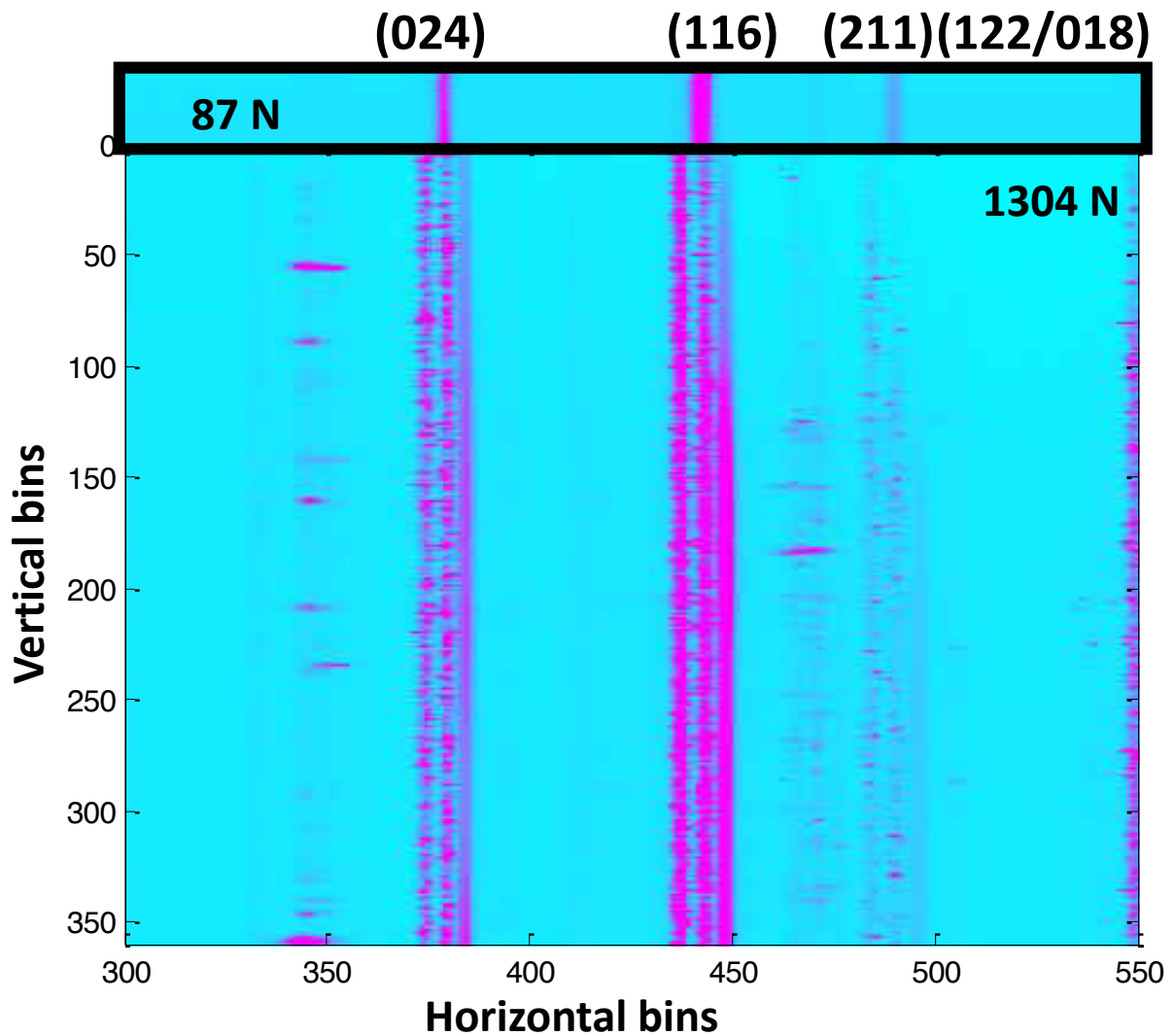


Figure 5.18: Comparison of transformed Debye ring imaging for applied nominal loading (87 N) and (1304 N) featuring peak shifting and division.

Taking the nominal loaded response as an indication of the residual strain condition, which is expected to have very low residual strains due to the lack of thermal expansion mismatch for the layers, the loaded condition highlights a peak in tensile (left of refer-

ence), a slight compression residual strain (slight right shift of reference), and a highly compressive peak (right of reference). For clarity, the bin pixel position is related to the inverse of lattice plane spacing. This shifting is explained to be the complex loading condition of the matrix material existing in part in tension as well as nominal or lightly compressive, while the uni-axial fibers take the high compressive loading. This complex strain state is supported by the fact that the matrix has very compressible high porosity micro-structure and is subjected to loading due to the fibers response. For fibers in a micro-buckling condition, it is expected that complex mechanical response for the matrix is possible. As discussed, the matrix particles have substantial variance in their size with large zones of matrix rich material where infiltration for the fibers may be insufficient. Further, the  $\alpha$  alumina crystal is known for high degrees of anisotropy due to the ratio of the a/c crystal dimensions. This may result in a distinction in the response between grains with their stronger direction aligned parallel to the loading axis compared with the alignment in the perpendicular direction. The diffraction response attributed to the fiber representative of the nano crystalline grain size is observed to shift into compressive lattice strain from the reference condition for all mechanical loading steps.

Further investigations included examining the aged vertical uni-directional fiber composite for similar features. The investigation revealed that diffraction peaks yielded a similar superposition of grain structures, but yielded minimal broadening or peak splitting. The aged investigation had a closer alignment of the load path and specimen center axis, but also demonstrates that the aged matrix material has appreciable sintering ef-

fects which result in a less compliant matrix and improved bonding to the fibers. This results in less matrix compaction and a less variable strain response across the composite. The finding of the diffraction ring splitting from a single, to doublet, to a triune state has not been identified previously and raised questions such as to if the beam clipped the loading platens, or if a phase change was occurring that could account for the large variation in lattice plane spacing in response to relatively small mechanical loads for ambient conditions. It was clarified through the use of the five locations azimuthally integrated lineouts that a foreign body was not present in the beam path. Additionally with a partial clipping or change of diffraction volume in the transmission direction, it would be expected to observe changes in the ring that influence higher lattice plane spacings differently than lower lattice plane spacing. Herein the results remain consistent across the lattice planes as well as the loading steps and measurement locations. The resulting splitting of the diffraction peaks is equivalent for all  $\alpha$  alumina lattice planes captured by the detector, and the splitting is not indicative of phase changes from  $\alpha$  to another form of alumina. For ambient conditions, it is not expected that the material would go through dramatic phase change in particular for low compressive loading of a ceramic.

From these findings the conclusions are asserted that confirm the hypothesis that the all alumina composites could effectively have their constituents isolated via synchrotron radiation, and that by comparing grain size and micro-structure the mechanics of the composite's constituents could be elucidated. Due to the complex diffraction peaks, strain analysis was not feasible as the neighboring peaks were not able to be numerically

isolated without imposing a bias due to azimuthal texturing. Future considerations will investigate the simultaneous fitting of multiple peaks to capture the tensile component, nominal, and compressive strain peaks; however this will require instituting a bias for the peak breadth and intensities.

### 5.3.2 Perpendicular Fiber Orientation

Specimens with the alumina fibers perpendicular to the loading axis as reinforcement in a Mullite matrix were tested with increasing mechanical loading for their response both mechanically and diffraction characteristics. With the inclusion of the Mullite matrix, it was possible to isolate the diffraction rings of just the alumina fibers. Analysis of the elastic strain was conducted, and additionally an investigation in to how the full width half maximum breadth of the fit lattice plane Debye ring. This was conducted for multiple planes, and the Figure 5.19 presents the (113)  $\alpha$  alumina plane. Mechanical loading was applied for a nominal condition, intermediate 15 MPa, and high 30 MPa application stress. The analysis demonstrates the ability to fit the in plane and out of plane strains, where the axial loading is observed the directly impact the  $e_{22}$  strain value. All the resulting strains are presented in Figure 5.19d, e, and f and are on the order of  $10^{-4}$ , which is near the limitations of strain analysis. However, the fitting method well captures the azimuthal lattice plane radius. The full width half maximum breadth is azimuthally resolved and plotted for all three loading conditions in Figure 5.19a, b,

and c. Full width half maximum breadth can be used as a strain measurement for azimuthally integrated plots, specifically the average of the azimuthally resolved full width half maximum breadth. For the 2D measurements, the azimuthal dependence can be captured where increased mechanical loading is seen to reduce the full width half maximum breadth in the loading directions. This is identified in the  $90^\circ$  and  $270^\circ$  range, and is observed to reduce linearly with the linear increases in applied loading stress. This can be related to the grains oriented in the loading direction developing a lower variance strain profile, which leads to a thinner breadth of the peak.

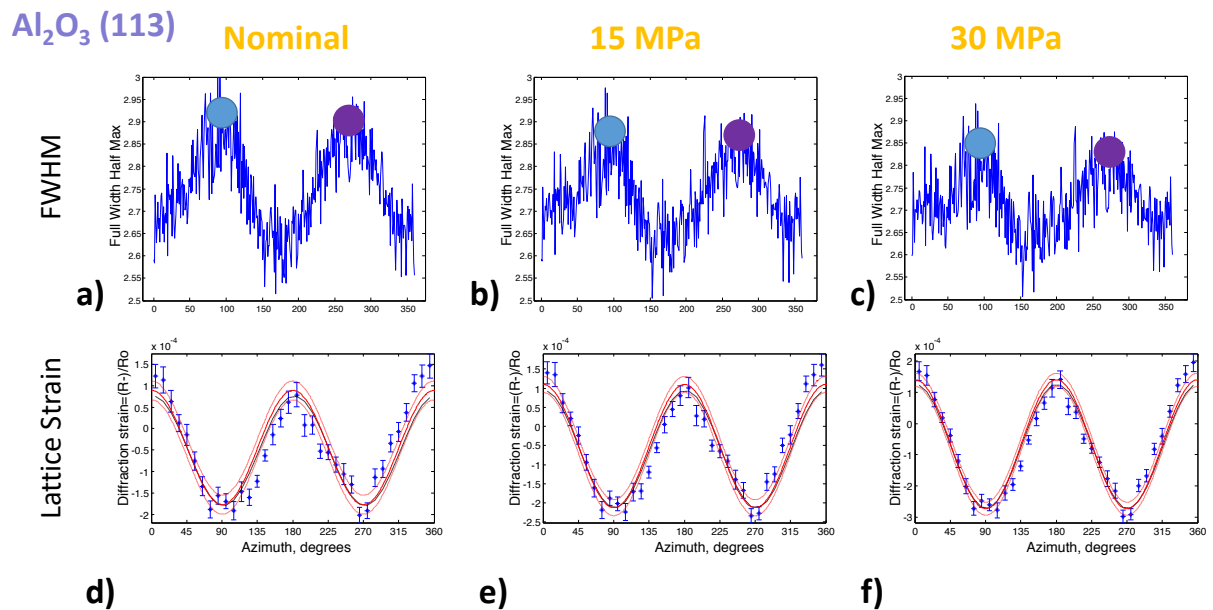


Figure 5.19: Comparison of alumina (113) plane full width half maximum (a, b, c) and diffraction strain (d, e, f) with variations in applied mechanical loading for quasi uni-directional perpendicular to loading alumina fibers with Mullite matrix as processed in ambient.

Figure 5.20 presents the analysis for the (110)  $\alpha$  alumina plane for both the lattice strain and full width half maximum breadth for the nominal, 15 MPa, and 30 MPa loading steps at ambient temperatures. The azimuthally resolved full width half maximum breadth variation is presented Figure 5.20a, b, and c, which can be assessed to have a linear variation at the peaks corresponding with the linear loading increases. The two maximums evolve in the same trend, but do not necessarily have the same slope. The strain fitting is presented in Figure 5.20d, e, and f and has more deviation from the double bell Fourier fit than the (113) plane.

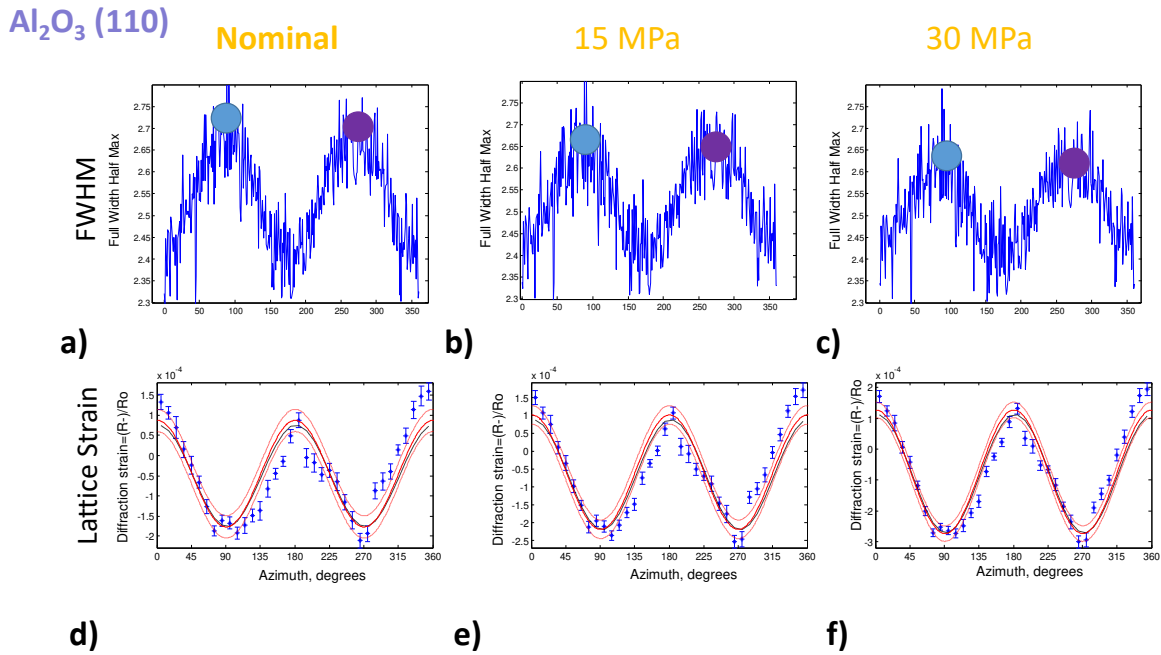


Figure 5.20: Comparison of alumina (110) plane full width half maximum (a, b, c) and diffraction strain (d, e, f) with variations in applied mechanical loading for quasi uni-directional perpendicular to loading alumina fibers with Mullite matrix as processed in ambient.

Figure 5.21 presents both  $\alpha$  alumina diffraction planes (110) and (113) resolved lattice strains with the variations in mechanical loading. The linear increase in applied mechanical loading stress generates a near linear lattice plane strain response, and some variation between the two planes is identified. This is expected as the calculated elastic modulus for the two (hkl) planes is not identical as seen in Figure 5.2.

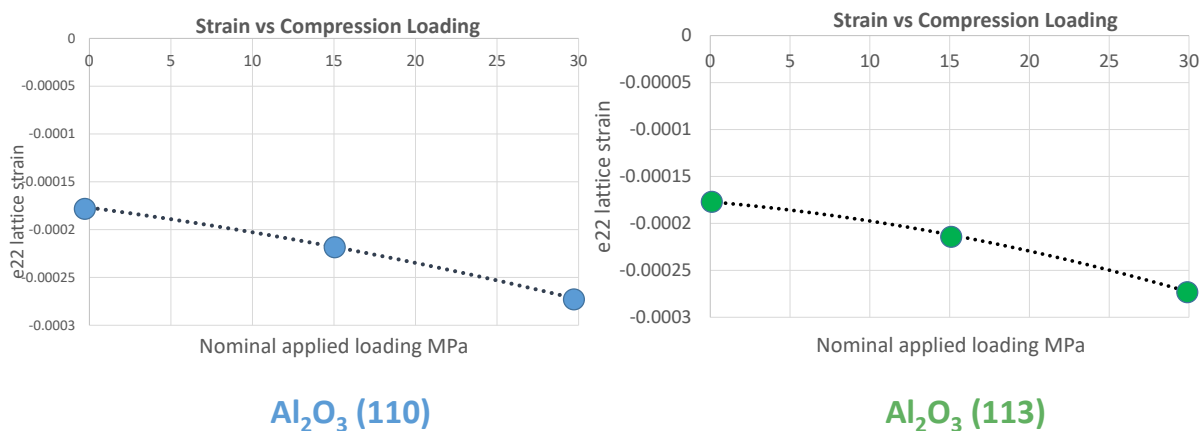


Figure 5.21: Comparison of alumina (110) and (113) planes diffraction strains with variations in applied mechanical loading for quasi uni-directional perpendicular to loading alumina fibers with Mullite matrix as processed in ambient.

The findings from the assessment on the perpendicular fiber to loading axis orientation are important as they demonstrate the ability to measure the lattice strains for the mixed material composites with Mullite matrix. Although this material has difference from the all alumina composite, it is still indicative of the composite mechanics and beneficial as it provides a clear baseline for comparison of the diffraction properties. Utilizing azimuthally resolved full width half maximum breadth evolution, it can be asserted than for all alumina composites the loading direction strain can be deciphered by binning the fitting analysis to small azimuthal degree ranges in the effort to isolate only the fiber strain component. Further, the fine grain structure of the fibers contrasts with the coarser



grain matrix and the full width half maximum breadth variations may lend additional isolation confidence.

## 5.4 Composite Mechanics

Synchrotron techniques were utilized to identify the composite mechanics in addition to the constituent isolation studies. Using a combination of computed tomography and diffraction measurements, holistic specimen properties and mechanics were able to be elucidated.

### 5.4.1 Imaging Analysis

Synchrotron computed tomography provided excellent 2D and 3D visualizations of the ceramic matrix composites. Of interest was assessing the resulting micro-structure for both the Mullite matrix and the alumina matrix with the alumina Nextel<sup>®</sup> 610 fiber bundle reinforcement. The reconstructed image stacks were assessed to identify zones of interest in both the diameter cross sectional plane (XY) and the height cross sectional plane (YZ). The specimens were created with a diminutive 1 mm diameter maximum and 3.2 mm height, and as such the findings must be interpreted for their sensitivity when comparing across a bulk volume of the material.

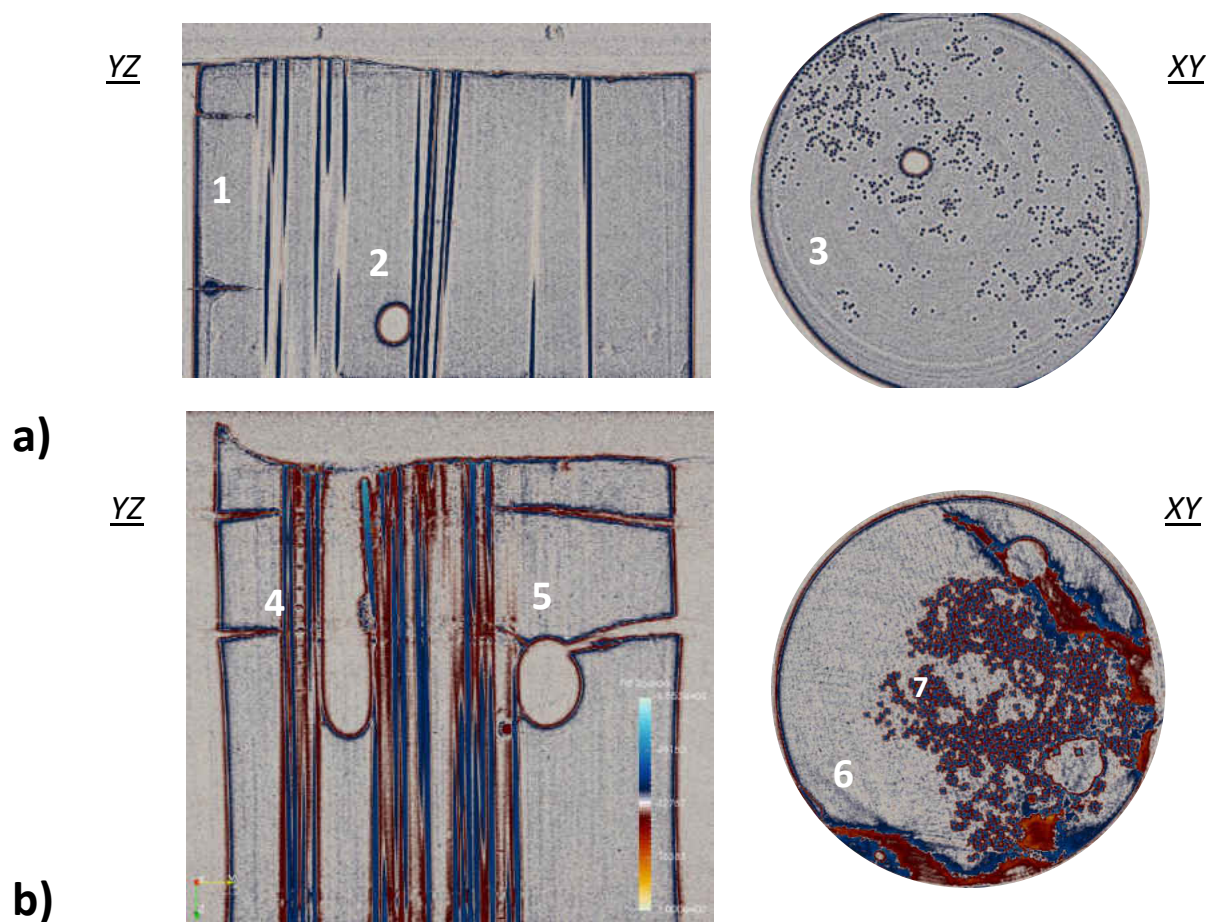


Figure 5.22: Tomographic imaging visual analysis for comparing a) alumina fiber bundle with alumina matrix and b) alumina fiber bundle with Mullite matrix. Image development conducted in Paraview™.

Figure 5.22a present the cross section slices for the full all alumina composite, constructed with an alumina fiber bundle infiltrated with alumina slurry. It can be compared for its resulting structure with Figure 5.22b, with the matrix replaced with Mullite slurry mixture. From the visualization, a number of zones of interest can be identified and are

labeled on the imaging. Voxel size remained a uniform 1.3 microns for both specimens. In zone 1 and 3, it can be identified that the exterior of the fiber bundle has matrix rich zones that are not reinforced locally by a fiber. However, comparing the cracks through the matrix rich zone to zone 4 and 6, it can be determined that the Mullite matrix suffers more dramatic crack propagation. This is attributed to the drying process and the lack of uniformity in the material properties between the dissimilar materials. Also noted in zone 4 is that the matrix between local fibers is identified in having a higher concentration of perpendicular drying cracks not present in the pure alumina mixture.

Broken or missing fibers are observed to create voids that during infiltration can become matrix rich zones or remain as air bubbles. Seen in zones 2 and 5, large voids can be observed, with the Mullite matrix showing crack propagation through the matrix rich zone and bridging the larger scale void structure. This type of defect has a profound influence on the damage tolerance and load partitioning for the composite. In zone 7 it can be observed that the packing density of the fibers is tight with pockets of matrix rich material inter dispersed. These images assist in being able to model and simulate the true distribution of processing irregularities which is critical to determining how the material will respond under extreme loading conditions. Figure 5.23b and c visualize the composite with alumina fibers reinforcing a Mullite matrix, and examinations of the columnar orientation, distribution, and misalignment are visible. In Figure 5.23c, the extensive Mullite matrix rich zones with drying cracks can be seen to propagate around fibers while connecting the void structures.

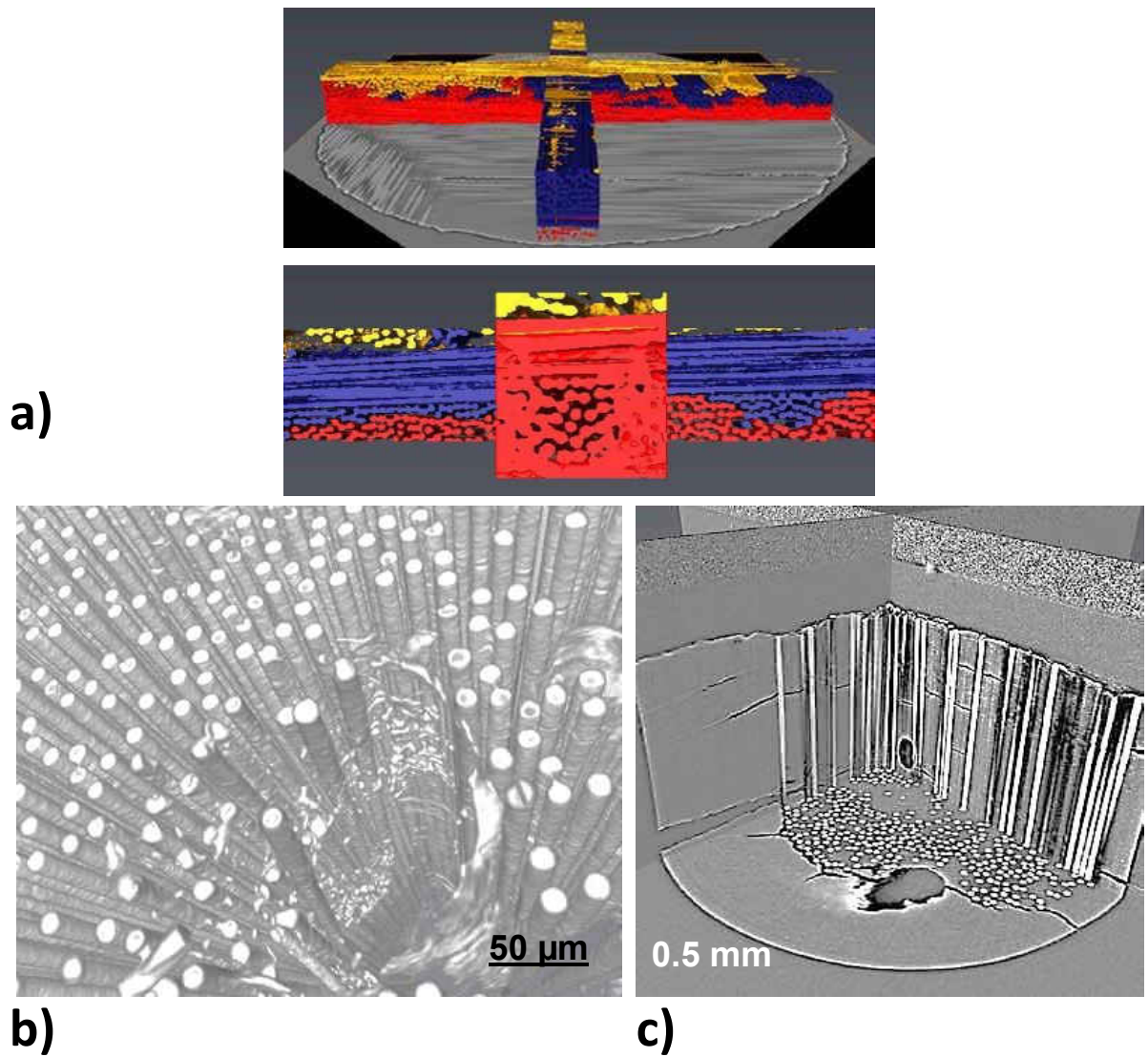


Figure 5.23: Tomographic imaging visual analysis for identifying a) alumina fiber de-bonding from alumina matrix, b) isolated alumina fibers from Mullite matrix, and c) visualization of alumina fibers and Mullite matrix processing defects. Images constructed by our collaboration in Avizo™ [11].

Additional tomographic analysis has been conducted on the reconstructed images by the German Aerospace Center scientists in Avizo Fire<sup>TM</sup>. Through the collaboration the images in Figure 5.23 were developed. Figure 5.23a demonstrates the segmentation of a  $\pm 45^\circ$  all alumina composite. It shows the post processing condition where fibers are pulling out from the matrix infiltration and where meso-scale porosity is located in the weave.

#### 5.4.2 Environmental Barrier Coated Composites

One key interest for the application of ceramic matrix composites continues to be there interaction with environmental barrier coatings to assist in extending the durability of the substrate. A common environmental barrier coating applied to all oxide ceramic matrix composites is  $Y_2O_3$  applied via atmospheric plasma spray [53, 125]. This creates a thick barrier coating to protect from corrosive environments and to provide thermal gradients from high temperature gases that can be used in application for turbines, turbomachinery, and combustion liners. With increases in inlet temperatures, weight reductions, and reductions in internal cooling flow, reductions in fuel burn could achieve over 5% from traditional turbine systems [53]. Currently research on WHIPOX<sup>TM</sup> substrates with  $Y_2O_3$  environmental barrier coatings is underway to examine the hot corrosion resistance and adherence strength [97, 19] attributed to a micron thick multi-layer diffusion zone.

Utilizing the synchrotron techniques for computer tomography, the interface was to be investigated. Cross sectional slices were generated, and they revealed several zones of interest presented in Figure 5.24. From the vertical cross section the environmental barrier coating is identified in zone 8 and 12. The atmospheric plasma sprayed coating is observed to have large but regular porosity. The interface zone is highlighted in zone 9 and 11, and is seen to be irregular in its thickness and smoothness, likely due to substrate roughness during application. During application of the environmental barrier coating, a small layer of matrix slurry is used to improve the adhesion to the substrate surface. This is identified in zone 10 above the fiber reinforced substrate.

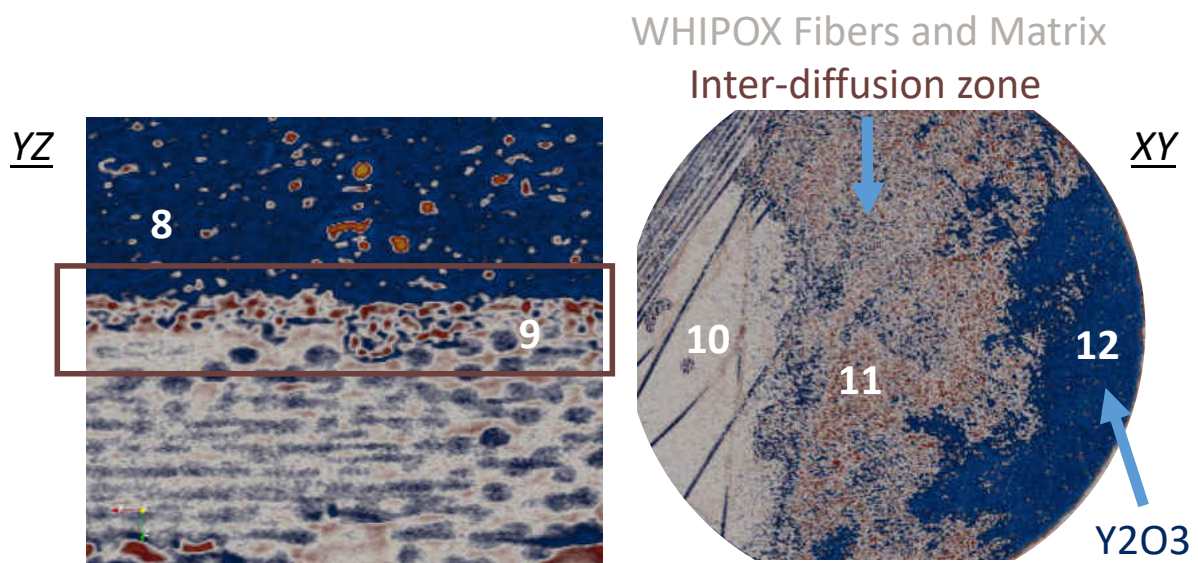


Figure 5.24: Tomographic cross sectional analysis for WHIPOX™ substrates with  $\pm 45^\circ$  orientation to investigate the non-uniform coating interface. Image development conducted in Paraview™.

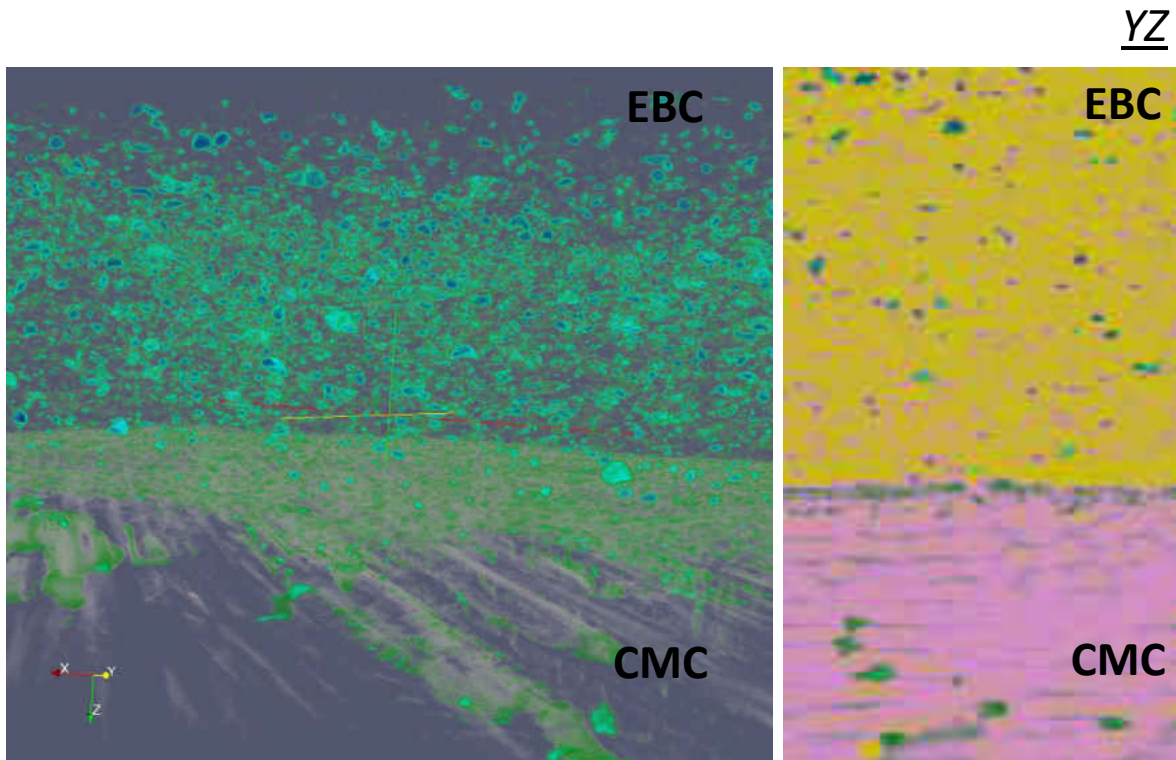


Figure 5.25: Tomographic analysis for WHIPOX<sup>™</sup> substrates with  $\pm 45^\circ$  orientation to investigate porosity variations between the EBC, CMC substrate, and the coating interface. Image development conducted in Paraview<sup>™</sup>.

Assessment in ParaView<sup>™</sup> allowed for segmenting the porosity of each layer, which is featured in Figure 5.25. This image features a 3D volume featuring only the air porosity structures, with two horizontal cross section slices directed into the page. From the visualization it is evident that there are three distinct porosity layers, corresponding with the environmental barrier coating, interface/slurry, and the substrate. Quantitative assessment of the pores was performed by German Aerospace Center scientists using the

statistical tool set in Avizo Fire<sup>TM</sup>. The analysis revealed 6% porosity in the atmospheric plasma deposited environmental barrier coating layer, comparing with 12% in the interface. Presented in Figure 5.26, a sub-volume featuring the three porosity zones is presented. The interface zone's porosity is seen to be small and tightly packed. This is attributed to the pre-processing for the deposition process, where raw aluminum is added to the alumina slurry to improve the deposition adherence. The addition adds material for the interphase interface development, which has been identified as an improvement on the durability. Porosity is attributed to the bi-product of aluminum spheres melting during deposition temperatures and evacuating as to leave a void structure.

This layer may be attributed to providing a zone to release thermal expansion mismatch strains, and may also indicate that the application methods may contribute to the risk for spallation. Findings from this study will be utilized by the scientists in the manufacturing department to investigate improvements in adherence to the substrate, potentially extending the applications and durability of ceramic matrix composites.



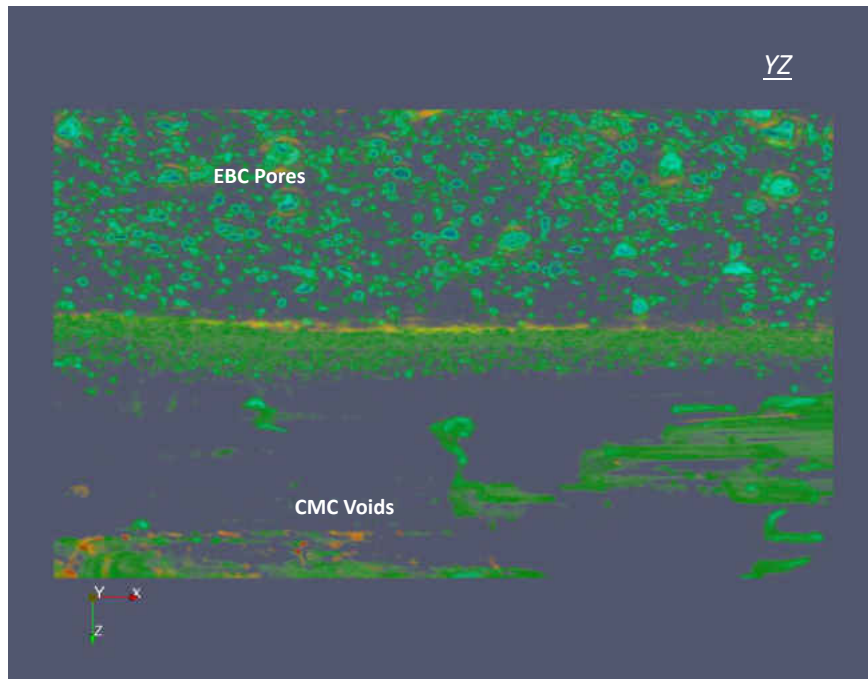


Figure 5.26: Defined interface porosity on a 3D visualization with uniform fine pore size, captured on WHIPOX<sup>TM</sup> substrates with  $\pm 45^\circ$  orientation with EBC coating. Image development conducted in Paraview<sup>TM</sup>.

## 5.5 Conclusions

Ceramic matrix composites have demonstrated great potential for application in power generation and combustion liners for aerospace applications. In an effort for full industry adoption, much work is needed to characterize application material response and identify high temperature mechanics and failure mechanisms. With such emphasis being placed on creep response and extreme high temperature behavior, simulation studies have been

conducted by the collaboration that showcased the response envelope for pure isochoric matrix against compressible matrix material. In an effort to understand this experimentally, synchrotron studies were designed and actualized. Fiber rotation and matrix compaction at 1200 °C under creep load holds. 2D radiography and 3D computed tomography have been conducted to identify processing defects that vary with fiber orientation and post processing heat treatment. Diffraction studies have been identified texturing in the fiber's alumina grains that far exceeds what is visible in the pure matrix.

Investigations into the loading response for quasi uni-directional fibers reinforcing a highly porous matrix were conducted and revealed both mechanical response from applied loading and the deviation as well as X-ray diffraction characteristics. Diffraction analysis resolved fiber matrix ring splitting from singlet, to doublet, to triune peaks with variations in grain structure. The superposition of diffraction rings was evident with the fine nano grain structure of the reinforcement fibers and the coarser grain matrix particles resulting in distinguishable variance.

Tomographic analysis was utilized to compare micro-structures for different versions of the WHIPOX<sup>TM</sup> including comparisons of matrix composition. Fiber matrix isolation was made possible using thresholding filtering, even achieved for all  $\alpha$  alumina composites. Further analysis from tomographic reconstruction revealed composite mechanics, and shed light on how the porosity and void structure's development that may govern spallation risk and such knowledge may yield enhancements that improve stability for environmental barrier coating interface on ceramic matrix composite substrates. Further,

the synchrotron resolved tomography geometries have been employed by the collaboration with the German Aerospace Center to advance numerical simulation efforts. This is featured in Figure 5.27 for a pure matrix specimen.

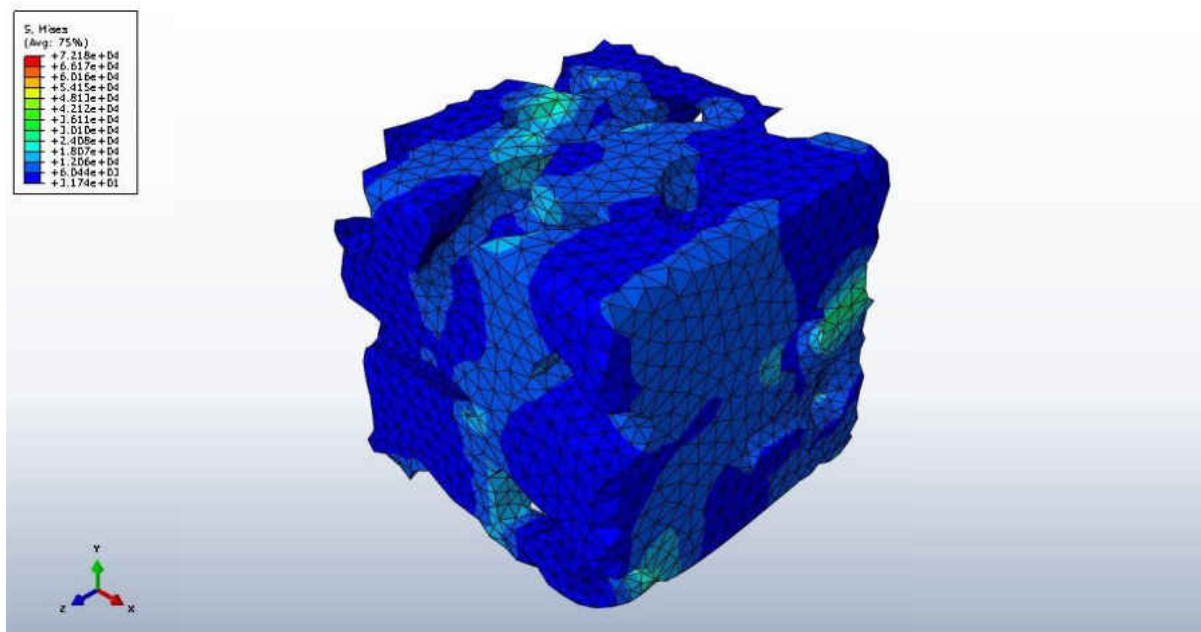


Figure 5.27: Modeling and simulation: realistic geometries and properties extracted from synchrotron studies now in use by DLR scientists [11].

## CHAPTER 6 CONCLUSIONS AND OUTLOOK

### 6.1 Conclusions

The scope of this study covered the characterization of high temperature aerospace materials including thermal barrier coatings and ceramic matrix composites. The goals were outlined as following:

1. Investigation of thermal barrier coating system strain response using in-situ measurements:
  - Multi-variable analysis of loading conditions
  - Identify high temperature mechanics for oxide scale and zirconia topcoat
  - Advancing design parameters for increasing durability and lifetime

For thermal barrier coatings the objectives included:

- *Objective 1:* Conduct full multi-variable analysis to determine the influence of loading variables during cycle evolution for YSZ and TGO ceramic layers
- *Objective 2:* Determine creep response and influences on viscoelastic mechanics
- *Objective 3:* Identify design elements for increased durability through tuning of system mechanics

The objectives were met by accomplishing the following research outcomes. *Objective 1:* A full mutli-variable assessment was conducted to determine the influence and magnitude of internal flow cooling, external applied force loading, and thermal exposure in cyclical application. Lattice strains for the axial and radial direction were resolved for the YSZ top coat layer and the internal thermally grown oxide scale. The findings demonstrate the importance of applying realistic environments to the test specimens, and discovered that during sufficiently high axial loading that the strain condition may be reserved in direction.

*Objective 2:* Visco-elastic mechanics were investigated by measuring the reduction in elastic lattice strain in the YSZ under high temperature exposure and applied mechanical load in force control. This response was able to be quantified and can be used to validate and improve modeling and simulation efforts. The ratio of strain rate creep response was plotted, and provides valuable insight into how the anisotropic, columnar structure of the YSZ behaves at high temperatures. Further, azimuthally resolved intensity variations were suggested to correlate with plastic strain due to grain rotation and re-alignment. This was plotted for the entire thermal cycle, revealing trends that were challenging to definitively establish with respect to the low intensity ratios and potential instrumentation uncertainty. This may contribute to supporting the complete understanding of the complex system mechanics. Oxide scale high temperature measurements reveled competing influences from the loading variables, but a creep response was identified and further

pronounced as the strain state drifted further into the tensile region for the axial component.

*Objective 3:* From the analysis, several elements can be gleaned as to improving the durability of the coating system. The findings demonstrate how the internal flow and applied mechanical loading produces converse effects, and show the magnitude of each variable. As such, with increased internal cooling to critical zones that experience higher mechanical loads it is possible to prevent the reversal from compressive to tensile strains (for the axial direction) whereby enhancing the durability. The reversal of the strain direction is associated with exasperating the failure mechanics in the system.

2. Understanding ceramic matrix composites' mechanics and its micro-structure's influence on its behavior:

- Isolate matrix and fiber via synchrotron imaging
- Identify influence of mechanical loading and partitioning

The goals of the investigation were rooted in the hypothesis that the all alumina oxide could be segmented via synchrotron studies for analysis based on the composite's grain size, porosity, and discrepancies in load partitioning and elastic modulus. Using quantitative imaging and synchrotron diffraction measurements, the investigation was designed to meet the following objectives:

1. *Objective 1:* Compare micro-structure of WHIPOX<sup>TM</sup> variations and investigate how defects arise from processing and in application loading.
2. *Objective 2:* Isolate the mechanics and load partitioning of the fiber and matrix by developing methods for examining anisotropy and texturing.
3. *Objective 3:* Comparison of diffraction strains for varying orientations and compositions of WHIPOX<sup>TM</sup> substrate to shed light on the mechanics of the system.

The objectives for the ceramic matrix composite study were met by accomplishing the following research outcomes. *Objective 1:* The micro-structure of various specimens was visualized and assessed for specimens with pure alumina matrix and Mullite matrix, the influence of aging on the matrix material, fiber weaves compared to quasi-unidirectional fiber orientations, and neat substrates compared with environmental barrier coating deposited specimens. The findings showed that the processing influence can achieve different crack and void structures, alter the internal porosity network, and change the applicable local mechanical properties.

*Objective 2:* By utilizing both X-ray diffraction and computer tomography, it was shown that the even the all  $\alpha$  alumina composites can have its constituents isolated. Via diffraction, the fiber and matrix demonstrated dissimilar grain size resulting in superimposition of diffraction points. During application of mechanical loading, this was observed to split the peak into a doublet, and then a triplet peak set with dissimilar grain structure for the satellite peaks. This is attributed to the matrix existing in a complex strain

profile, with both tensile and neutral components. The fiber, with its nano-crystalline grains resulted in a highly compressive and continuous diffraction profile. Examining anisotropy compared to the calculated elastic modulus for various (hkl) planes, and the evolution of full width half maximum breadth demonstrated the fiber's response differing from the matrix material. This was made possible by use of the dissimilar Mullite matrix material and isolated pure matrix specimens.

*Objective 3:* Uni-directional all alumina composites were able to have their strain state analyzed, as were composites under mechanical loading that included dissimilar Mullite matrix material. As processed all alumina composites were observed to have dissimilar grain texturing responses of which peak broadening and splitting were evident. This creates a complex response to evaluate the lattice plane strain with statistical certainty, and efforts to explore isolation of the constituents was conducted. The findings provide some techniques to improve the sensitivity of the strain analysis investigations which include: azimuthal binning a small range of azimuthal degrees around the primary loading axis ( $90^\circ$  and  $270^\circ$ ), isolation based on full width half maximum breadth, and the more complex challenge of isolating based on intensity and grain diffraction response to isolate the constituent's diffraction response.



## 6.2 Future Developments

This study provided significant outcomes to advance the state of the art, while yet providing more questions and challenges to develop for additional studies. Herein, extensive experimental testing has been conducted with results that can be leveraged by numerical simulation studies to improve the design and implementation of the ceramics in application. The forward direction necessitates continued investigation for the creation of such simulations and will allow for converting the findings into design criteria for improving durability. The measurement of the internal flow cooled surface for the thermal barrier coating's study will allow for more precise estimations of induced gradients, and will advance the modeling of the phenomena. Measuring the global displacement with methods such as digital image correlation or laser extensometers will allow for more complete analysis of visco-elastic phenomena. Further, conversions from lattice strains to induced stress require the compliment of numerical studies and measurements of depth resolved diffraction via in-situ rotation, but could allow for the complete elastic modulus tensor to be evaluated across the depth of the YSZ top coat.

Ceramic matrix composites studies are proposed to continue, including the addition of luminescent spectroscopy to further investigate the strain and stress state deviation for the matrix and fibers. In-situ measurements while the specimens are under high mechanical compressive loads is predicted to provide information to further validate the synchrotron findings.

Tomographic study revealed a number of important discoveries, yet quantitative analysis of zones of interest requires the development of numerical scripting to further study the distribution of flaws against processing techniques, evolution of void structure, and the coating interface evolution with high temperature exposure. Evaluating the isolated strain contributions of the complex and superimposed diffraction rings, for all alumina constituents, will enable statistically viable in-situ measurements of the constituents simultaneously. Some of these investigations are under way by the collaboration with the German Aerospace Center and have shown promising initial results as the developments continue.

## LIST OF REFERENCES

- [1] 3M. Nextel<sup>TM</sup> ceramic textiles technical notebook. Technical report, 2004.
- [2] J. Abraham, E. Sparrow, and J. Tong. Heat transfer in all pipe flow regimes: laminar, transitional/intermittent, and turbulent. *International Journal of Heat and Mass Transfer*, 52(3):557–563, 2009.
- [3] M. Ames, J. Markmann, R. Karos, A. Michels, A. Tschöpe, and R. Birringer. Unraveling the nature of room temperature grain growth in nanocrystalline materials. *Acta Materialia*, 56(16):4255–4266, 2008.
- [4] C. J. Armani, M. B. Ruggles-Wrenn, G. E. Fair, and R. S. Hay. Creep of Nextel<sup>TM</sup> 610 fiber at 1100°C in air and in steam. *International Journal of Applied Ceramic Technology*, 10(2):276–284, 2013.
- [5] S. M. Arnold, D. Cebon, and M. Ashby. Materials selection for aerospace systems. 2012.
- [6] K. Artzt, S. Hackemann, F. Flucht, and M. Bartsch. Anisotropic creep behavior of a unidirectional all-oxide CMC. *Mechanical Properties and Performance of Engineering Ceramics and Composites IX: Ceramic Engineering and Science Proceedings*, 35(2):1–14, 2014.
- [7] R. Bailey. The utilization of creep test data in engineering design. *Proceedings of The Institution of Mechanical Engineers*, 131(1):131–349, 1935.

- [8] H. Bale, M. Blacklock, M. R. Begley, D. B. Marshall, B. N. Cox, and R. O. Ritchie. Characterizing three-dimensional textile ceramic composites using synchrotron x-ray micro-computed-tomography. *Journal of the American Ceramic Society*, 95(1):392–402, 2012.
- [9] H. A. Bale, A. Haboub, A. A. MacDowell, J. R. Nasiatka, D. Y. Parkinson, B. N. Cox, D. B. Marshall, and R. O. Ritchie. Real-time quantitative imaging of failure events in materials under load at temperatures above 1,600°C. *Nature materials*, 12(1):40–46, 2013.
- [10] N. P. Bansal. *Handbook of ceramic composites*, volume 200. Springer Science & Business Media, 2006.
- [11] M. Bartsch, K. Artzt, J. Wischek, M. Eggeler, A. M. II, S. R. P. Kenesei, M. Eggeler, J. Okasinkski, and J. Almer. 3-dimensional microstructure characterization of porous ceramic matrix composites by x-ray tomography and fib-slicing as database for numerical modelling. In *International Conference and Expo on Advanced Ceramics and Composites*, 2017.
- [12] M. Bartsch, B. Baufeld, S. Dalkili, and I. Mircea. Testing and characterization of ceramic thermal barrier coatings. *Materials Science Forum*, 492-493:3–8, 2005.
- [13] M. Bartsch, B. Baufeld, S. Dalkilic, L. Chernova, and M. Heinzelmann. Fatigue cracks in a thermal barrier coating system on a superalloy in multiaxial thermo-mechanical testing. *International Journal of Fatigue*, 30(2):211–218, 2008.

- [14] M. Bartsch, K. Mull, and C. Sick. Effects of thermomechanical fatigue loading on damage evolution and lifetime of a coated super alloy. In *Fatigue & Fracture Mechanics: 33rd Volume*. ASTM International, 2003.
- [15] M. Bartsch, H. Richter, and K. Artzt. Ceramic fibre reinforced ceramic matrix materials with porous matrix-effect of porosity on mechanical behaviour. 2014.
- [16] W. W. Bathie. Fundamentals of gas turbines. 1984.
- [17] B. Baufeld, E. Tzimas, P. Hähner, H. Müllejans, S. Peteves, and P. Moretto. Phase-angle effects on damage mechanisms of thermal barrier coatings under thermomechanical fatigue. *Scripta materialia*, 45(7):859–865, 2001.
- [18] D. Bazin, C. Chappard, C. Combes, X. Carpentier, S. Rouzière, G. André, G. Matzen, M. Allix, D. Thiaudière, S. Reguer, et al. Diffraction techniques and vibrational spectroscopy opportunities to characterise bones. *Osteoporosis international*, 20(6):1065–1075, 2009.
- [19] T. Behrendt, S. Hackemann, P. Mechnich, Y. Shi, S. Hönig, S. Hofmann, and D. Koch. Development and test of oxide/oxide CMC combustor liner demonstrators for aero engines. In *ASME Turbo Expo 2016: Turbomachinery Technical Conference and Exposition*, pages V006T02A004–V006T02A004. American Society of Mechanical Engineers, 2016.
- [20] J. Betten. *Creep mechanics*. Springer Science & Business Media, 2008.

- [21] R. L. Borup, J. R. Davey, F. H. Garzon, D. L. Wood, and M. A. Inbody. Pem fuel cell electrocatalyst durability measurements. *Journal of Power Sources*, 163(1):76–81, 2006.
- [22] W. H. Bragg and W. L. Bragg. *X rays and crystal structure*. Bell, 1915.
- [23] W. L. Bragg. The structure of some crystals as indicated by their diffraction of X-rays. In *Proceedings of the Royal Society of London A: Mathematical, Physical and Engineering Sciences*, volume 89, pages 248–277. The Royal Society, 1913.
- [24] M. Bramble, R. Flemming, and P. McCausland. Grain size, 'Spotty' XRD rings, and chemin: Two-dimensional X-Ray diffraction as a proxy for grain size measurement in planetary materials. In *Lunar and Planetary Science Conference*, volume 45, page 1658, 2014.
- [25] D. J. Buchanan, R. John, and L. P. Zawada. Off-axis creep behavior of oxide/oxide Nextel<sup>TM</sup> 720/AS-0. *Composites Science and Technology*, 68(6):1313–1320, 2008.
- [26] E. Busso, H. Evans, Z. Qian, and M. Taylor. Effects of breakaway oxidation on local stresses in thermal barrier coatings. *Acta Materialia*, 58(4):1242 – 1251, 2010.
- [27] E. P. Busso and Z. Q. Qian. A mechanistic study of microcracking in transversely isotropic ceramic–metal systems. *Acta materialia*, 54(2):325–338, 2006.

- [28] G. Camus. Modelling of the mechanical behavior and damage processes of fibrous ceramic matrix composites: application to a 2-D SiC/SiC. *International Journal of Solids and Structures*, 37(6):919–942, 2000.
- [29] E. A. Carelli, H. Fujita, J. Y. Yang, and F. W. Zok. Effects of thermal aging on the mechanical properties of a porous-matrix ceramic composite. *Journal of the American Ceramic Society*, 85(3):595–602, 2002.
- [30] K. K. Chawla. *Ceramic matrix composites*. Springer, 1998.
- [31] K. K. Chawla. *Composite materials: science and engineering*. Springer Science & Business Media, 2012.
- [32] A. H. Chokshi. Diffusion creep in oxide ceramics. *Journal of the European Ceramic Society*, 22(14):2469–2478, 2002.
- [33] H. Cole. Bragg’s law and energy sensitive detectors. *Journal of Applied Crystallography*, 3(5):405–406, 1970.
- [34] P. Costamagna, L. Magistri, and A. Massardo. Design and part-load performance of a hybrid system based on a solid oxide fuel cell reactor and a micro gas turbine. *Journal of Power Sources*, 96(2):352–368, 2001.
- [35] P. Debye. Interferenz von röntgenstrahlen und wärmebewegung. *Annalen der Physik*, 348(1):49–92, 1913.

- [36] R. O. Diaz. In-situ stress measurements of EB-PVD thermal barrier coatings using synchrotron x-ray diffraction under thermo-mechanical loading. Master's thesis, University of Central Florida, 2010.
- [37] D. Dimos and D. L. Kohlstedt. Diffusional creep and kinetic demixing in yttria-stabilized zirconia. *Journal of the American Ceramic Society*, 70(8):531–536, 1987.
- [38] H. Dölle and V. Hauk. The measurement of residual stresses of general orientation by x-ray diffraction techniques. *Haerterei-Techn. Mitt.,(West Germany)*, 31(3):165–168, 1976.
- [39] M. Dorfman, D. Sporer, P. Meyer, et al. Thermal spray technology growth in gas turbine applications. 2013.
- [40] J. Drenth. *Principles of protein X-ray crystallography*. Springer Science & Business Media, 2007.
- [41] J. M. Drexler, A. Aygun, D. Li, R. Vaben, T. Steinke, and N. P. Padture. Thermal-gradient testing of thermal barrier coatings under simultaneous attack by molten glassy deposits and its mitigation. *Surface and Coatings Technology*, 204:2683–2688, 2010.
- [42] D. J. Duval, S. H. Risbud, and J. F. Shackelford. Mullite. In *Ceramic and Glass Materials*, pages 27–39. Springer, 2008.



- [43] H. E. Eaton, G. D. Linsey, E. Y. Sun, K. L. More, J. B. Kimmel, J. R. Price, and N. Miriyala. EBC protection of SiC/SiC composites in the gas turbine combustion environment: Continuing evaluation and refurbishment considerations. In *ASME Turbo Expo 2001: Power for Land, Sea, and Air*, pages V004T02A010–V004T02A010. American Society of Mechanical Engineers, 2001.
- [44] C. Eberl, X. Wang, D. S. Gianola, J. T. D. Nguyen, M. Y. He, A. G. Evans, and K. J. Hemkerz. In situ measurement of the toughness of the interface between a thermal barrier coating and a Ni alloy. *The American Ceramic Society*, 94 [S1]:S120S127, 2011.
- [45] T. Eggers, J. Longo, J. Turner, W. Jung, M. Hörschgen, A. Stamminger, A. Gülhan, F. Siebe, G. Requardt, T. Laux, et al. The shefex flight experiment pathfinder experiment for a sky based test facility. *AIAA Paper*, 7921:2006, 2006.
- [46] A. G. Evans, D. Mumm, J. Hutchinson, G. Meier, and F. Pettit. Mechanisms controlling the durability of thermal barrier coatings. *Progress in materials science*, 46(5):505–553, 2001.
- [47] N. Fleck and B. Budiansky. Compressive failure of fibre composites due to microbuckling. In *Inelastic deformation of composite materials*, pages 235–273. Springer, 1991.

- [48] M. Gell, J. Eric, V. Krishnakumar, K. McCarron, B. Barber, Y.-H. Sohn, and V. K. Tolpygo. Bond strength, bond stress and spallation mechanisms of thermal barrier coatings. *Surface and Coatings Technology*, 120:53–60, 1999.
- [49] J. Gladden, J. H. So, J. Maynard, P. Saxe, and Y. Le Page. Reconciliation of ab initio theory and experimental elastic properties of  $\text{Al}_2\text{O}_3$ . *Applied Physics Letters*, 85(3):392–394, 2004.
- [50] J. Göring, F. Flucht, and H. Schneider. Mechanical behavior of whipox ceramic matrix composites. *High Temperature Ceramic Matrix Composites*, pages 675–680, 2001.
- [51] J. Göring, S. Hackemann, and B. Kanka. Whipox<sup>TM</sup>: Ein faserverstärkter oxidkeramischer werkstoff für hochtemperatur-langzeitanwendungen. *Materialwissenschaft und Werkstofftechnik*, 38(9):766–772, 2007.
- [52] S. M. Goushegir, P. O. Guglielmi, J. G. da Silva, M. P. Hablitzel, D. Hotza, H. A. Al-Qureshi, and R. Janssen. Fiber-matrix compatibility in an all-oxide ceramic composite with RBAO matrix. *Journal of the American Ceramic Society*, 95(1):159–164, 2012.
- [53] J. E. Grady. CMC technology advancements for gas turbine engine applications. 2013.
- [54] J. Gross, A. Waters, H. Martz, and B. Koziowski. *APS Performance Summary-Update*. United States. Department of Energy, 2004.

- [55] A. Guinier. *X-ray diffraction in crystals, imperfect crystals, and amorphous bodies*. Courier Corporation, 1994.
- [56] S. Hackemann, F. Flucht, and W. Braue. Creep investigations of alumina-based all-oxide ceramic matrix composites. *Composites Part A: Applied Science and Manufacturing*, 41(12):1768–1776, 2010.
- [57] M. Harvey, C. Courcier, V. Maurel, and L. Rémy. Oxide and TBC spallation in  $\beta$ -NiAl coated systems under mechanical loading. *Surface and Coatings Technology*, 203(5):432–436, 2008.
- [58] V. Hauk. *Residual stresses*. DGM Informationsgesellschaft Verlag, 1993.
- [59] B. He. Introduction to two dimensional X-ray diffraction. *Powder Diffraction*, 18(2):71–85, June 2003.
- [60] B. B. He. *Two-dimensional X-ray Diffraction*. John Wiley & Sons, 2011.
- [61] M. T. Hernandez, D. Cojocar, M. Bartsch, and A. M. Karlsson. On the opening of a class of fatigue cracks due to thermo-mechanical fatigue testing of thermal barrier coatings. *Computational Materials Science*, 50(9):2561–2572, 2011.
- [62] M. T. Hernandez, A. M. Karlsson, and M. Bartsch. On TGO creep and the initiation of a class of fatigue cracks in thermal barrier coatings. *Surface and Coatings Technology*, 203(23):3549 – 3558, 2009.

- [63] A. Heuer, G. Fryburg, L. Ogbuji, T. Mitchell, and S. Shinozaki.  $\beta$  to  $\alpha$  transformation in polycrystalline SiC: I, microstructural aspects. *Journal of the American Ceramic Society*, 61(9-10):406–412, 1978.
- [64] C. Huang, K. S. Tan, J. Lin, and K. L. Tan. XRD and XPS analysis of the degradation of the polymer electrolyte in H<sub>2</sub>-O<sub>2</sub> fuel cell. *Chemical physics letters*, 371(1):80–85, 2003.
- [65] R. Hutchinson, N. Fleck, and A. Cocks. A sintering model for thermal barrier coatings. *Acta materialia*, 54(5):1297–1306, 2006.
- [66] B. Jakobsen. *In-situ studies of bulk deformation structures: Static properties under load and Dynamics during deformation*. PhD thesis, 2007.
- [67] M. Kamaya, A. J. Wilkinson, and J. M. Titchmarsh. Measurement of plastic strain of polycrystalline material by electron backscatter diffraction. *Nuclear engineering and design*, 235(6):713–725, 2005.
- [68] B. Kanka. Einstellung des faservolumengehaltes in oxidkeramischen faserverbundwerkstoffen, Mar. 6 2013. EP Patent 1,734,023.
- [69] B. Kanka, J. Göring, M. Schmücker, and H. Schneider. Processing, microstructure and properties of Nextel 610, 650 and 720 fiber/porous mullite matrix composites. *Ceram. Engin. Sci. Proc.*, 22:703, 1980.

- [70] A. M. Karlsson and A. G. Evans. A numerical model for the cyclic instability of thermally grown oxides in thermal barrier systems. *Acta Materialia*, Volume 49 Issue 10:1793–1804, 2001.
- [71] H. Kaya. The application of ceramic-matrix composites to the automotive ceramic gas turbine. *Composites science and technology*, 59(6):861–872, 1999.
- [72] M. Ke, S. Hackney, W. Milligan, and E. Aifantis. Observation and measurement of grain rotation and plastic strain in nanostructured metal thin films. *Nanostructured Materials*, 5(6):689–697, 1995.
- [73] A. Khounsary, P. Kenesei, J. Collins, G. Navrotsky, and J. Nudell. High energy x-ray micro-tomography for the characterization of thermally fatigued glidcop specimen. In *Journal of Physics: Conference Series*, volume 425, page 212015. IOP Publishing, 2013.
- [74] R. Kitazawa, H. Kakisawa, and Y. Kagawa. Anisotropic tgo morphology and stress distribution in EB-PVD  $Y_2O_3$ - $ZrO_2$  thermal barrier coating after in-phase thermo-mechanical test. *Surface and Coatings Technology*, 238:68–74, 2014.
- [75] K. Knipe. *In-Situ Synchrotron Studies of Turbine Blade Thermal Barrier Coatings under Extreme Environments*. PhD thesis, University of Central Florida Orlando, Florida, 2014.
- [76] K. Knipe, A. Manero, S. F. Siddiqui, S. Sofronsky, P. Fouquet, S. Raghavan, C. Meid, J. Wischek, M. Bartsch, J. Okasinski, et al. Synchrotron xrd measure-

ments of thermal barrier coatings subjected to loads representing operational conditions of rotating gas turbine blades.

- [77] K. Knipe, A. C. Manero, S. Sofronsky, J. Okasinski, J. Almer, J. Wischek, C. Meid, A. Karlsson, M. Bartsch, and S. Raghavan. Synchrotron x-ray diffraction measurements mapping internal strains of thermal barrier coatings during thermal gradient mechanical fatigue loading. *Journal of Engineering for Gas Turbines and Power*, 137(8):082506, 2015.
- [78] K. Knipe, A. Manero II, S. F. Siddiqui, C. Meid, J. Wischek, J. Okasinski, J. Almer, A. M. Karlsson, M. Bartsch, and S. Raghavan. Strain response of thermal barrier coatings captured under extreme engine environments through synchrotron x-ray diffraction. *Nature Communications*, 5, 2014.
- [79] R. Knoche, E. Werth, M. Weth, J. G. Garcia, C. Wilhelmi, and M. Gerendas. Design and development approach for gas turbine combustion chambers made of oxide ceramic matrix composites. In *Ceramic Engineering and Science Proceedings*, volume 32, pages 77–87. American Ceramic Society, Inc., 735 Ceramic Place Westerville OH 43081 United States, 2011.
- [80] D. Koch, K. Tushtev, and G. Grathwohl. Ceramic fiber composites: Experimental analysis and modeling of mechanical properties. *Composites Science and Technology*, 68(5):1165–1172, 2008.

- [81] D. Koch, K. Tushtev, J. Horvath, R. Knoche, and G. Grathwohl. Evaluation of mechanical properties and comprehensive modeling of CMC with stiff and weak matrices. In *Advances in Science and Technology*, volume 45, pages 1435–1443. Trans Tech Publ, 2006.
- [82] W. Krenkel, B. Heidenreich, and R. Renz. C/c-sic composites for advanced friction systems. *Advanced Engineering Materials*, 4(7):427–436, 2002.
- [83] S. Kyriakides, R. Arseculeratne, E. Perry, and K. Liechti. On the compressive failure of fiber reinforced composites. *International Journal of Solids and Structures*, 32(6):689–738, 1995.
- [84] C. G. Levi, J. Y. Yang, B. J. Dalgleish, F. W. Zok, and A. G. Evans. Processing and performance of an all-oxide ceramic composite. *Journal of the American Ceramic Society*, 81(8):2077–2086, 1998.
- [85] A. M. Limarga, R. Vaßen, and D. R. Clarke. Stress distributions in plasma-sprayed thermal barrier coatings under thermal cycling in a temperature gradient. *Journal of Applied Mechanics*, 78:011003, 2011.
- [86] F. Liu and W. A. Sirignano. Turbojet and turbofan engine performance increases through turbine burners. *Journal of Propulsion and Power*, 17(3):695–705, 2001.
- [87] S.-Y. Liu and I.-W. Chen. Fatigue of yttria-stabilized zirconia: I, fatigue damage, fracture origins, and lifetime prediction. *Journal of the American Ceramic Society*, 74(6):1197–1205, 1991.

- [88] V. Lughi, V. K. Tolpygo, and D. R. Clarke. Microstructural aspects of the sintering of thermal barrier coatings. *Materials Science and Engineering: A*, 368(1):212–221, 2004.
- [89] A. C. Manero, S. Sofronsky, K. Artzt, S. Hackemann, J. Wischek, J. Okasinski, P. Kenesei, J. Almer, M. Bartsch, and S. Raghavan. Interpreting high temperature deformation behavior of a ceramic matrix composite via high energy x-rays and numerical simulation. In *57th AIAA/ASCE/AHS/ASC Structures, Structural Dynamics, and Materials Conference*, page 0410, 2016.
- [90] A. Manero II, S. Sofronsky, K. Knipe, C. Meid, J. Wischek, J. Okasinski, J. Almer, A. M. Karlsson, S. Raghavan, and M. Bartsch. Monitoring local strain in a thermal barrier coating system under thermal mechanical gas turbine operating conditions. *JOM*, 67(7):1528–1539, 2015.
- [91] A. C. Manero II. *Nondestructive Analysis of Advanced Aerospace Materials Via Spectroscopy and Synchrotron Radiation*. PhD thesis, University of Central Florida Orlando, Florida, 2014.
- [92] T. Manns and B. Scholtes. DECcalc-A program for the calculation of diffraction elastic constants from single crystal coefficients. In *Materials Science Forum*, volume 681, pages 417–419. Trans Tech Publication, 2011.
- [93] L. Margulies, G. Winther, and H. Poulsen. In situ measurement of grain rotation during deformation of polycrystals. *Science*, 291(5512):2392–2394, 2001.



- [94] A. F. Massardo, C. F. McDonald, and T. Korakianitis. Microturbine/fuel-cell coupling for high-efficiency electrical-power generation. *Journal of Engineering for Gas Turbines and Power*, 124(1):110–116, 2002.
- [95] V. Maurel, A. Koster, and L. Rémy. An analysis of thermal gradient impact in thermal–mechanical fatigue testing. *Fatigue & Fracture of Engineering Materials & Structures*, 33(8):473–489, 2010.
- [96] D. May, A. Gordon, and D. Segletes. The application of the norton-bailey law for creep prediction through power law regression. In *ASME Turbo Expo 2013: Turbine Technical Conference and Exposition*, pages V07AT26A005–V07AT26A005. American Society of Mechanical Engineers, 2013.
- [97] P. Mechnich and W. Braue. Air plasma-sprayed  $Y_2O_3$  coatings for  $Al_2O_3/Al_2O_3$  ceramic matrix composites. *Journal of the European Ceramic Society*, 33(13):2645–2653, 2013.
- [98] R. R. Naslain. Sic-matrix composites: Nonbrittle ceramics for thermo-structural application. *International Journal of Applied Ceramic Technology*, 2(2):75–84, 2005.
- [99] F. Norton. Creep of high temperatures, 1929.
- [100] H. Ohnabe, S. Masaki, M. Onozuka, K. Miyahara, and T. Sasa. Potential application of ceramic matrix composites to aero-engine components. *Composites Part A: Applied Science and Manufacturing*, 30(4):489–496, 1999.

- [101] J. Petek and P. Hamilton. Performance monitoring for gas turbines performance monitoring for gas turbines. *Orbit*, 75:64–74, 2005.
- [102] R. Raj and M. Ashby. On grain boundary sliding and diffusional creep. *Metallurgical transactions*, 2(4):1113–1127, 1971.
- [103] A. K. Ray, S. Bose, P. K. De, and D. K. Das. Lifetime evaluation of a thick thermal barrier coated superalloy used in turbine blade. *Materials Science and Engineering*, A 527:5474–5483, 2010.
- [104] L. Rémy, C. Guerre, I. Rouzou, and R. Molins. Assessment of tbc oxidation-induced degradation using compression tests. *Oxidation of metals*, 81(1-2):3–15, 2014.
- [105] D. H. Richter. *Multiscale homogenization of ceramic composites with porous matrix phase*. PhD thesis, 2012.
- [106] H. Richter and L. Hoehe. Numerical modelling of a ceramic matrix composite with porous matrix phase. In *Proceedings of the 13th ONERA-DLR Aerospace Symposium*, pages 1–10, 2013.
- [107] O. A. Ruano and O. D. Sherby. Low stress creep of fine-grained materials at intermediate temperatures: Diffusional creep or grain boundary sliding? *Materials Science and Engineering*, 56(2):167–175, 1982.

- [108] M. Ruggles-Wrenn and R. Lanser. Tension-compression fatigue of an oxide/oxide ceramic composite at elevated temperature. *Materials Science and Engineering: A*, 659:270–277, 2016.
- [109] M. Schmücker, A. Grafmüller, and H. Schneider. Mesostructure of WHIPOX all oxide CMCs. *Composites Part A: Applied Science and Manufacturing*, 34(7):613–622, 2003.
- [110] M. Schmücker and P. Mechnich. Improving the microstructural stability of Nextel 610 alumina fibers embedded in a porous alumina matrix. *Journal of the American Ceramic Society*, 93(7):1888–1890, 2010.
- [111] M. Schmücker and H. Schneider. WHIPOX all oxide ceramic matrix composites. In *Handbook of Ceramic Composites*, pages 423–435. Springer, 2005.
- [112] U. Schulz. Phase transformation in EB-PVD yttria partially stabilized zirconia thermal barrier coatings during annealing. *Journal of the American Ceramic Society*, 83(4):904–910, 2000.
- [113] U. Schulz, C. Leyens, K. Fritscher, M. Peters, B. Saruhan-Brings, O. Lavigne, J.-M. Dorvaux, M. Poulain, R. Mévrel, and M. Caliez. Some recent trends in research and technology of advanced thermal barrier coatings. *Aerospace Science and technology*, 7(1):73–80, 2003.

- [114] U. Schulz, H. Oettel, and W. Bunk. Texture of EB-PVD thermal barrier coatings under variable deposition conditions. *Zeitschrift für Metallkunde*, 87(6):488–492, 1996.
- [115] Y. Shi, S. Hofmann, S. Hackemann, and D. Koch. Evaluation and validation of elastic properties and a failure criterion for an oxide wound ceramic composite material. *High Temperature Ceramic Matrix Composites 8: Ceramic Transactions, Volume 248*, pages 433–442, 2013.
- [116] S. F. Siddiqui, K. Knipe, A. Manero, C. Meid, J. Wischek, J. Okasinski, J. Almer, A. M. Karlsson, M. Bartsch, and S. Raghavan. Synchrotron x-ray measurement techniques for thermal barrier coated cylindrical samples under thermal gradients. *Review of Scientific Instruments*, 84(8):083904, 2013.
- [117] J. Singer. Creep rupture of ductile materials under variable load. *Journal of Mechanical Engineering Science*, 7(2):193–197, 1965.
- [118] S. Sjöström and H. Brodin. Influence of TBC end geometry on the TMF life of an APS TBC. *Procedia Engineering*, 2(1):1363–1371, 2010.
- [119] Y. Sohn, J. Kim, E. Jordan, and M. Gell. Thermal cycling of EB-PVD/MCrAlY thermal barrier coatings: I. microstructural development and spallation mechanisms. *Surface and Coatings Technology*, 146:70–78, 2001.
- [120] C. Templier, J. Stinville, P. Villechaise, P. Renault, G. Abrasonis, J. Rivière, A. Martinavičius, and M. Drouet. On lattice plane rotation and crystallographic

- structure of the expanded austenite in plasma nitrided AISI 316L steel. *Surface and Coatings Technology*, 204(16):2551–2558, 2010.
- [121] U. Trabandt and K. Handrik. CMC nose skirt panels for X-38-successfully qualification tested and fit-checked. In *IAF abstracts, 34th COSPAR Scientific Assembly*, volume 1, page 499, 2002.
- [122] D. Traudes and A. Harrison. Overview of fatigue and creep testing of ceramic matrix composites for aerospace: ceramic matrix composites have come a long way in the past decade in their ability to have sustained strength at high temperatures. *Quality*, 54(11):S17–S17, 2015.
- [123] K. Tushtev, J. Horvath, D. Koch, and G. Grathwohl. Deformation and failure modeling of fiber reinforced ceramics with porous matrix. *Advanced Engineering Materials*, 6(8):664–669, 2004.
- [124] E. TZIMAS, H. MULLEJANS, S. PETEVES, J. BRESSERS, and W. STAMM. Failure of thermal barrier coating systems under cyclic thermomechanical loading. *Acta Materialia*, 48:4699–4707, 2000.
- [125] M. van Roode, J. Price, J. Kimmel, N. Miriyala, D. Leroux, A. Fahme, and K. Smith. Ceramic matrix composite combustor liners: a summary of field evaluations. *Journal of Engineering for Gas Turbines and Power*, 129(1):21–30, 2007.

- [126] B. Veal, A. Paulikas, B. Gleeson, and P. Hou. Creep in  $\alpha$ -Al<sub>2</sub>O<sub>3</sub> thermally grown on  $\beta$ -NiAl and NiAlPt alloys. *Surface and Coatings Technology*, 202(4):608–612, 2007.
- [127] B. W. Veal, A. P. Paulikas, and P. Y. Hou. Tensile stress and creep in thermally grown oxide. *Nature Materials*, 5:349–351, May 2006.
- [128] X.-L. Wang, J. Almer, C. Liu, Y. Wang, J. Zhao, A. Stoica, D. Haeffner, and W. Wang. In situ synchrotron study of phase transformation behaviors in bulk metallic glass by simultaneous diffraction and small angle scattering. *Physical review letters*, 91(26):265501, 2003.
- [129] P. Weiss, L. Obadia, D. Magne, X. e. Bourges, C. Rau, T. Weitkamp, I. Khairoun, J. Bouler, D. Chappard, O. Gauthier, et al. Synchrotron x-ray microtomography (on a micron scale) provides three-dimensional imaging representation of bone in-growth in calcium phosphate biomaterials. *Biomaterials*, 24(25):4591–4601, 2003.
- [130] S. Whitaker. Forced convection heat transfer correlations for flow in pipes, past flat plates, single cylinders, single spheres, and for flow in packed beds and tube bundles. *AIChE Journal*, 18(2):361–371, 1972.
- [131] J. D. Whitcomb. *Composite materials: testing and design (eighth conference)*, volume 972. ASTM International, 1988.
- [132] D. M. Wilson. Statistical tensile strength of Nextel<sup>TM</sup> 610 and Nextel<sup>TM</sup> 720 fibres. *Journal of Materials Science*, 32(10):2535–2542, 1997.

- [133] H. Winick, G. Brown, K. Halbach, and J. Harris. Wiggler and undulator magnets. *Physics Today*, 34(5):50–63, 1981.
- [134] M. M. Woolfson. *An introduction to X-ray crystallography*. Cambridge University Press, 1997.
- [135] P. K. Wright. Influence of cyclic strain on life of a pvd tbc. *Materials Science and Engineering: A*, 245(2):191–200, 1998.
- [136] X. Wu, S. R. Kalidindi, C. Necker, and A. A. Salem. Prediction of crystallographic texture evolution and anisotropic stress–strain curves during large plastic strains in high purity  $\alpha$ -titanium using a taylor-type crystal plasticity model. *Acta Materialia*, 55(2):423–432, 2007.
- [137] Q. Yang, K. Rugg, B. Cox, and D. Marshall. Evaluation of macroscopic and local strains in a three-dimensional woven C/SiC composite. *Journal of the American Ceramic Society*, 88(3):719–725, 2005.
- [138] H. Zhao, F. Yu, T. D. Bennett, and H. N. Wadley. Morphology and thermal conductivity of yttria-stabilized zirconia coatings. *Acta Materialia*, 54(19):5195–5207, 2006.
- [139] F. W. Zok and C. G. Levi. Mechanical properties of porous-matrix ceramic composites. *Advanced Engineering Materials*, 3(1-2):15–23, 2001.

- [140] N. Zotov, M. Bartsch, L. Chernova, D. Schmidt, M. Havenith, and G. Eggeler. Effects of annealing on the microstructure and the mechanical properties of EB-PVD thermal barrier coatings. *Surface and Coatings Technology*, 205(2):452–464, 2010.